COMPUTATIONAL STUDY FOR TISSUE-SPECIFIC DOSIMETRIC QUANTITIES OF

SECONDARY RADIATION FOR MARS EXPLORATION

By

Sungmin Pak

Bachelor of Science – Astronomy and Space Science
Kyung Hee University
2016

Master of Science – Space Research
Kyung Hee University
2018

A dissertation submitted in partial fulfillment
of the requirements for the

Doctor of Philosophy – Interdisciplinary Health Sciences

The Graduate College

University of Nevada, Las Vegas
May 2024

Dissertation Approval

This dissertation prepared by

Sungmin Pak

entitled

Computational Study for Tissue-Specific Dosimetric Quantities of Secondary Radiation for Mars Exploration

is approved in partial fulfillment of the requirements for the degree of

Doctor of Philosophy – Interdisciplinary Health Sciences
The Graduate College

Francis Cucinotta, Ph.D.
Examination Committee Chair

Steen Madsen, Ph.D.
Examination Committee Member

Daniel Young, Ph.D.
Examination Committee Member

Alexander Barzilov, Ph.D.
Graduate College Faculty Representative

Alyssa Crittenden, Ph.D.
*Vice Provost for Graduate Education &
Dean of the Graduate College*

Abstract

The two main sources of primary space radiation, Galactic Cosmic Rays (GCRs) and Solar Particle Events (SPEs), encompass a spectrum of ions, ranging from protons (Z=1) to nickel ions (Z=28), with energies spanning from less than 1 keV to exceeding a few TeV. While SPEs represent sporadic events primarily comprised of a high flux of low- to intermediate-energy protons, GCRs are characterized by continuous low flux of diverse ions with higher energies, peaking in intensity near the solar minimum. During a Mars mission, astronauts will encounter primary particles of high energy from GCR and SPE spectra, capable of penetrating spacecraft and habitat structures, along with secondary particles generated through interactions between primary space radiation and shielding materials and human tissues. While considerable attention has been devoted to primary particles in space missions in prior research, the biomedical consequences of exposure to secondary particles, especially mesons, have received comparatively less scrutiny despite their growing significance in deep space with augmented shielding. This dissertation project fills this gap by investigating the dosimetric quantities of secondary neutrons, pions, and kaons within various human organs for Mars exploration for the first time. Using a realistic computational human male phantom collaboratively developed by the International Commission on Radiological Protection (ICRP) and the International Commission on Radiation Units and Measurements (ICRU), the absorbed dose and dose equivalent in human organs of each baryon, meson, and lepton, as well as their effective dose, have been meticulously evaluated. For the worst-case scenario, exposure to GCR near the solar minimum and two of the most significant SPEs in the space age, events in August 1972 and September 1989, has been considered for the interplanetary cruise phase and the surface phase on Mars with varying thicknesses of aluminum shielding. The simulations have been executed using the PHITS3.27 Monte Carlo simulation toolkit on the Cherry-Creek

Cluster at the University of Nevada, Las Vegas (UNLV) National Supercomputing Institute (NSI). Dosimetric quantities have been evaluated based on the ICRP publications and the NASA Space Cancer Risk (NSCR) model.

The results indicate that the total effective dose assessed with the NSCR model for GCR exposure in interplanetary space decreases from 43.4 cSv/yr to 39.0 cSv/yr as the aluminum shielding amount increases from 1 g/cm^2 to 50 g/cm^2. Conversely, the sum of neutron, pion, and kaon effective doses increases from 2.8 cSv/yr to 9.3 cSv/yr. This implies that the contribution of these secondary particles to the total effective dose escalates from 6.5% for 1 g/cm^2 aluminum shielding to 23.9% for 50 g/cm^2 aluminum shielding. An increase in secondary contribution is also suggested with the ICRP model and SPE exposure. The contribution of secondary particles on the Martian surface is found to be less contingent on aluminum shielding depth, while it surpasses 20% even with thin 1 g/cm^2 aluminum shielding. This is attributable to the heightened generation of secondary neutrons in the Martian atmosphere and ground. The comprehensive analysis conducted in this project, pertaining to tissue-specific dosimetric quantities within an advanced human phantom under practical radiation exposure scenarios, furnishes valuable insights into the potential health risks associated with secondary particles during Mars exploration.

Acknowledgements

I am deeply thankful to Professor Francis Cucinotta, my doctoral advisor, for his unwavering guidance and mentorship throughout the journey of completing this dissertation. His profound expertise and insights have not only shaped my research but have also nurtured my academic growth. His pioneering work in the field has been a driving force behind my pursuit of a doctoral degree, and it has been a tremendous honor to be his student.

I extend sincere gratitude to Professor Steen Madsen for his exceptional teaching and support during my doctoral studies. The foundational knowledge of radiation biology that I gained from him has been instrumental in shaping this dissertation project and will continue to be invaluable in my research career. His assistance and encouragement throughout my doctoral program have been invaluable.

My gratitude also goes to my dissertation committee members, Professor Daniel Young and Professor Alexander Barzilov, for their constructive advice and critical insights that greatly enriched the quality of this work.

I am profoundly indebted to my family for their unwavering love and encouragement throughout this endeavor. Their belief in me has been a constant source of motivation. I am especially thankful to my wife, whose dedication and support—from helpful discussions to caring for our newborn child—have been indispensable. Her numerous contributions allowed me to focus on my research and dissertation project.

Special thanks are extended to Professor Janice Pluth and Dr. Krishnakumar Nangeelil for their continuous support and insightful discussions during both the highs and lows of this doctoral journey. Their encouragement has served as a guiding light, propelling me forward.

Table of Contents

List of Tables

List of Figures

Chapter 1: Introduction

Following the historic first human moon landing in 1969, humanity is once again turning its gaze towards deep space. Discussions, plans, and active missions for human exploration of the Earth's moon and Mars are taking place globally among space agencies. The National Aeronautics and Space Administration (NASA) is leading the Artemis program, aiming to return humans to the Moon and eventually embark on a mission to Mars (NASA, 2020). The Artemis program encompasses objectives such as human landings on the lunar south pole region, the establishment of Artemis Base Camp on the lunar surface, and the placement of the Gateway in lunar orbit. Artemis Base Camp is envisioned as a home for astronauts who will be annually sent to the Moon, and the Gateway is envisioned to be a vital station for crews heading to the Moon, Mars, and other destinations. The Artemis program is a colossal international project collaborated by 36 countries, including Angola, Argentina, Australia, Bahrain, Belgium, Brazil, Bulgaria, Canada, Columbia, Czech Republic, Ecuador, France, Germany, Greece, Iceland, India, Israel, Italy, Japan, Luxemburg, Mexico, Netherlands, New Zealand, Nigeria, Poland, Republic of Korea, Romania, Rwanda, Saudi Arabia, Singapore, Spain, Ukraine, United Arab Emirates, United Kingdom, United States of America, and Uruguay. On the other hand, the China National Space Administration (CNSA) has proposed its own project for human lunar landings in the 2030s, planning to establish the International Lunar Research Station (ILRS) by 2036 in collaboration with Azerbaijan, Belarus, Egypt, Pakistan, Russia, South Africa, and Venezuela. CNSA also proposed its first crewed mission to Mars in the 2030s.

Space travel captures the interest of not only government agencies but also private enterprises like Virgin Galactic and Blue Origin, venturing into space tourism. While their current programs are limited to suborbital flights at approximately 100 km altitude, efforts are underway to extend space

tourism into deep space. Blue Origin has been selected by NASA to develop a crewed moon lander (O'Shea, 2023), and Space Exploration Technologies Corp. (SpaceX) is focusing its efforts on creating spaceships for human transportation to and landing on the Moon and Mars (Musk, 2018). Astronauts in outer space face an environment vastly different from Earth's. Microgravity induces physiological changes in the human body (Bizzarri, Monici, & van Loon, 2015), including compromised immune system (Bradbury et al., 2020), brain vestibular deprivation and cephalic fluid shift (De la Torre, 2014; Roberts et al., 2015; Hargens & Vico, 2016; Roberts et al., 2017), and bone and muscle loss (Maupin et al., 2019; Lee et al., 2020; Stavnichuk et al., 2020). Space radiation is a significant health concern (Cucinotta & Durante, 2006a; Durante & Cucinotta, 2011), especially for deep space explorations such as Moon and Mars missions, where astronauts are exposed to a harsh radiation environment lacking Earth's natural protection (Cucinotta et al., 2010). The aforementioned projects to the Moon and Mars are missions beyond the low Earth orbit (LEO). LEO is loosely defined as orbits between 160 km and 1000 km above Earth, and the International Space Station (ISS) is located with an average altitude near 400 km (ESA, 2020). Within LEO, astronauts can be protected from severe space radiation because charged particles with energy below about 1000 MeV/u are deflected, scattered, and lose their energy by Earth's magnetosphere and atmosphere (Cucinotta et al., 2010). However, crews for missions beyond LEO encounter elevated levels of radiation exposure from Solar Particle Events (SPEs) and Galactic Cosmic Rays (GCRs) without the natural shielding of Earth (Cucinotta et al., 2001). SPEs are particles accelerated into space during solar flares or Coronal Mass Ejections (CMEs), which are sporadic and largely unpredictable events (Baker, 1998; Baker, 2002). Their components are well known to be mostly protons, followed by alpha particles, and a smaller number of other positive ions and electrons (Cucinotta et al., 1994b; Townsend et al., 1994; Phillips, 1995). Their intensity and

energy spectra vary from event to event, and most SPEs are known to not induce serious health concerns in astronauts (Kim, George, & Cucinotta, 2006; Kim, Cucinotta, & Wilson, 2007; Kim et al., 2009a; Kim et al., 2009b; Wu et al., 2009). According to satellite data, more than 70 SPEs are usually measured in one solar cycle (approximately 11 years), and more than 20% of the events have a significant fluence ($\geq 2 \times 10^9$ cm^{-2}) above 30 MeV (Shea & Smart, 1990; Kim et al., 2009a). While the majority of SPEs lead to negligible radiation dose due to their low flux and energy, it can be much more significant during noticeably strong solar storms such as the events in August 1972 and September 1989 (Kim et al., 2009a; Jiggens et al., 2014).

On the other hand, GCRs originate from beyond the solar system, consisting of particles similar to SPEs but with an increased proportion of alpha particles and heavy ions with higher energy, while protons remain predominant (Badhwar & O'Neill, 1994; NCRP, 2006). GCRs are standing radiation, and the energy spectra of their components are well-defined depending on the solar activity (Wilson et al., 1995a). Because of their high energy, GCR ions can penetrate spacecraft structures and contribute a large portion of radiation dose to crew members (Cucinotta, Kim, & Ren, 2006b). In addition, the high energy of GCRs with mean energy above 1 GeV/u leads to substantial secondary radiation production from nuclear interactions. Recent measurements from the Mars Science Laboratory Radiation Assessment Detector (MSL/RAD) during the transit to Mars and on the surface of Mars (Ehresmann et al., 2016; Matthiä et al., 2016) confirm that astronauts will receive a high dose of radiation from various high energy primary and secondary particle species, ranging from protons ($Z = 1$) to ions heavier than iron ($Z > 26$), during the missions beyond LEO.

Efforts to safeguard astronauts from SPEs and GCRs during space missions involve the use of passive shielding, a practice employed in past and upcoming space explorations (Cucinotta, Kim,

& Ren, 2006b; Durante & Cucinotta, 2011). However, it has been found that numerous secondary particles are produced by the interactions between primary space radiation and radiation shielding materials of spacecraft (Heilbronn et al., 2005; Heilbronn et al., 2014; Heilbronn et al., 2015; Rojdev et al., 2015). Monte Carlo simulations by Heilbronn et al. (2014) demonstrate that the number of secondary neutrons generated by one incident GCR ion in interplanetary space increases from 0.23 with 1 cm of aluminum (2.7 g/cm^2 Al) shielding to 10.5 with 20 cm of aluminum (54 g/cm^2 Al) shielding. For GCR exposure, around 65 to 70% of the secondary neutrons are produced by protons, 15 to 30% by alpha particles, and 5 to 15% by heavy ions, depending on the shielding material and thickness (Wilson, 1997; Heilbronn et al., 2014). On the other hand, Monte Carlo simulations by Jun (2001) suggest that a high secondary neutron dose is induced by trapped protons. In addition to neutrons, substantial dose and fluence of other secondary particles such as pions and kaons are also expected for GCR, while the tissue-specific contributions of mesons to the dose equivalent has received little attention in the past.

Radiation exposure, including neutrons and mesons, pose the risks of late effects, encompassing cancer, genetic effects, and neurological disorders (Morgan, 1972; Ainsworth et al., 1973; Ornitz et al., 1980; Withers, Thames Jr, & Peters, 1982; Gasinska et al., 1993; NRC, 1997; Hall & Giaccia, 2018; Stricklin et al., 2021). As crewed long-duration space missions to the Moon and Mars progress, assessing health risks arising from both primary and secondary particles in various space radiation exposure scenarios becomes imperative. Radiation exposure to tissue during both SPE and GCR exposures should be carefully reviewed, as an intense SPE can deliver a large amount of acute dose, especially when not enough protection is given in extravehicular activity (EVA) in interplanetary space or on the surface of planets, moons, and asteroids (Kim, Cucinotta, & Wilson,

2007; Kim et al., 2009b), and GCR takes a major contribution to the dosimetric quantities during the whole mission time (Cucinotta et al., 2001; Cucinotta et al., 2013b; Hassler et al., 2014).

The focus of the current study is to evaluate the tissue-specific absorbed dose and fluence of secondary neutrons and charged mesons behind the various thicknesses of passive aluminum shielding during SPE and GCR exposures in interplanetary space and on the Martian surface using the Monte Carlo simulation code, PHITS. The tissue-specific dose equivalent and effective dose of secondary neutrons, pions, and kaons for Mars exploration are then assessed based on the publications of the International Commission on Radiological Protection (ICRP) (ICRP, 1977; ICRP 1991; ICRP 2007) and the latest NASA Space Cancer Risk model (NSCR-2022) (Cucinotta, Kim, & Chappell, 2012; Cucinotta, Kim, & Chappell, 2013a; Cucinotta, To, & Cacao, 2017; Cucinotta et al., 2020a; Cucinotta & Saganti, 2022a; Cucinotta, 2022b). The NSCR model has been developed for space exposures and reviewed by the NCRP (2014) and the US National Academy of Sciences (NRC, 2012), while the ICRP quality factor (QF) is developed for ground-based exposures.

Chapter 2: Background

2.1: Radiation Exposure in Space

2.1.1: Physical Characteristics of Ions

The two primary sources of space radiation, SPEs and GCRs, consist of ions, predominantly protons, alpha particles, and smaller amounts of other light ions and heavy ions. Heavy ions, although less numerous, are high LET radiation with a much higher biological effectiveness compared to photons or protons leading to an important concern in radiation protection. When atoms move at high speeds, their atomic electrons are stripped away, leading to the formation of positively charged ions. Ions have higher mass compared to electrons and other charged particles, and even the lightest ion, i.e., a proton, possesses a rest mass 1837 times greater than that of an electron.

Charged particles interact with nuclei or orbital electrons in the materials mainly through Coulomb force due to their electric charge. These interactions encompass inelastic collisions with orbital electrons, elastic scattering by nuclei known as the Rutherford scattering, emission of Bremsstrahlung radiation, emission of Cherenkov radiation, and nuclear reactions (Attix, 2008; Knoll, 2010; Korcyl, 2012; Hall & Giaccia, 2018). Because of the increased mass of ions, inelastic collisions with electrons are considered the primary mechanism of ion interaction with matter, while others are typically negligible, except for nuclear reactions.

Nuclear reactions involve the production of one or more particles through collisions between nuclei or between a nucleus and a nucleon. It is commonly denoted as a + X → Y + b or simply X(a, b)Y, where X is the target, a is the projectile, and Y and b are the reaction products. During the process, total energy, linear momentum, charge, Baryon number, angular momentum, and

parity are conserved (Krane, 1987). Through nuclear reactions, a significant number of secondary particles, also known as fragments, are produced (Figure 2.1) (Zeitlin et al., 1996; Haettner, Iwase, & Schardt, 2006; Cucinotta et al., 2011a; Bolst et al., 2017). Because the multiplicity of particles produced can be quite high (>5), cross-section measurements are often of the inclusive type, where only a single type of secondary is measured. The variety of fragments creates a mixed radiation field in matter, complicating dose calculations, treatment planning, and shielding efforts (Cucinotta et al., 2011a; Desouky & Zhou, 2016; Pak & Cucinotta, 2021). Table 2.1 lists several important nuclear reactions relevant to heavy ion therapy and space radiation research (Cucinotta et al., 2011a). The diverse range of nuclear reaction types poses a significant challenge for radiation transport codes to accurately describe ion transport in materials or tissues.

Through inelastic Coulomb collision with heavy ions, orbital electrons can be raised to a higher energy level, so-called excitation, or can be completely removed from the atom, which is called ionization. Electrons knocked out from their parent atoms may possess sufficient energy to ionize other atoms, and these fast secondary electrons are termed delta-rays (Knoll, 2010). As a consequence of energy transfer to one or more electrons in matter, heavy ions continuously lose energy and decelerate. The loss in energy (dE) of the incident ion per path length (dx) in matter is defined as the stopping power (S):

$$S = -\frac{dE}{dx}. \tag{2.1}$$
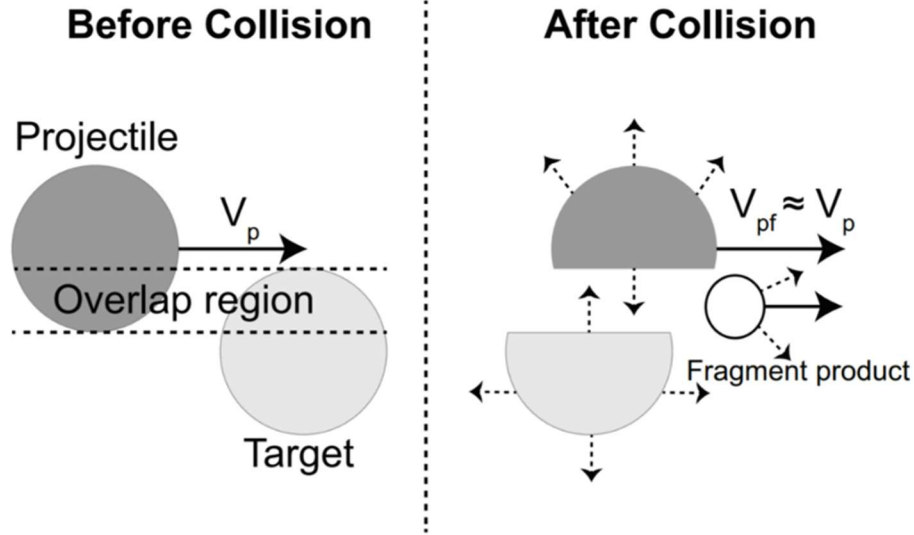
Figure 2.1. Illustration of fragmentation procedure of heavy ion interaction. Fragments have a similar velocity to the initial projectile but smaller mass and charge. Image reprinted from Bolst et al. (2017).

Table 2.1. Important nuclear reactions for heavy ion therapy and space radiation research. Table reprinted from Cucinotta et al. (2011a).

Reaction	Secondary	Mechanism	Comment
Nucleon-Nucleus Nucleus-Nucleus	Nucleon	Knockout, cascade	Low linear energy transfer, large range
Nucleon-Nucleus Nucleus-Nucleus	Nucleon	Evaporation	Medium or high linear energy transfer, small range
Nucleon-Nucleus Nucleus-Nucleus	Light ion	Direct knockout, nuclear evaporation or de-excitation, coalescence	Low to medium linear energy transfer, small to large range
Nucleon-Nucleus	Heavy ion	Elastic collision or target fragment	High linear energy transfer, small range
Nucleus-Nucleus	Heavy ion	Projectile fragment	Large range
Nucleus-Nucleus	Heavy ion	Target fragment	High linear energy transfer, small range
Nucleon-Nucleus Nucleus-Nucleus	Meson, γ-ray, electron, etc.	Inelastic collision	Low linear energy transfer, large range

To account for the density of the matter (ρ), the mass stopping power (S_ρ) is also commonly utilized, defined as:

$$S_\rho = -\frac{dE}{\rho dx}. \tag{2.2}$$

The mass stopping power (S_ρ) is a sum of the mass radiative stopping power ((S_ρ)$_r$) and the mass collision stopping power ((S_ρ)$_c$), while the radiative stopping power is insignificant for heavy ions. The Bethe formula expresses the mass collision stopping power (Attix, 2008):

$$\left(S_\rho\right)_c = \frac{4\pi e^4 z^2}{m_0 c^2 \beta^2} \frac{N_A Z}{A}\left[\ln\left(\frac{2m_0 c^2 \beta^2}{(1-\beta^2)I}\right) - \beta^2\right]. \tag{2.3}$$

In this equation, e is the electronic charge, m_0 is the electron rest mass, c is the speed of light, β is the relative speed of the incident particle to c, z is the atomic number of the incident ion, N_A is the Avogadro's number, Z is the nuclear charge number of the matter, A is the mass number of the matter, and I is the mean excitation potential of the matter. This expression reveals that the loss in energy of the incident particle depends on the electron density of the matter, as well as the incident particle type and speed. Stopping power is inversely proportional to the speed squared, indicating that heavy ions lose and deliver most of their energy near the end of their track, designated as the Bragg peak (Figure 2.2) (Smith, 2006).
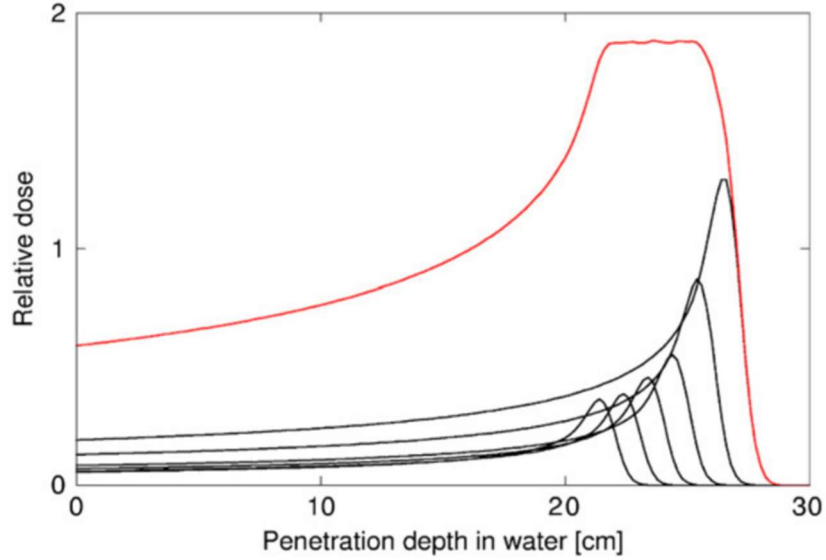
Figure 2.2. Bragg peaks (black) and Spread-Out Bragg Peaks (SOBP) (red) of energy-modulated protons. The location of the Bragg peak is contingent on the incident energy of the charged particle. Clinically, to treat a large area, SOBP, composed of multiple Bragg peaks from protons with different energies, can be used. Image reprinted from Smith (2006).

The depth that a charged particle travels before coming to a stop is referred to as range (R), which

can be calculated as:

$$R(E) = \int_0^E \left(-\frac{dE}{dx} \right)^{-1} dE. \tag{2.4}$$

The approximated average range is defined as the continuous-slowing-down approximation

(CSDA) range. The CSDA ranges for protons in various materials are available on the PSTAR

(Stopping-Power And Range Tables for Proton) website, managed by the National Institute of

Standards and Technology (NIST, 2023). The range of proton can be converted to the range of

other charged particles with the same speed using the formula:

$$R = \frac{m}{m_p z^2} R_p. \tag{2.5}$$

Here, R is the range of the charged particle with the same speed as the proton with range R_p, m is the mass of the charged particle, m_p is the mass of a proton, and z is the atomic number of the charged particle (Knoll, 2010).

When discussing the energy absorbed by the matter, the restricted stopping power, more commonly referred to as linear energy transfer (LET, L), is used (Belkic, 2012; Hall & Giaccia, 2018):

$$L = \frac{dE}{dl}. \tag{2.6}$$

Here, dE is the mean local energy transferred to the matter, and dl is the projectile's traveling distance. LET varies with the incident particle energy and type. Heavy ions, due to delivering more energy over a short distance in the matter compared to photons, electrons, mesons, or high-energy protons, are categorized as high-LET radiation (Figure 2.3) (Goodhead, 1988; Goodhead, 1994).
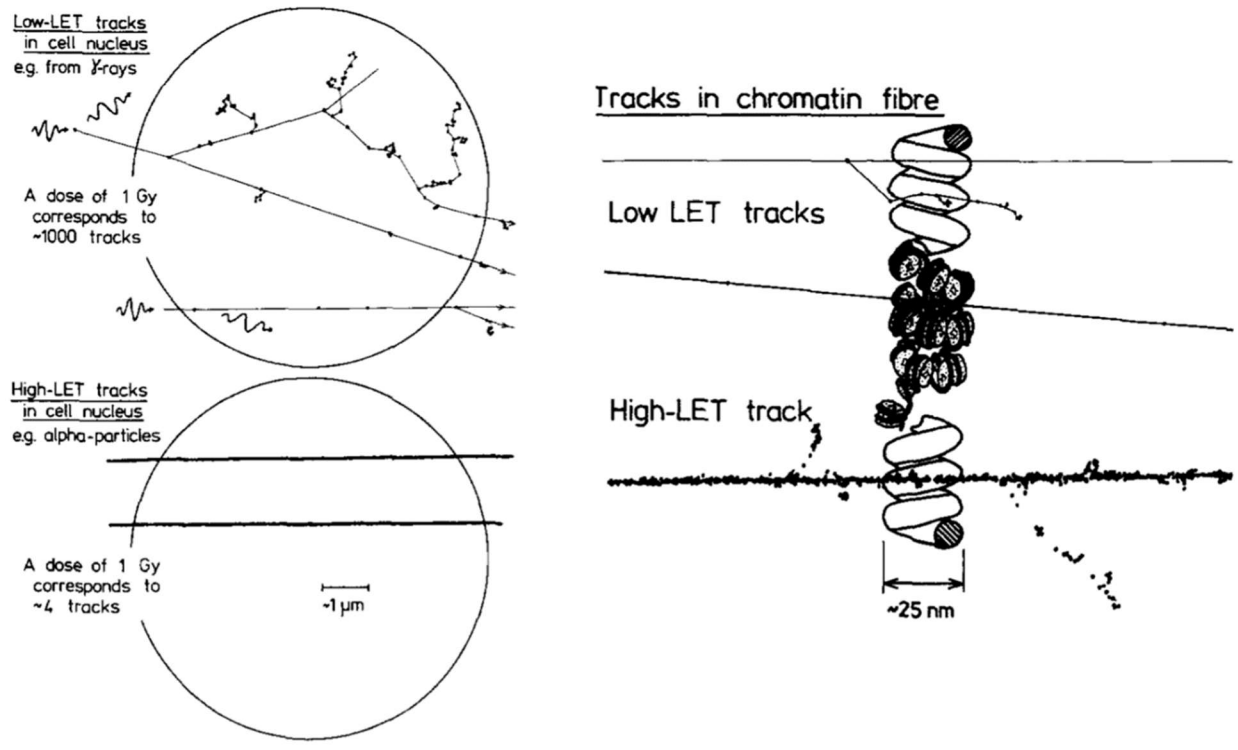
Figure 2.3. Illustration of low- and high-LET radiation tracks in a cell nucleus (left) and on the scale of chromatin fiber (right). High-LET radiation induces significantly more ionizations and excitations along its track over a short distance. Image reprinted from Goodhead (1994).

2.1.2: Physical Characteristics of Neutrons

Neutrons, while not typically present in space radiation spectra, are generated during interactions between spacecraft shielding materials or human tissues and the primary space radiation, which consists of ions. Unlike ions, neutrons lack an electrical charge, rendering them unable to interact with matter through the Coulomb force. Neutrons primarily interact with the nuclei in a material, and these interactions encompass elastic scattering, inelastic scattering, and neutron-induced nuclear reactions (Krane, 1987; Knoll, 2010). The nature of neutron interactions depends on their energy or speed.

For slow neutrons with 0.5 eV or less energy, neutron-induced nuclear reactions, such as the radiative capture reaction, are most commonly utilized to transfer energy to the material, while a negligible amount of energy can also be transferred by elastic scattering. In radiative capture, neutrons are absorbed by matter, leading to the production of mostly secondary gamma-rays, while the occurrence of secondary charged particles is low. When fast neutrons with 0.5 eV or greater energy interact with matter, secondary radiation takes the form of charged particles, additional neutrons, or recoil nuclei, causing the incident neutrons to lose energy. High-energy fast neutrons may also undergo inelastic scattering by nuclei, emitting gamma-rays, and losing energy.

At energies above 10 MeV, neutrons cause spallation and fragmentation reactions, while for neutrons with energy above 290 MeV, meson production becomes possible. Neutrons are a secondary source of radiation in space, and their energy spectra at production resemble that of the primary GCR or SPE energy spectra. However, the neutron fluence spectra increase at lower energies due to further neutron production in cascade and evaporation reactions by secondary neutrons or charged particles. Neutron production cross-sections generally increase with the target mass number, making materials such as iron or lead prohibitive for shielding in space (Wilson et

al. 1995a). This tendency is clearly shown in Figure 2.4, where the differential neutron production energy cross-sections for 800-MeV protons incident on 1 g/cm^2 thick carbon, aluminum, iron, and lead targets are illustrated (Amian et al., 1992).

The probability of interaction of monoenergetic neutrons is expressed by the cross-section (σ), and the first-order neutron intensity (I) attenuation in the absorbing material is described by:

$$I = I_0 e^{-\sigma n x}, \tag{2.7}$$

where I_0 is the initial neutron intensity, n is the number of atoms per unit volume, and x is the thickness of the absorbing material. The total cross-section (σ_{total}) is the summation of the cross-sections for each reaction:

$$\sigma_{total} = \sigma_{inelasticScattering} + \sigma_{elasticScattering} + \sigma_{radiativeCapture} + \cdots. \tag{2.8}$$

Neutrons lose energy in each interaction. For instance, the change in energy due to an elastic collision is described by:

$$\frac{E}{E_0} = \frac{A^2 + 1 + 2A\cos\theta}{(A+1)^2}, \tag{2.9}$$

where E_0 is the initial neutron energy, E is the neutron energy after interaction, A is the mass of an atom in the material, and θ is the scattering angle. After multiple scatterings, neutron energy follows a Maxwellian distribution:

$$f(E)dE = \frac{2\pi n}{(\pi kT)^{3/2}} E^{1/2} e^{-E/kT} dE, \tag{2.10}$$

where *f(E) dE* indicates the proportion of neutrons possessing energies within the range *E* to *E* +

dE, *k* stands for the Boltzmann constant, *T* denotes the thermodynamic temperature, and *n* signifies

the number of neutrons per unit volume.
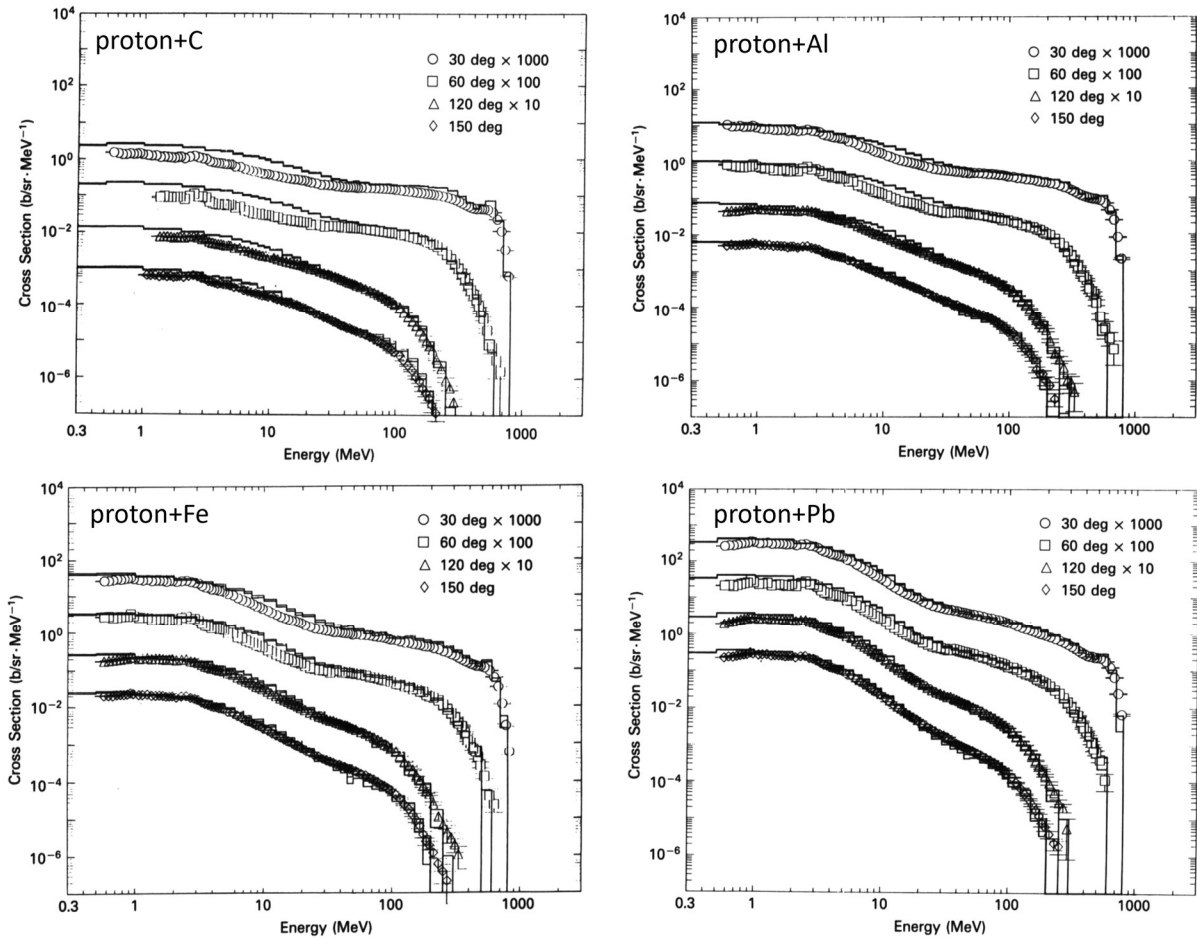
Figure 2.4. Differential neutron production cross-sections. Experimental data for neutrons generated with 30, 60, 120, and 150 degrees for 800-MeV protons incident on 1 g/cm^2 thick carbon, aluminum, iron, and lead are illustrated. Solid lines are the values calculated using the high-energy transport code (HETC) with the intranuclear-cascade evaporation model. Image reprinted from Amian et al. (1992).

2.1.3: Physical Characteristics of Mesons

Mesons consist of a quark and an antiquark, constituting subatomic particles with a short lifetime (Krane, 1987). Charged pi mesons (pions) and charged K mesons (kaons), akin to secondary neutrons, are produced as secondary radiation in space. Pions and kaons are generated by the interactions between nucleons, nuclei, or mesons (Rosenfeld, 1975; Cucinotta, Wilson, & Norbury, 1998a). Assuming N is any nucleon or nucleus, M is a meson, and X is reaction products, the meson generation can be expressed as:

$$N + N \rightarrow M + X, \tag{2.11}$$

$$M + N \rightarrow M + X. \tag{2.12}$$

For instance, reactions leading to the generation of positive (π^+) and negative (π^-) pions and positive (K^+) and negative (K^-) kaons include:

$$p + p \rightarrow p + n + \pi^+, \tag{2.13}$$

$$\pi^+ + p \rightarrow \pi^+ + \pi^+ + n, \tag{2.14}$$

$$p + n \rightarrow p + p + \pi^-, \tag{2.15}$$

16

$$\pi^- + p \rightarrow n + K^+ + K^-, \qquad\qquad (2.16)$$

$$p + p \rightarrow \pi^+ + d, \qquad\qquad (2.17)$$

where p is a proton, n is a neutron, and d is a deuteron.

Positive and negative pions have 139.57 MeV of a rest mass, approximately 14.9% of the proton mass. They undergo weak decay to charged leptons (electrons ($e^\pm$) or muons ($\mu^\pm$)) and their respective neutrinos, with a lifetime of 2.54×10^{-8} seconds:

$$\pi^\pm \rightarrow \mu^\pm + \overline{\nu}_\mu \qquad (\approx 100\%) \qquad\qquad (2.18a)$$

$$\rightarrow e^\pm + \overline{\nu}_e \qquad (1.23 \times 10^{-4}) \qquad\qquad (2.18b)$$

$$\rightarrow \mu^\pm + \overline{\nu}_\mu + \gamma \qquad (1.24 \times 10^{-4}) \qquad\qquad (2.18c)$$

$$\rightarrow e^\pm + \overline{\nu}_e + \gamma \qquad (5.6 \times 10^{-8}) \qquad\qquad (2.18d)$$

$$\rightarrow e^\pm + \overline{\nu}_e + \pi^0 \qquad (1.03 \times 10^{-8}) \qquad\qquad (2.18e)$$

Positive and negative kaons, with a rest mass of 493.68 MeV (0.526 times the proton mass), decay with a lifetime of 1.24×10^{-8} seconds and emit pions or leptons and their respective neutrinos:

$$K^{\pm} \rightarrow \mu^{\pm} + \nu_{\mu} \qquad (63\%) \qquad\qquad (2.19a)$$

$$\rightarrow \pi^{\pm} + \pi^{0} \qquad (21\%) \qquad\qquad (2.19b)$$

$$\rightarrow \pi^{\pm} + \pi^{\pm} + \pi^{\mp} \qquad (6\%) \qquad\qquad (2.19c)$$

$$\rightarrow \pi^{\pm} + \pi^{0} + \pi^{0} \qquad (2\%) \qquad\qquad (2.19d)$$

$$\rightarrow \pi^{0} + \mu^{\pm} + \nu_{\mu} \qquad (3\%) \qquad\qquad (2.19e)$$

$$\rightarrow \pi^{0} + e^{\pm} + \nu_{e} \qquad (5\%) \qquad\qquad (2.19f)$$

$$\rightarrow e^{\pm} + \mu_{e} \qquad (0.0015\%) \qquad\qquad (2.19g)$$

The energy of charged mesons in the material is expressed by the Bethe formula (Equation 2.3). However, their reduced mass and short lifetime result in increased scattering and quick decay (Attix, 2008). Negative pions, in particular, are notable for their unique characteristics in dose delivery to matter. At the end of their track in human tissue, they are typically absorbed by oxygen, producing nuclear fragments. Of the 139.57 MeV rest mass of pions, around 40 MeV is used to overcome binding energy, approximately 30 MeV is given to ions, and neutrons take around 70 MeV. The presence of these secondary particles with high LET allows for increased dose delivery

to critical human organs in space exploration. In addition, the absorption of a negative muon in the material produces a muonic atom, followed by photon emission described by the modified Fermi-Teller law (Mokhov & Van Ginneken, 1999; Pak & Cucinotta, 2024).

2.1.4: Biomedical Aspects

When incident particles enter biological material, they induce chemical and biological changes through direct or indirect action (Figure 2.5) (Goodhead, 1999; Hall & Giaccia, 2018). In indirect action, secondary electrons arising from radiation-matter interactions generate free radicals, damaging the target, typically deoxyribonucleic acid (DNA) (Dertinger & Jung, 1970; Desouky, Ding, & Zhou, 2015). Conversely, direct action involves the direct ionization of the target by primary radiation or secondary electrons. Ions and neutrons may exhibit both actions, but direct action dominates, resulting in increased lethal damage (Hirayama et al., 2009). Complex DNA damage can also occur, involving a mixture of direct and indirect damage, denoted as hybrid DNA damage (Goodhead & Nikjoo, 1997).
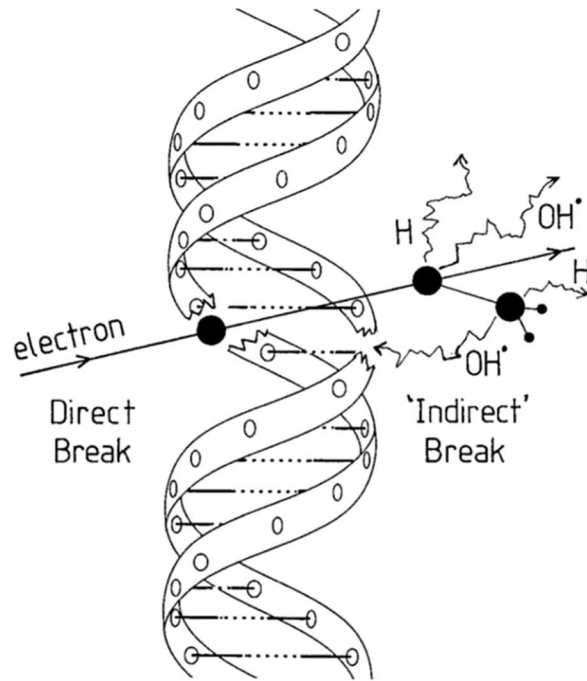
Figure 2.5. Schematic representation of direct and indirect action causing DNA damage. Image reprinted from Goodhead (1999).

High-LET radiation, such as hadrons, causes the same level of biological changes with less dose compared to low-LET radiation, such as photons, due to more ionizations in a short distance, leading to clustered damage sites (Butts & Katz, 1967). This is particularly evident at a microscopic level, where complicated double-strand breaks (DSBs) of DNA are more easily caused. The Relative Biological Effectiveness (RBE) quantifies the ratio between the dose of reference radiation (Cobalt-60 gamma-rays) and the dose of test radiation necessary to produce equivalent biological effects. While RBE depends on many factors, including biological endpoint, particle energy, particle type, dose, fractionization, oxygen level, and cell type, ions generally have a higher RBE than photons and light charged particles. Notably, the increased tumor incidence followed by exposure to high-LET radiation with high RBE compared to low-LET radiation has been indicated by experimental studies, as shown in Figure 2.6 (Fry et al., 1985).

For space radiation, secondary electrons generated along the ion's track play a significant role in energy transfer. These "delta-rays" with energies high enough to lead additional ionizations to the proximity of target atoms contribute ~80% of the LET of an incident ion (Cucinotta, Kim, & Chappell, 2011b). While LET does not account for ion track widths, which increase with ion speed, the ICRP publications express the radiation quality factor solely based on LET (L) (ICRP, 1991; ICRP, 2007), which is not appropriate for space radiation protection. Hence, the state-of-the-art NSCR model has been developed and updated by Cucinotta and his colleagues (Cucinotta, Kim, & Chappell, 2012; Cucinotta, Kim, & Chappell, 2013a; Cucinotta, To, & Cacao, 2017; Cucinotta et al., 2020a; Cucinotta & Saganti, 2022a; Cucinotta, 2022b), which adopts a track structure approach of "core" and "penumbra" in biological effects (Figure 2.7) (Cucinotta, 2024). As the generation of delta-rays is closely related to the incident particle's energy (E) and charge number (Z), the radiation quality factor in the NSCR model is expressed by E and Z.
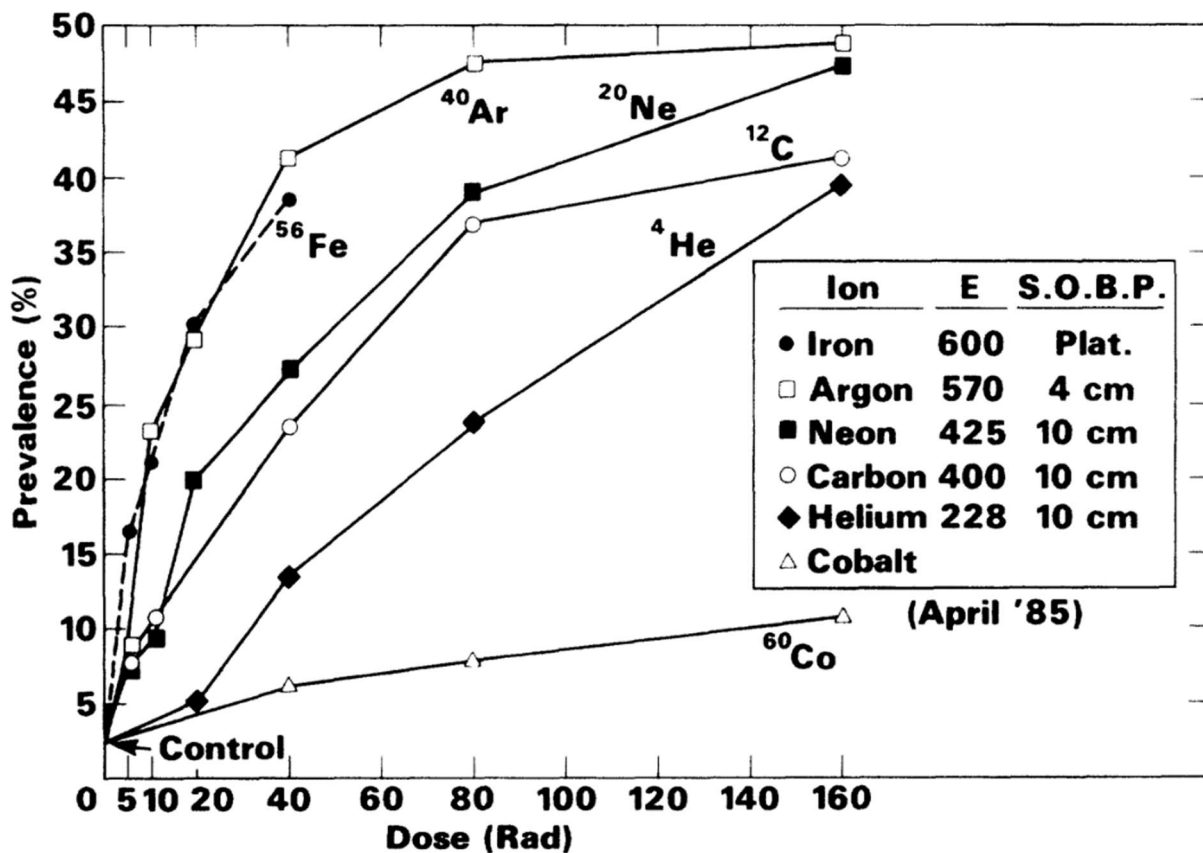
Figure 2.6. Mouse Harderian gland tumor incidence rate. High-LET radiation (228 MeV/u [4]He with the RBE of 5, 400 MeV/u ^{12}C with the RBE of 12, 425 MeV/u [20]Ne with the RBE of 18, 570 MeV/u [40]Ar with the RBE of 27, and 600 MeV/u [56]Fe with the RBE of 27) possess higher prevalence compared to low-LET radiation (^{60}Co gamma-rays) for the same dose. Image reprinted from Fry et al. (1985).

The health effects caused by radiation exposure can be broadly classified into stochastic and deterministic effects (Hall & Giaccia, 2018; Martin et al., 2018). Stochastic effects lack a dose threshold, manifesting even at low radiation exposure, with severity independent of dose but probability increasing with dose. Carcinogenesis and genetic effects fall under stochastic effects. In contrast, deterministic effects have a dose threshold, and their severity is related to the amount of dose. Acute radiation effects, such as prodromal syndromes and fatalities from hematopoietic, gastrointestinal, and cerebrovascular syndromes, are examples of deterministic effects.

$$Q_{NASA} = (1 - P(Z,E)) + \frac{6.24(\Sigma_0 / \alpha_\gamma)}{LET} P(Z,E)$$
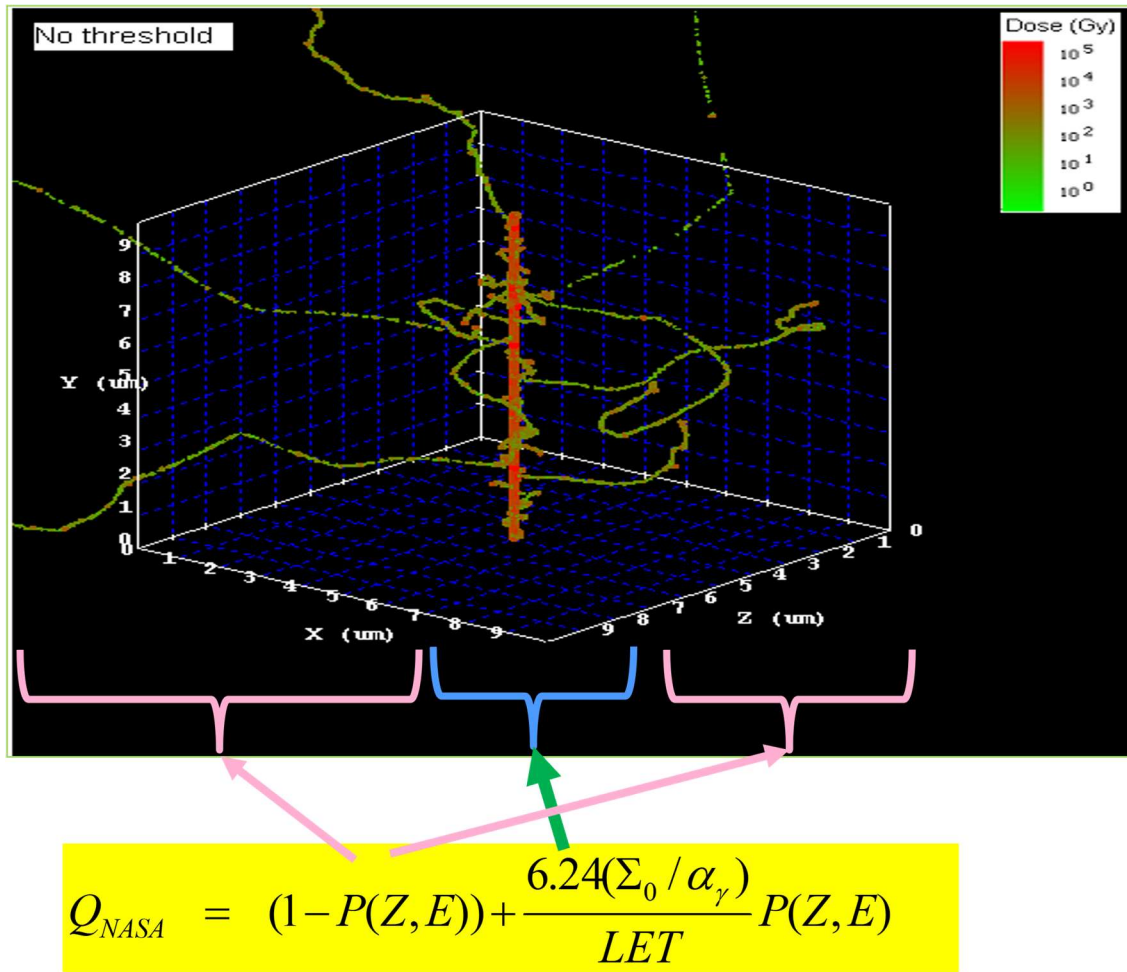
Figure 2.7. 1 GeV ^{56}Fe ion track structure illustrating "core-like" and "penumbra-like" terms in the NSCR model. Image reprinted from Cucinotta (2024).

Exposure to hadron irradiation can occur through various means, including environmental radon exposure, involvement in a radiation accident or atomic bomb incident, medical treatments, or during space travel (Cullings, Pierce, & Kellerer, 2014; Mortezaee et al., 2019). Research indicates that exposure to ions, neutrons, or mesons can elevate the risks of heritable mutations, cancer, cognitive impairment, and other health issues (Fry et al., 1985; Todd, 1992; Kim, Rusek, & Cucinotta, 2015; Mortezaee et al., 2019).

In the context of space exploration, where more than 10% of GCRs consist of helium or heavier nuclei, and highly energetic protons are prevalent in SPE and GCR spectra (Figure 2.8), additional evidence of health concerns arises (Simpson, 1983; Badhwar & O'Neill, 1994; Phillips, 1995; Rauch & CALET Collaboration, 2014; Guo et al., 2015). As shown in Figure 2.9, studies on crews participating in space missions have reported complex chromosomal damage in lymphocyte cells (Cucinotta et al., 2008). Chronic exposure to high LET radiation has been associated with a heightened risk of central nervous system (CNS) malfunction (Hienz et al., 2010). Solar particles may contribute to hematological abnormalities, prodromal effects, and immune system problems if not shielded, while GCR heavy ions can penetrate shielding, leading to damage to biomolecules, cells, and organs (Kim, George, & Cucinotta, 2006).

Given the chronic radiation exposure faced by crews for long-term space exploration, the risk of cardiovascular diseases and stochastic effects, including genetic mutations and tumorigenesis, significantly rises for astronauts who participated in missions beyond LEO (NCRP, 2006). This underscores the significance of understanding and mitigating the health implications of radiation exposure in space radiation.
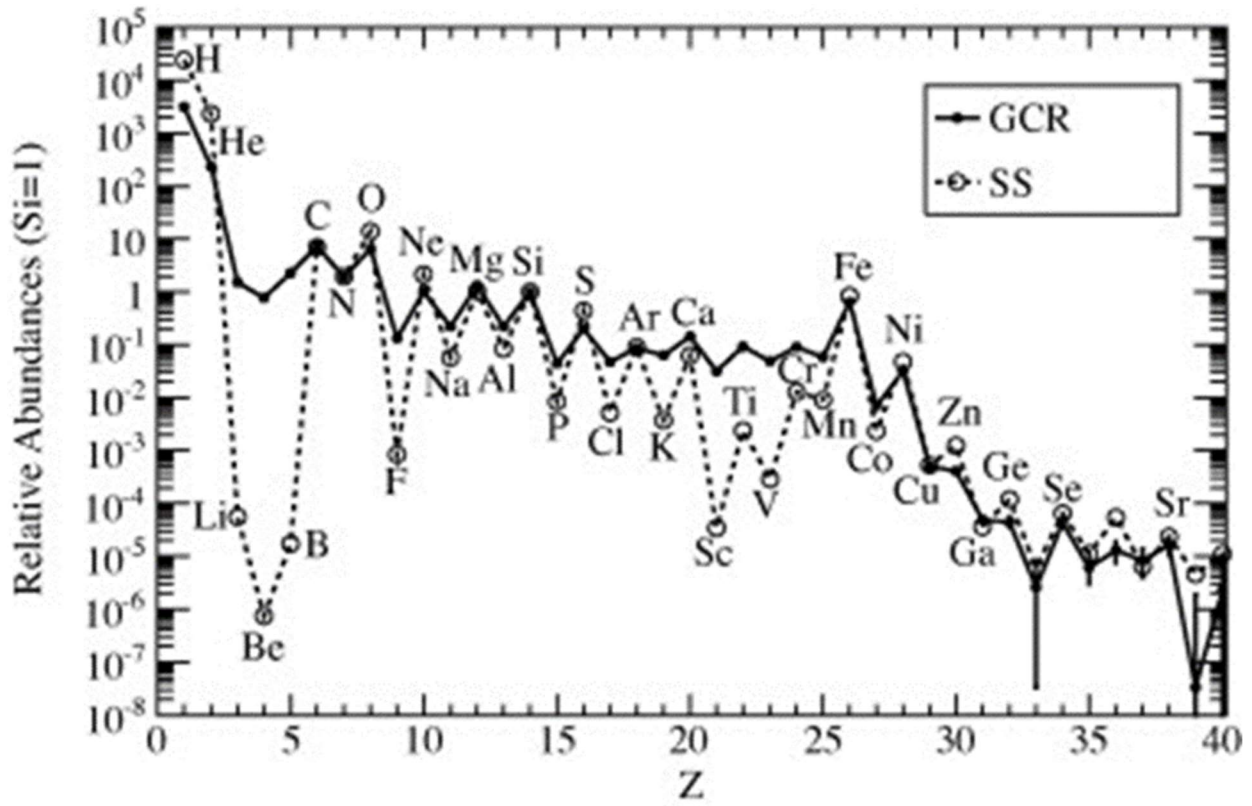
Figure 2.8. Relative abundances of ions in space radiation at the energy of 2 GeV/u, normalized by silicon. GCR stands for the galactic cosmic ray, and SS stands for the solar system. Image reprinted from Rauch & CALET Collaboration (2014).
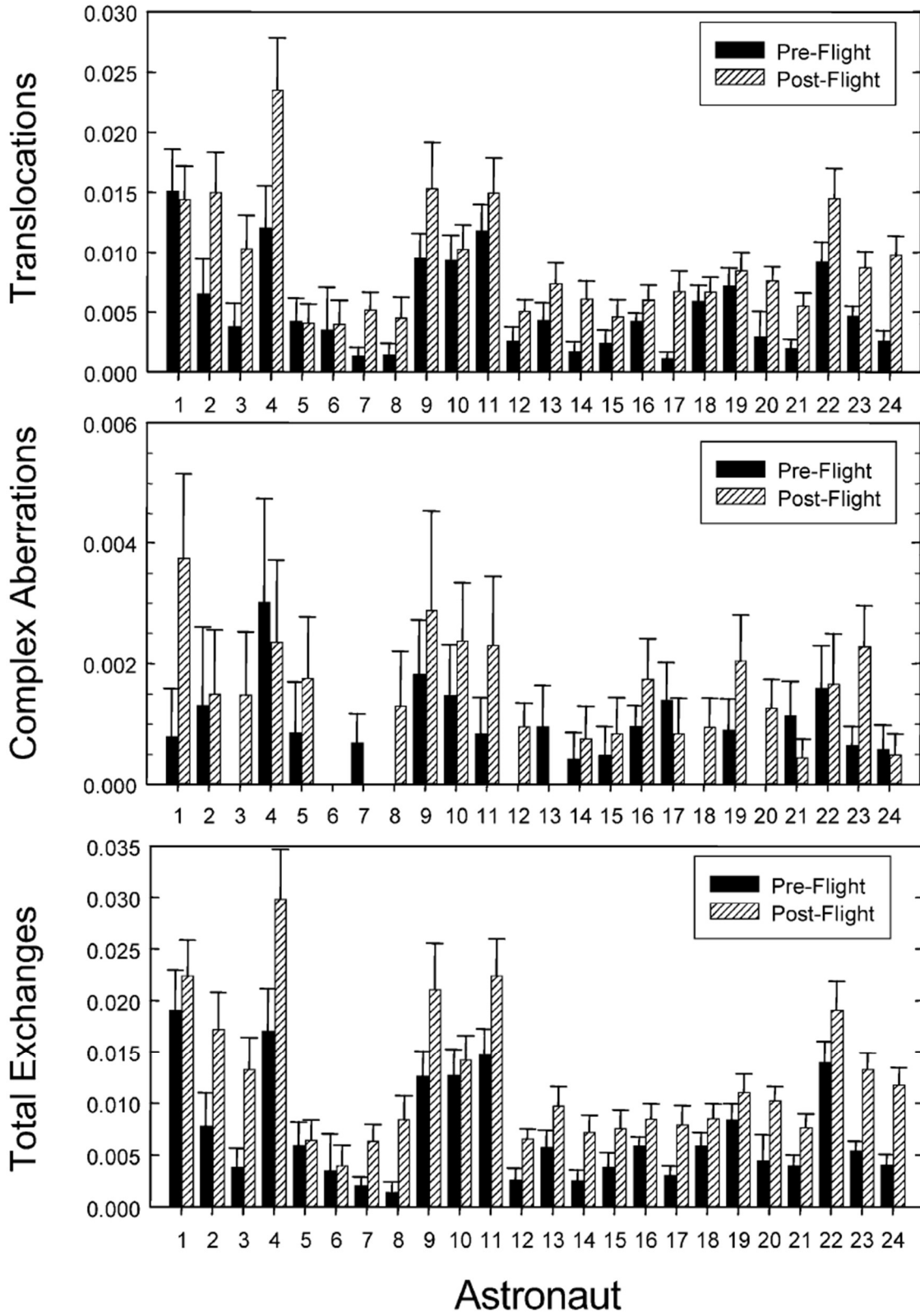
Figure 2.9. Frequency of chromosomal aberrations in blood lymphocytes before and after space mission. Image reprinted from Cucinotta et al. (2008).

2.2: Monte Carlo Simulation

2.2.1: Overview

The Monte Carlo method stands as a statistical paradigm for addressing intricate mathematical problems, encompassing integrodifferential equations, by employing numerous pseudo-random numbers (Metropolis & Ulam, 1949; Sawilowsky, 2003). The Monte Carlo simulation involves representing physical phenomena through iterative random sampling to derive numerical values. The inception of utilizing random sampling for integral calculations traces back to the work on Buffon's needle problem (Leclerc & de Buffon, 1777), signifying the pioneering application of this approach. Subsequent applications included diverse problem domains (Kalos & Whitlock, 2009), such as the evaluation of π (de Laplace, 1820) and the computation of integrals related to the kinetic energy of gases (Kelvin, 1901). The contemporary Monte Carlo method is attributed to physicist Enrico Fermi, who employed it to investigate neutron diffusion and tackle various mathematical challenges (Metropolis, 1987; Kalos & Whitlock, 2009). Further advancements were made by a cadre of scientists, including Nicholas Constantine Metropolis, John von Neumann, and Stanislaw Marcin Ulam, during the 1940s and 1950s. Notably, it played a crucial role in research on neutron diffusion and the Manhattan Project (Ulam, Richtmyer, & von Neumann, 1947; Haigh, Priestley, & Rope, 2014). The nomenclature "Monte Carlo" was suggested by Metropolis and Ulam, referencing the Monte Carlo Casino in Monaco, serving as a code name during the Manhattan Project (Manno, 1999; Mazhdrakov, Benov, & Valkanov, 2018).

In April 1948, the inaugural computational Monte Carlo simulation code was executed on the Electronic Numerical Integrator and Computer (ENIAC), marking a significant milestone as the first electronic computer in history. This simulation addressed a spectrum of challenges in neutron transportation (Metropolis, 1987; Haigh, Priestley, & Rope, 2014).

Monte Carlo simulation has witnessed rapid evolution and widespread adoption due to its manifold advantages over traditional methods for locating and solving differential equations. Its applications span diverse fields, including engineering (Mazhdrakov, Benov, & Valkanov, 2018), physical sciences (Gubernatic & Los Alamos National Laboratory, 2003), biology (Mode, 2011), finance (Jäckel, 2002), and various other research disciplines (Harrison, 2010). The versatility and efficacy of Monte Carlo simulations have established them as an indispensable tool in contemporary scientific and computational endeavors.

2.2.2: Random Number and Sampling

Monte Carlo simulation, inherently based on a sequence of random events (Kalos & Whitlock, 2009), faces the challenge that digital computers cannot generate perfect random number distributions (Gentle, 2003; Rubinstein & Kroese, 2016). Consequently, random number generators come into play, offering so-called pseudo-random numbers that exhibit a semblance of randomness and are drawn from known distributions. To qualify as valid, generated pseudo-random numbers should exhibit identity and independent over an extensive number of sampling trials ($>10^8$) (Gentle, 2003). Various methods have been developed and adopted for generating pseudo-random numbers, with examples including the linear congruential generator (Lehmer, 1951) and its variations (Gentle, 2003), as well as different non-linear congruential generators (Eichenauer & Lehn, 1986).

The linear congruential generator stands out as the most widely employed method for creating random numbers in Monte Carlo calculations (Manno, 1999; Gentle, 2003; Rubinstein & Kroese, 2016). In this generator, the i-th random number, x_i, is computed by the formula:

$$x_i = (ax_{i-1} + c) \bmod m. \tag{2.20}$$

Here, a is the multiplier, c is the increment, and m is the modulus. Essentially, x_i represents the remainder when $(ax_{i-1} + c)$ is divided by m. Parameters a, c, and m must be carefully selected non-negative integers. The initial random number, x_0, is referred to as the seed, initiating a sequence of the random number generation called a Lehmer sequence. If c is zero, the generator is termed a multiplicative congruential generator, providing a faster computation yet still effective. In a case

where c is non-zero, it is known as a mixed congruential generator. Random numbers in Monte Carlo simulation codes are typically normalized to fall within the range of 0 to 1:

$$u_i = \frac{x_i}{m}. \tag{2.21}$$

A sequence of the random number generation repeats at most m steps, returning to the cycle's seed and restarting the entire series. Hence, choosing a large value for m is preferable to simulate a substantial number of natural random events, selected as:

$$m = 2^\beta \tag{2.22}$$

for a binary system, where β is the length of the computer word, such as 32 or 64. To ensure independence and uniformity in the generated series of pseudo-random numbers, several statistical tests can be employed, including the Kolmogorov-Smirnov goodness-of-fit test, serial test, and chi-square goodness-of-fit test (Gentle, 2003; Rubinstein & Kroese, 2016).

Having obtained pseudo-random numbers in a uniform distribution between 0 and 1, the next step involves generating random variables or random variates with known probability distribution functions. This process, known as the sampling of random variates, employs various methods for complex distributions, including the composition method, rejection method (also known as acceptance-rejection method), ratio-of-uniforms method, and alias method (Gentle, 2003; Rubinstein & Kroese, 2016). In cases where the probability density function of variates of x between a and b, denoted as $f(x)$, is simple, direct methods or the invertible cumulative distribution

function method can be applied for sampling (Manno, 1999; Bielajew, 2001). The cumulative

distribution function of values of x is defined as:

$$F(x) = \int_a^x f(x')dx',$$

(2.23)

with the inverse function is given by:

$$x = F^{-1}(y).$$

(2.24)

Then, random variables are generated using the equation:

$$x = F^{-1}(u),$$

(2.25)

where u represents a random number in a uniform distribution between 0 and 1. For example, let

us consider generating a random variable from a simple exponential probability density function:

$$f(x) = ce^{-cx}, \qquad 0 \le x < \infty.$$

(2.26)

Here, c is a constant, and the cumulative density function is given by:

$$F(x) = \int_0^x ce^{-cx'}dx' = 1 - e^{-cx} = u.$$

(2.27)

Thus, the random variable x is generated as:

$$x = -\frac{\ln(1-u)}{c}. \tag{2.28}$$

Another application involves generating a random direction of a particle from an isotropic point source (Figure 2.10). For $0 \leq \theta \leq \pi$ and $0 \leq \varphi < 2\pi$, the probability density function for the endpoint of the unit vector of the particle, uniformly distributed on a spherical surface with a radius of 1, is:

$$f(\varphi,\theta)d\varphi d\theta = \frac{\sin\theta d\theta d\varphi}{4\pi} = \frac{\sin\theta d\theta}{2}\frac{d\varphi}{2\pi}. \tag{2.29}$$

As θ and φ are independent, their probability density functions are separated:

$$f_\theta(\theta) = \int_0^{2\pi} f(\varphi,\theta)d\varphi = \frac{\sin\theta}{2}, \tag{2.30a}$$

$$f_\varphi(\varphi) = \int_0^{\pi} f(\varphi,\theta)d\theta = \frac{1}{2\pi}. \tag{2.30b}$$

The cumulative density functions are then:

$$F_\theta(\theta) = \int_0^{\theta} \frac{\sin x'}{2}dx' = \frac{1-\cos\theta}{2} = u_1, \tag{2.31a}$$

$$F_\varphi(\varphi) = \int_0^\varphi \frac{1}{2\pi} dx' = \frac{\varphi}{2\pi} = u_2. \tag{2.31b}$$

This leads to the initial angles of the particle given by:

$$\theta = \arccos(1 - 2u_1), \tag{2.32a}$$

$$\varphi = 2\pi u_2, \tag{2.32b}$$

and the rectangular components of the unit vector of the initial directors are:

$$x = \sin\theta \cos\varphi, \tag{2.33a}$$

$$y = \sin\theta \sin\varphi, \tag{2.33b}$$

$$z = \cos\theta. \tag{2.33c}$$
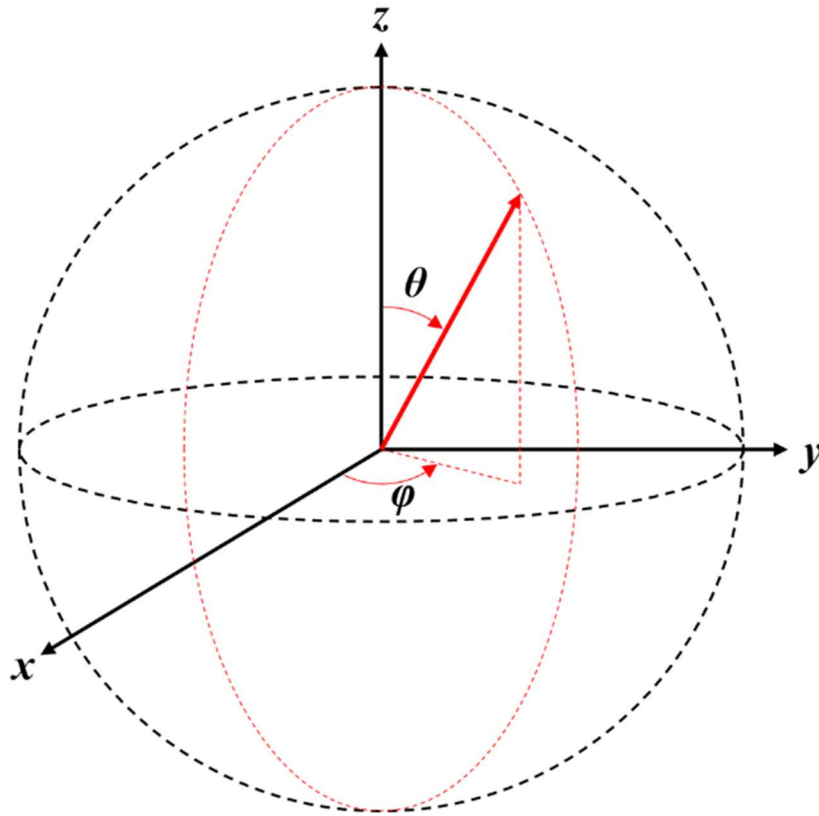
Figure 2.10. Isotropic point source. Polar angle θ and azimuthal angle φ of the initial particle are given by $\theta = \arccos(1-2u_1)$ and $\varphi = 2\pi u_2$, where two random numbers, u_1 and u_2, present in a uniform distribution between 0 and 1.

2.2.3: Particle Transport in Monte Carlo Method

Understanding the probability of physical interactions between particles and matter has been a subject of research for over a century. Given that radiation transport is inherently stochastic, Monte Carlo methods prove suitable for simulating the physical events during particle movement (Kalos & Whitlock, 2009).

In Monte Carlo toolkits, particle transport is typically computed step by step (Agostinelli et al., 2003; Geant4 Collaboration, 2021). The step length is randomly sampled by the interaction length, denoted as the mean free path (λ), which is given by:

$$\lambda(E) = \frac{1}{\sum_i [n_i \sigma(Z_i, E)]}. \tag{2.34}$$

Here, $\sigma(Z, E)$ is the total cross-section per atom, n_i is the number of atoms of element i, computed by $n_i = N\rho w_i/A_i$, N is Avogadro's number, ρ is the medium density, w_i is the mass proportion of element i, and A_i is the mass of a mole of element i.

The number of mean free paths between two interaction points, n_λ, is sampled by:

$$n_\lambda = -\log(\eta), \tag{2.35}$$

where a random number η is uniformly chosen between 0 and 1.

Charged particles continuously lose energy while penetrating a medium. The mean energy loss in the Monte Carlo method is calculated by:

$$\frac{dE(E,T_{cut})}{dx} = n_{at} \int_0^{T_{cut}} \frac{d\sigma(Z,E,T)}{dT} T dT. \qquad (2.36)$$

In this formula, n_{at} is the number of atoms in the unit volume of the matter, T and T_{cut} are the kinetic energy of the secondary particle and cut-off, E is the total energy of the incident particle, and $d\sigma(Z,E,T)/dT$ is the differential cross-section per atom with atomic number Z.

In the initialization phase of the simulation, mean free paths, cross-sections, and mean energy losses are tabulated for particle transportation.

In some Monte Carlo toolkits, including Geant4 and PHITS, an algorithm called ATomic Interaction with MAtter (ATIMA) is implemented to predict ion energy loss. In this algorithm, the energy loss per unit path length is denoted as:

$$\frac{dE}{dx} = \left(\frac{dE}{dx}\right)_{inela} + \left(\frac{dE}{dx}\right)_{ela}, \qquad (2.37)$$

where the inelastic portion is:

$$\left(\frac{dE}{dx}\right)_{inela} = 2\pi r_e^2 mc^2 n_{el} \frac{<q>^2 Z_T}{A_T \beta^2} \left(\left[\ln\left(\frac{2mc^2\beta^2\gamma^2}{I^2}\right) - \beta^2 - \frac{C}{Z_T}\right] B + LS - \frac{\delta}{2}\right), \qquad (2.38)$$

and the elastic contribution is:

$$\left(\frac{dE}{dx}\right)_{ela} = \frac{846.21 \times 10^{-23} Z_P Z_T A_P A_v X}{A_T A_{sum} A_{pow}}. \qquad (2.39)$$

36

Here, $r_e = e^2/(4\pi\epsilon_0 mc^2)$ signifies the electron radius, n_{el} represents the electron density within the material under consideration, I stands for the mean excitation energy of the material, A_T and Z_T denote the mass number and nuclear charge number of the target material, $<q>$ signifies the average ion charge (Pierce & Blann, 1968), $\gamma = E/mc^2$, $\beta^2 = 1 - \gamma^{-2}$, C is the Shell correction function, B represents the Barkas term, incorporating polarization effect (Jackson & McCarthy, 1972), LS includes nuclear size effects for relativistic ions (Lindhard & So, 1996), δ stands as the density effect function (Sternheimer & Peierls, 1971), A_P and Z_P denote the mass number and nuclear charge number of the projectile, $A_{sum} = A_T + A_P$, $Z_{pow} = Z_T^{0.23} + Z_P^{0.23}$, and $X = ln(\epsilon)/2\epsilon$ for $\epsilon > 30$ or $X = 0.5 ln(1 + 1.01323\epsilon)/(\epsilon + 0.01321\epsilon^{0.21226} + 0.19593\epsilon^{0.5})$ for $\epsilon \leq 30$, where $\epsilon = 32530 A_T A_P E_P / (Z_T Z_P A_{sum} Z_{pow})$ with E_P is the total energy [keV/u] of the projectile.

In the realm of Monte Carlo simulation for heavy ion transport, the heavy ion cross-section can be derived from the cross-section of a proton with the same speed (Dingfelder et al., 1971; Plante & Cucinotta, 2011):

$$\frac{d\sigma_{ion}(v)}{dW} = Z^2 \frac{d\sigma_{proton}(v)}{dW}. \tag{2.40}$$

Here, σ_{ion} stands for the cross-section of heavy ion, σ_{proton} represents the cross-section of a proton, consisting of ionization and excitation cross-sections, v is the incident particle speed, Z denotes the heavy ion charge number, and W signifies the energy loss by interaction. The charge number Z is often replaced by the effective charge number Z^* (Barkas, 1953), which accounts for the changing charge of an ion due to capture or loss of electrons as its speed varies:

$$Z^* = Z\left[1 - \exp\left(-\frac{125\beta}{Z^{2/3}}\right)\right], \qquad (2.41)$$

where β is the speed of particle relative to the speed of light.

As discussed in Chapter 2.1.1, ions predominantly interact with material via Coulombic collisions with atomic electrons, leading to ionizations and excitations. The ionization process of electrons in liquid water irradiated by protons can be described by a semi-empirical formula (Rudd, 1990):

$$\frac{d\sigma_{io}^i}{dw} = \frac{S_i}{I_i} \frac{F_1 + F_2 w}{(1+w)^3 (1 + e^{-\alpha(w - w_c)/v})}. \qquad (2.42)$$

Here, $d\sigma_{io}^i / dw$ is the differential ionization cross-section for the orbital i, $w = W/I_i$, where W is the secondary electron energy, and I_i is the electron binding energy. Additionally, $v = (T/I)^{0.5}$, where $T = E_P(m/M_P) = E_P(m/M_P) = E_P/1836$ for the primary proton energy E_P, proton mass M_P, and electron mass m. The cut-off energy $w_c = 4v^2 - 2v - R/4I_i$, and $S_i = 4\pi a_0^2 N_i (R/I_i)^2$, where $a_0 = 52.9$ picometers is the Bohr radius, N is the number of electrons, and $R = 13.6$ eV is the Rydberg unit of energy. The dimensionless parameters F_1 and F_2 depend on the primary proton energy E_P or v:

$$F_1(v) = L_1 + H_1, \qquad (2.43a)$$

$$F_2 = \frac{L_2 H_2}{L_2 + H_2}, \tag{2.43b}$$

where

$$L_1 = \frac{C_1 v^{D_1}}{1 + E_1 v^{D_1+4}}, \tag{2.44a}$$

$$H_1 = \frac{A_1 \ln(1+v^2)}{v^2 + \dfrac{B_1}{v^2}}, \tag{2.44b}$$

$$L_2 = C_2 v^{D_2}, \tag{2.44c}$$

$$H_2 = \frac{A_2}{v^2} + \frac{B_2}{v^4}. \tag{2.44d}$$

Parameters for Equation (2.44) and α are listed in Table 2.2. The total ionization cross-section (σ_{io}^{i}) can then be calculated as the integral:

$$\sigma_{io}^{i} = \int_{0}^{E_{max}+I_i} \frac{d\sigma_{io}^{i}}{dW} dW, \tag{2.45}$$

39

where the maximum energy transfer $E_{max} = 4mME/(M + m)^2$ for electron mass m, ion mass M, and ion energy E.

On the other hand, the excitation process of electrons in liquid water can be described by the following semi-empirical formula (Kutcher & Green, 1976; Plante & Cucinotta, 2011):

$$\frac{d\sigma_{ex}^i}{dW} = \rho(W)Wf_i(W)\ln\left(\frac{4T}{W}\right), \tag{2.46a}$$

$$\rho(W) = \frac{Z^2e^4}{8\pi\varepsilon_0^2 mv^2 W^2} = \frac{4\pi a_0^2 Z^2}{T}\left(\frac{R}{W}\right)^2, \tag{2.46b}$$

where $d\sigma_{ex}^i / dW$ is the differential excitation cross-section for the orbital i, W is the energy loss, ρ is the ion scattering cross-section, f_i is a function defined for different excitation states, $T = E(m / M)$ for ion energy E, electron mass m, and ion mass M, Z represents the ion charge, e stands for the elementary charge, ε_0 denotes the vacuum permittivity, and v is ion speed.

Analogous to the ionization process, the total excitation cross-section is computed through the integral:

$$\sigma_{ex}^i = \int_{0.01}^{100} \frac{d\sigma_{ex}^i}{dW} dW. \tag{2.47}$$

40

Here, the lower (0.01) and upper (100) limits are empirically chosen (Plante & Cucinotta, 2011).

Table 2.2. Parameters for the differential ionization cross-section for electrons in liquid water irradiated by protons. Table reprinted from Plante & Cucinotta (2011).

Parameter	External orbitals	Internal orbitals	Parameter	External orbitals	Internal orbitals
A_1	0.97	1.25	A_2	1.04	1.10
B_1	82.0	0.50	B_2	17.3	1.30
C_1	0.40	1.00	C_2	0.76	1.00
D_1	-0.30	1.00	D_2	0.04	0.00
E_1	0.38	3.00	α	0.64	0.66

2.2.3.1: Nuclear Cross-Section

In Monte-Carlo codes, the total absorption and nuclear elastic cross-sections are used to identify that a nuclear event has occurred in particle transport through a material. Nuclear physics based on optical models provides improved ab initio prediction of total, elastic, and absorptive cross-sections and is used in abrasion-ablation models of heavy ion fragmentation (Bell & Squires, 1959; Townsend et al., 1993). The older form of optical models started from a nonrelativistic time-independent Schrödinger equation with two-body potentials to deal with the nucleus-nucleus multiple scattering in a similar manner to the scattering of light (Bell & Squires, 1959; Krane, 1987). A more interesting formulation considers the multiple scattering series for nucleus-nucleus scattering to derive a one-body Lippman-Schwinger equation based on the double folding of the nucleon-nucleon t-matrix with the target and projectile ground-state densities (Wilson, 1974; Wilson & Townsend, 1981; Townsend, 1983) to form a parameter-free optical model. A two-body optical model is formulated to consider correlations amongst target or projectile nucleons (Cucinotta et al., 1989; Cucinotta et al., 2018).

In nuclear reactions, abrasion and ablation stand for particle removal during interaction and nuclear de-excitation after abrasion, respectively (Cucinotta et al., 2011a). The Geant4 codes use the semi-empirical abrasion-ablation model, and the amount of abraded nuclear material, Δ_{abr}, by interacting with a projectile is expressed by (Wilson et al., 1995b):

$$\Delta_{abr} = FA_P\left[1 - \exp\left(-\frac{C_T}{\lambda}\right)\right], \tag{2.48}$$

where F is the fraction of the projectile, A_P is the mass number of the projectile, $\lambda = 16.6/E^{0.26}$ is mean free path, and C_T is the chord length in the target for maximum interaction probability, which depends on the radius of the target nucleus, $r_T \approx 1.29\sqrt{r_{rms,T}^2 - 0.84^2}$, and the radius of the projectile, $r_P \approx 1.29\sqrt{r_{rms,P}^2 - 0.84^2}$, where r_{rms} stands for root-mean-square charge radius of electron scattering. Where r is the distance between nuclei, C_T is given by:

$$(r_T > r_P) \qquad C_T = \begin{cases} 2\sqrt{r_T^2 - x^2}, & x = \dfrac{r_P^2 + r^2 - r_T^2}{2r} > 0 \\[2mm] 2\sqrt{r_T^2 - r^2}, & x \le 0 \end{cases} \qquad (2.49a)$$

$$(r_T \le r_P) \qquad C_T = \begin{cases} 2\sqrt{r_T^2 - x^2}, & x > 0 \\[2mm] 2r_T, & x \le 0 \end{cases} \qquad (2.49b)$$

On the other hand, the number of ablated projectile nucleons, Δ_{abl}, is represented by:

$$\Delta_{abl} = \frac{E_S + E_X}{10} + \Delta_{spc}, \qquad (2.50)$$

where E_S and E_X are semi-empirical surface excitation energy and total excitation energy, respectively, and $\Delta_{spc} = A_P F \exp(-C_T / \lambda)$ is the number of loosely bounded projectile spectator constituents.

Table 2.3. Parameters for the momentum distribution of the abraded secondary proton. Table reprinted from Cucinotta (1994a).

i	p_i, MeV/c	C_i
1	$\sqrt{2/5}k_F$	1
2	$\sqrt{6/5}k_F$	0.03
3	500	0.003 (0.0002)[a]

The momentum distribution of the abraded secondary proton is formulated by (Cucinotta, 1994a; Geant4 Collaboration, 2021):

$$\psi(p) \propto \sum_{i=1}^{3} C_i \exp\left(-\frac{p^2}{2p_i^2}\right) + d_0 \frac{\gamma p}{\sinh(\gamma p)}. \tag{2.51}$$

Here, p is proton momentum [MeV/c], $\psi(p)$ is the number of secondary protons with momentum p, $d_0 = 1$, $\gamma = 1/90$ c/MeV. Where k_F stands for the Fermi momentum, other parameters are listed in Table 2.3. k_F is 184 MeV/c for ^{12}C, 251 MeV/c for ^{40}Ar, and 265 MeV/c for ^{208}Pb.

The absorption cross-section for a nucleon-nucleus reaction depends on the energy of the projectile (Letaw, Silberberg, & Tsao, 1983). For incident protons with energy greater than 2 GeV, it is given by:

$$\sigma_{abs,H} = 45A^{-0.7}[1 + 0.016\sin(5.3 - 2.63\ln A)] \text{ mb}, \tag{2.52}$$

while for lower energy, the formula is:

$$\sigma_{abs,L} = \sigma_{abs,H} \left[1 - 0.62 \exp(-E/200) \sin(10.9 E^{-0.28}) \right]. \tag{2.53}$$

When it comes to nucleus-nucleus reaction, a Bradt-Peters formula can be used (Bradt & Peters, 1950; Townsend & Wilson, 1986):

$$\sigma_{abs}(A_P, A_T, E) = \pi r_0^2 \beta(E)[A_P^{1/3} + A_T^{1/3} - \delta(A_P, A_T, E)]^2, \tag{2.54}$$

where $\delta(A_P, A_T, E) = 0.2 + A_P^{-1} + A_T^{-1} - 0.292 \exp(-E/792) \cos(0.229 E^{0.453})$, $\beta(E) = 1 + 5E^{-1}$, $r_0 = 1.26$ fm, and the energy of projectile E is in units of MeV/u.

The motion of ions in a nuclear Coulomb field is described by the equation of energy conversion (Wilson et al., 1995b; Geant4 Collaboration, 2021):

$$E_{tot} = \frac{1}{2} \mu \frac{d^2 r}{dt^2} + \frac{l^2}{2\mu r^2} + \frac{Z_P Z_T e^2}{r}, \tag{2.55}$$

where E_{tot} is the total energy in the center of mass frame, $\mu = m_1 m_2/(m_1 + m_2)$ is reduced mass, r is the distance between nuclei, e is electric charge, Z_P and Z_T are charge numbers of the projectile and target, respectively, and l is angular momentum, which is given by $l^2 = 2\mu E_{tot} b^2$. Here, $b = \sqrt{r(r - r_m)}$ is the impact parameter at the distance of closest approach, i.e., $dr/dt = 0$, assuming $r_m = Z_P Z_T e^2 / E_{tot}$. The scattering angle θ has a relation with the impact parameter b:

$$\theta = \pi - 2b \int_{r_{\min}}^{\infty} \frac{dr}{r^2 \sqrt{1 - (b/r)^2 - 2U/mv^2}}, \qquad (2.56)$$

where r_{min} is the distance at the closest approach, m and v are the mass and velocity of the projectile, and U is the potential. In Monte Carlo simulation, the square of impact parameter, b, is sampled uniformly subject to r and not exceeding $r_P + r_T$.

In the microscopic quantum fragmentation model (Cucinotta et al., 1998b; Cucinotta et al., 2006c), the abrasion is described with an impact parameter. Where the pre-fragment is F^*, total momentum transfer, $\mathbf{q}$, is the subtraction of the final target momentum, $\mathbf{p_X}$, from the initial target momentum, $\mathbf{p_T}$, i.e., $\mathbf{q} = \mathbf{p_T} - \mathbf{p_X}$, and b and b' are the impact parameters in state n and n', respectively, the excitation spectrum for the abrasion step is expressed by:

$$\frac{d\sigma}{dE_F} = \left\langle T \left| \int d^2q\, d^2b\, d^2b'\, e^{iq(b-b')} P_{n,n'} \times (b,b',E_{F^*}) \Lambda_{n,n'}(q,b,b',E_{F^*}) \right| T \right\rangle \qquad (2.57)$$

Here, the interaction between the projectile, R, and the target, T, is given by the abrasion response, Λ:

$$\Lambda_{n,n'}(q,b,b',E_{F^*}) = \int \frac{d\mathbf{k}_R}{(2\pi)^3} \left\langle R' \left| Q_{RT}^+(b') \right| R \right\rangle \times \left\langle R \left| Q_{RT}(b) \right| R' \right\rangle \delta(E_i - E_f), \qquad (2.58)$$

where $\mathbf{k}_R$ is the projectile momentum vector, and Q_{RT} is the projectile-target profile operator. On the other hand, the ablation step is described by a Master equation (Cucinotta & Wilson, 1996; Cucinotta et al., 2006c):

$$\frac{df_b(E_b^*,t)}{dt} = \sum_j \int dE f_a(E_b^*,t) P_{a,j}(E) - \sum_k \int dE f_b(E_b^*,t) P_{b,k}(E), \qquad (2.59)$$

where $f_b(E,t)$ is the probability that the nuclei b is shown at time t with excitation energy E_b, and $P_{b,k}(E)$ is the probability of emission of ion k with energy E by the nuclei b. In this equation, gains due to decay of ion a forming ion b by emission of ion j are expressed as the first term on the right-hand side, while losses from decay of ion b to form ion c by releasing ion k are described in the second term. Emitting particles j or k are alpha or lighter particles, such as a proton, deuteron, and tritium.

In PHITS, the Japan Atomic Energy Research Institute (JAERI) Quantum Molecular Dynamics (JQMD) and the Intra-Nuclear Cascade of Liège version 4.6 (INCL4.6) models are used with the ATIMA algorithm to describe hadronic collisions and nucleus interactions (Niita et al., 1995). Information about nucleon state, elastic cross-sections, and inelastic cross-sections in the JQMD model is introduced in Chapter 3.1.4.

2.2.4: PHITS Monte Carlo Simulation Toolkit

In the realm of simulating the intricate processes involved in radiation transport during physical events, where interactions are contingent upon a multitude of parameters such as particle type, energy, target materials, and geometry, the development of Monte Carlo simulation toolkits has been pivotal. Thus, numerous toolkits containing extensive data libraries cater to diverse purposes and emanate from various organizations across different nations. Prominent among the general-purpose Monte Carlo codes are FLUKA (Ferrari et al., 2005; Battistoni et al., 2015; Battistoni et al., 2016), Geant4 (Agostinelli et al., 2003; Allison et al., 2006; Allison et al., 2016), PHITS (Niita et al., 2006; Iwamoto et al., 2017; Sato et al., 2018; Iwamoto et al., 2022; Sato et al., 2024), and MCNP6 (Goorley et al., 2012; Werner, 2017; Werner et al., 2018). In the context of this project, PHITS has been meticulously chosen to facilitate precise primary space ion transport and the derivation of secondary particle yield in shielding materials and human tissues.

As it stands for Particle and Heavy Ion Transport code System, PHITS is specially designed for heavy ion transport due to the increasing necessity of research on space vehicles and heavy ion accelerator facilities (Iwase, Niita, & Nakamura, 2002; Niita et al., 2006). The origin of PHITS is the Nucleon-Meson Transport Code (NMTC), which is written in Fortran IV and developed at Oak Ridge National Laboratory for simulation of the nucleon, muon, and charged pion transport (Coleman & Armstrong, 1970). After several revisions of NMTC at the Los Alamos National Laboratory (LANL) and Brookhaven National Laboratory (BNL), JAERI, a former organization of the Japan Atomic Energy Agency (JAEA), included several functions and models for heavy ions in the revised NMTC and released the JAERI version, which is called NMTC/JAERI (Nakahara & Tsutsui, 1982). In the late 1990s, it was upgraded to NMTC/JAERI97 (Takada et al., 1998) with significant changes encompassing a new geometry model, adopting an intranuclear

cascade model, and the pre-equilibrium calculation model. A few years later, as JAERI needed to extend the energy range of the code for a new accelerator project (Niita et al., 2001), it was combined with a high-energy hadronic cascade model, the Jet AA Microscopic Transport Model (JAM) (Nara et al., 1999), and was named NMTC/JAM. By incorporating the Shen formula for the heavy ion total cross-section, the Fortran program for computing Stopping Powers And Ranges for muons, charged pions, protons, and heavy ions (SPAR) (Armstrong & Chandler, 1973) and JQMD code (Niita et al., 1995), NMTC/JAM became to be able to be used for the heavy ion transport and published with a new name, PHITS (Iwase, Niita, & Nakamura, 2002). PHITS is currently being controlled and updated by several facilities, including the Japan Atomic Energy Agency (JAEA), the Research Organization for Information Science and Technology (RIST), and the High Energy Accelerator Research Organization (Kō Enerugī Kasokuki Kenkyū Kikō, KEK). PHITS has a pre-defined default setting for physics models for different particle types in specific energy ranges (Figure 2.11) (Iwatomo et al., 2017; Sato et al., 2018; PHITS development team, 2022). In PHITS version 3.27, released in March 2022, the physical interactions of the deuteron, tritium, ^{3}He ion, alpha-particle, and hadron, including proton and pion, in the energy range between 1 MeV/u and 3 GeV/u are calculated by INCL4.6 model (Boudard et al., 2013) because it has been validated for hadron transportation and is faster than JQMD. For these particles, JAM (Nara et al., 1999) is adopted in the energy higher than 3 GeV/u, while the ATomic Interaction with MAtter (ATIMA) program is used for the energy lower than 1 MeV/u. JENDL-4.0/He has been newly added in this version for 1 MeV to 200 MeV hadrons; however, it is only recommended to use for accelerator shielding design. Neutron uses similar models to other hadrons; however, the Japanese Evaluated Nuclear Data Library version 4.0 (JENDL-4.0) (Chiba et al., 2011; Iwamoto et al., 2011a; Shibata et al., 2011) is used for the energy lower than 20 MeV. In order to take account of

the evaporation model or for accurate yields of charged particles from low energy neutron reaction, the Event Generator Mode (EGM or E-mode) (Iwamoto et al., 2011b) can be turned on by the users. Nucleon-nucleus reaction follows ATIMA for the energy lower than 10 MeV/u, JQMD between 10 MeV/u and 3 GeV/u, and JAMQMD, a combination of the JAM and JQMD, for the energy higher than 3 GeV/u. For the evaporation of hadrons and nuclei, the GEM code (Furihata et al., 2001), developed from the Atchison fission model and the Generalized Evaporation Model, is utilized. The users have an option of using the Electron-Gamma Shower version 5 (EGS5) for precise transport of electrons, positrons, and photons (Hirayama et al., 2005). The switching energies for physics models can be changed by setting the parameters in the PHITS input file. PHITS calculations have been verified and validated by comparisons with several experiments, results from other Monte Carlo simulation codes, and benchmark studies (Iwase, Niita, & Nakamura, 2002; Niita et al., 2006; Iwamoto et al., 2017).

Neutron	Proton, Pion (other hadrons)	Nucleus	Muon	e⁻ / e⁺	Photon

1 TeV   1 TeV/u   1 TeV

High

Intra-nuclear cascade (JAM) + Evaporation (GEM) 3.0 GeV | JAMQMD + GEM | Virtual Photo-Nuclear JAM/JQMD + GEM 200 MeV

Photo-Nuclear JAM/JQMD + GEM + JENDL + NRF

Energy ↑ ↓

Intra-nuclear cascade (INCL4.6) + Evaporation (GEM) 200 MeV | d t ^{3}He α | Quantum Molecular Dynamics (JQMD) + GEM 10 MeV/u | EGS5 | EPDL97 or EGS5

20 MeV   JENDL-4.0/He   1 MeV

ATIMA + Original

Low

Nuclear Data Library (JENDL-4.0) | Stopping power (ATIMA) 1 keV   or track structure (KURBUC) | 1 keV | 1 keV

+ EGM 0.01 meV

Muonic atom + Capture | **Track structure 1 meV | *Only in water

Figure 2.11. The PHITS3.27 default setting of physics models. Image reprinted from PHITS development team (2022).

Chapter 3: Methodology

Exploring the health effects of space radiation exposure presents a formidable challenge due to the absence of a comparable radiation environment on Earth, both in natural settings and controlled laboratories. The omnidirectional nature of space radiation, encompassing a diverse array of fluxional particles with a broad energy spectrum, makes it practically unfeasible to replicate in current research facilities. The comprehension of the repercussions of space radiation exposure heavily relies on data extrapolated from sources such as Japanese atomic bomb survivors, victims of radiation accidents, and radiation therapy patients (NCRP, 2000; NCRP, 2006; NRC, 2006; ICRP, 2007). However, none of these exposure scenarios precisely mirror the conditions of SPE and GCR exposures in interplanetary space or on the surface of celestial bodies.

To study potential space radiation health risks, this project leverages the PHITS Monte Carlo simulation toolkit and the NASA Space Cancer Risk (NSCR) model, as well as the ICRP publications. The PHITS codes employed in this research are specifically designed to compute absorbed doses and particle fluxes within human organs, considering various thicknesses of aluminum shielding. This analysis extends to scenarios occurring in interplanetary space and on the Martian surface during exposure to the most intense GCR spectra during the solar minimum, as well as two significant historical SPEs in August 1972 and September 1989.

All simulations are conducted utilizing the OpenMP parallel computing method on multiple nodes, featuring 16 Xeon E5 – 2640v3 Central Processing Unit (CPU) cores and 36 Gigabyte Random-Access Memory (RAM). The computational infrastructure utilized for this project is the Cherry Creek supercomputer at the University of Nevada, Las Vegas (UNLV) National Supercomputing Institute (NSI).

3.1: Simulation Setup

3.1.1: Space Radiation Models

The radiation environment experienced during space missions beyond LET varies depending on the solar activity (Wilson et al., 1995a; Wilson, 1997). The solar dipole moment undergoes cycles approximately every 20 to 24 years, which in turn influences solar activity cycles lasting 10 to 12 years. Solar activity tends to increase as the dipole moment declines, reaching maximum levels when the dipole switches hemispheres. GCR flux magnitude fluctuates throughout the solar cycle (Figures 3.1 and 3.2) (Badhwar & O'Neill, 1994; Cucinotta & Cacao, 2020b), with peak fluxes at the solar minimum when the Interplanetary Magnetic Field (IMF) is weakest, facilitating the entry of intergalactic charged particles into the solar system. Conversely, near maximum solar activity, GCR intensity decreases, but the likelihood of significant SPE rises substantially (Figure 3.2) (Kim et al., 2009a). To assess the biophysical effects of space radiation exposure in worst-case scenarios, this project considers GCR during the solar minimum, as well as two historical SPEs in August 1972 and September 1989.

The GCR spectra during the solar minimum are generated in PHITS codes based on the German Aerospace Center (DLR) model developed by Matthiä et al. (2013). This model is made to reduce the complexity of the earlier GCR model of the International Organization for Standardization (ISO, 2004) developed originally by Nymmik (Nymmik et al., 1992; Nymmik, Panasyuk, & Suslov, 1996), where the differential flux density of particle i. Φ_i, is expressed concerning particle rigidity, R [GV], at the time, t, using the following formula:

$$\Phi_i(R,t) = \frac{dN}{dAdt'd\Omega dR}(R,t) = \frac{C_i\beta^{\alpha_i}}{R^{\gamma_i}}\left[\frac{R}{R+R_0(R,t)}\right]^{\Delta_i(R,t)}. \tag{3.1}$$

Here, N is the number of particles per area A at time t' with solid angle Ω and rigidity R. In the right-hand side of the equation, β is the particle's relative speed to light, $\Delta_i(R,t)$ and $R_0(R,t)$ are for the GCR modulation, and other parameters are introduced in Table 3.1.

In the DLR GCR model, the modulations are replaced by the mean sunspot number or W-index, W:

$$R_0(R,t) = 0.37 + 3\times10^{-4}[W(t,\Delta t(R,t))]^{1.45}, \tag{3.2a}$$

$$\Delta_i(R,t) = 0.02W(t) + 4.7, \tag{3.2b}$$

resulting in a simplified time-dependent function of $W(t)$:

$$\Phi_i(R,t) = \frac{C_i\beta^{\alpha_i}}{R^{\gamma_i}}\left[\frac{R}{R+(0.37+3\times10^{-4}W(t)^{1.45})}\right]^{0.02W(t)+4.7}. \tag{3.3}$$
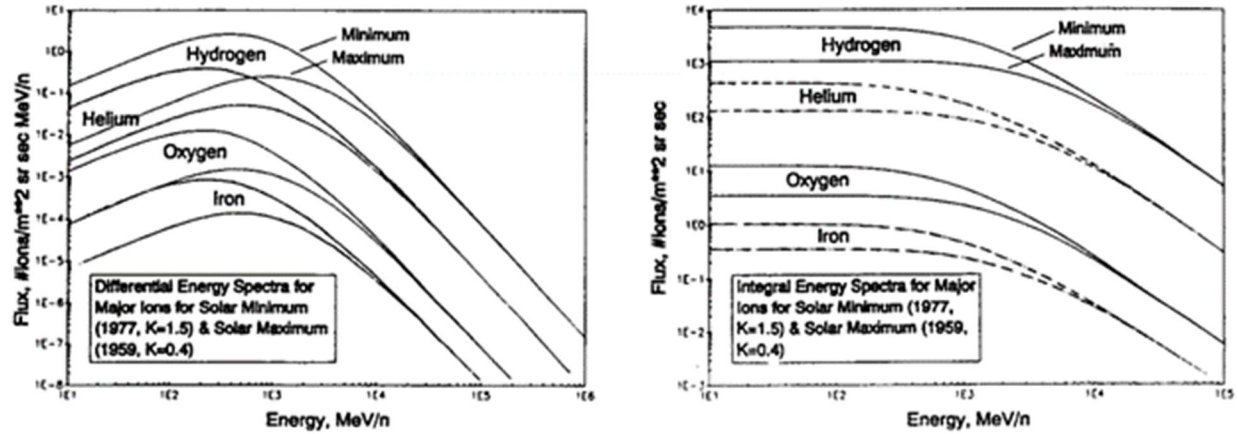
Figure 3.1. Spectra for GCR obtained from Pioneer 10, Voyager 1, and Voyager 2. The left and right panels show differential and integral energy spectra, respectively. Image reprinted from Badhwar & O'Neill (1994).
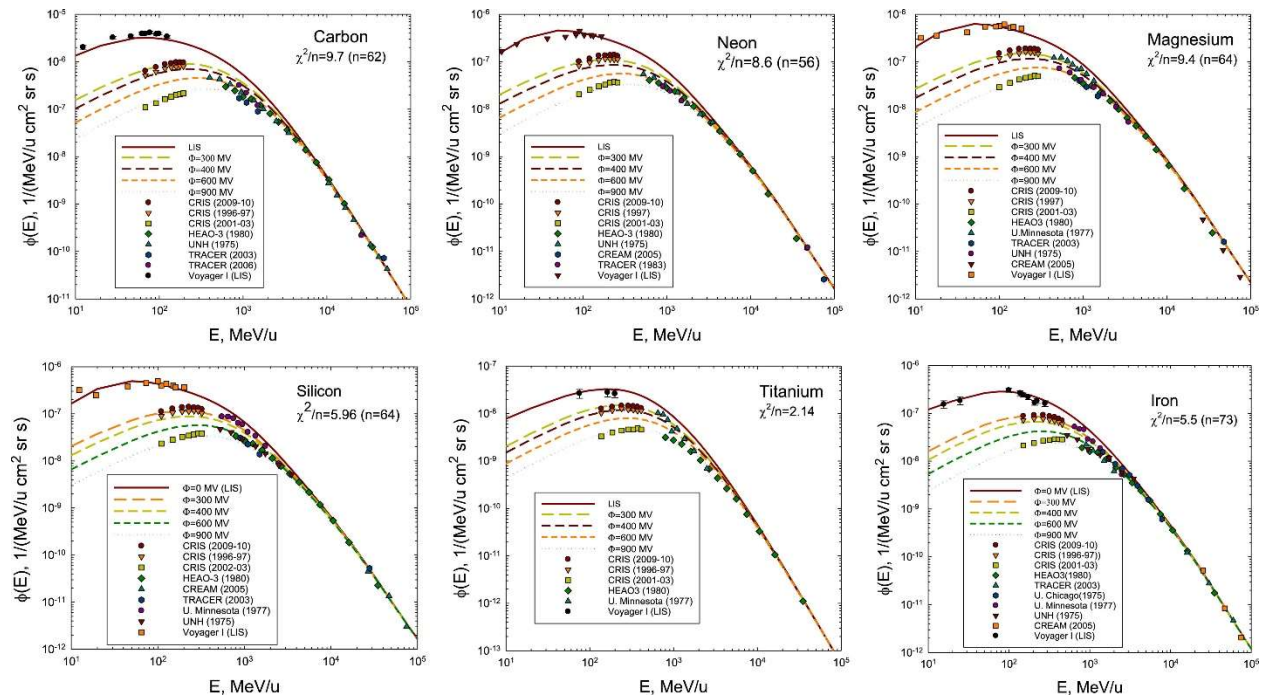
Figure 3.2. Selected GCR heavy ion spectra with solar modulation. Several measurements are shown, including the Voyager I measurement of the Local Interstellar Spectra (LIS), where solar modulation is ignorable. the Image reprinted from Cucinotta & Cacao (2020b).

55
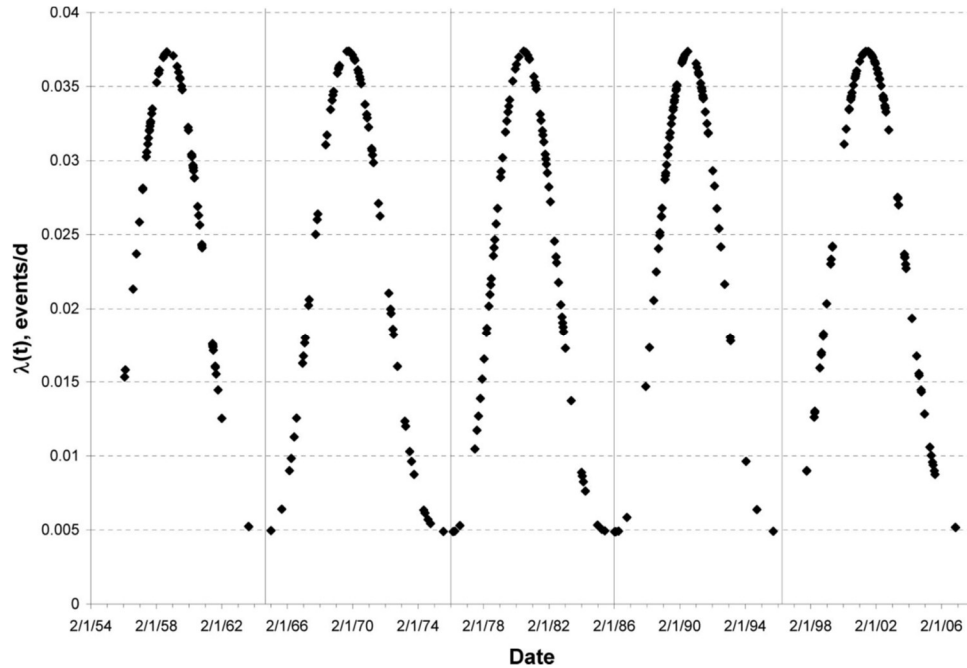
Figure 3.3. The propensity for SPE occurrence (hazard function, λ, at the time, t) in solar cycles 19 – 23. More SPEs near the solar maximum (the middle of cycles) are shown compared to the solar minimum (the beginning and end of cycles). Image reprinted from Kim et al. (2009a).

The W-index is derived from the GCR carbon data obtained by the Cosmic Ray Isotope Spectrometer (CRIS) aboard the Advanced Composition Explorer (ACE) spacecraft (Stone et al., 1998). The W-index ranges from approximately 0 during the solar minimum to 150 during the solar maximum. As of February 17, 2024, during the rise of solar activity in solar cycle 25, the W-index is 98.2, compared to 3.2 on March 26, 2020, near the solar minimum (NICT, 2024).

Due to the predominance of Z=1 and Z=2 ions in GCR spectra, an insufficient number of Z>2 ions is generated in the simulations if all GCR particles are considered in one single code. Hence, the initial GCR spectra have been generated in six separate PHITS codes for Z=1 ions, Z=2 ions, Z=3-8 ions, Z=9-14 ions, Z=15-20 ions, and Z=21-28 ions to ensure the statistical stability of all kinds of GCR particles.

Table 3.1. Parameters for the differential flux density in the DLR GCR model. Table reprinted from Matthiä et al. (2013).

Nucleus	Z_i	A_i	C_i [(s sr m² GV)⁻¹]	γ_i	α_i
H	1	1.0	18500.00	2.74	2.85
He	2	4.0	3690.00	2.77	3.12
Li	3	6.9	19.50	2.82	3.41
Be	4	9.0	17.70	3.05	4.30
B	5	10.8	49.20	2.96	3.93
C	6	12.0	103.00	2.76	3.18
N	7	14.0	36.70	2.89	3.77
O	8	16.0	87.40	2.70	3.11
F	9	19.0	3.19	2.82	4.05
Ne	10	20.2	16.40	2.76	3.11
Na	11	23.0	4.43	2.84	3.14
Mg	12	24.3	19.30	2.70	3.65
Al	13	27.0	4.17	2.77	3.46
Si	14	28.1	13.40	2.66	3.00
P	15	31.0	1.15	2.89	4.04
S	16	32.1	3.06	2.71	3.30
Cl	17	35.4	1.30	3.00	4.40
Ar	18	39.9	2.33	2.93	4.33
K	19	39.1	1.87	3.05	4.49
Ca	20	40.1	2.17	2.77	2.93
Sc	21	44.9	0.74	2.97	3.78
Ti	22	47.9	2.63	2.99	3.79
V	23	50.9	1.23	2.94	3.50
Cr	24	52.0	2.12	2.89	3.28
Mn	25	54.9	1.14	2.74	3.29
Fe	26	55.8	9.32	2.63	3.01
Co	27	58.9	0.10	2.63	4.25
Ni	28	58.7	0.48	2.63	3.52

On the other hand, SPE spectra are generated in PHITS simulations based on the Tylka model

(Tylka & Dietrich, 2009). The Tylka model expresses integral omnidirectional proton fluence, J

[protons/cm^2], using the Band function (Band et al., 1993; Tylka & Dietrich, 2009; Tylka, Dietrich,

& Atwell, 2010; Usoskin et al., 2011; Adriani et al., 2014; Bruno et al., 2018):

$$J(>R) = \begin{cases} J_0 R^{-\gamma_1} e^{-R/R_0}, & R \le (\gamma_2 - \gamma_1) R_0 \\ J_0 A R^{-\gamma_2}, & R > (\gamma_2 - \gamma_1) R_0 \end{cases} \tag{3.4}$$

where rigidity, R [GV], is given by:

$$R = \sqrt{T^2 + 2T_0 T}, \tag{3.5}$$

T is proton energy in the unit of [GeV], $T_0 = 0.938$ GeV is the proton rest-mass energy, A is given

by:

$$A = [(\gamma_2 - \gamma_1) R_0]^{(\gamma_2 - \gamma_1)} e^{(\gamma_2 - \gamma_1)}, \tag{3.6}$$

and parameters, J_0, R_0, γ_1, and γ_2 are determined by the measurements of SPEs. The comparison

between the Band function and measured SPE spectra is shown in Figure 3.4 (Tylka & Dietrich,

2009). Parameters for two historical SPEs are listed in Table 3.2 (Tylka & Dietrich, 2009; Tylka,

Dietrich, & Atwell, 2010). Initial GCR and SPE spectra generated in this project are displayed in

Figure 3.5.
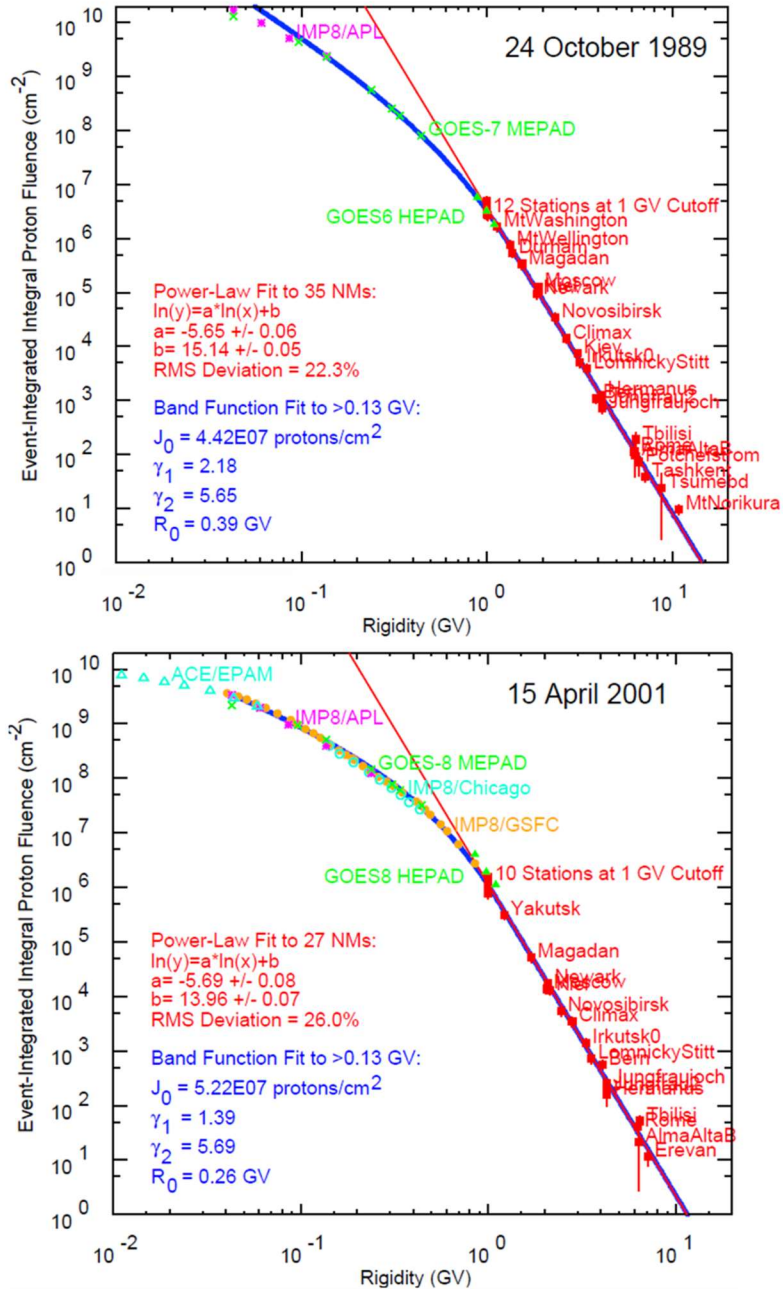
Figure 3.4. Comparisons of proton spectra between the Band function and Ground-Level Enhanced (GLE) measurements. Image reprinted from Tylka & Dietrich (2009).

Table 3.2. Band function parameters for selected SPEs in this project. Data obtained from Tylka & Dietrich (2009) and Tylka, Dietrich, & Atwell (2010).

Event		J_0 [protons/cm^2]	γ_1	γ_2	R_0 [GV]
August 4, 1972		1.450×10^{15}	-3.636	7.95	0.0345
September 29, 1989	(first 75 minutes)	1.799×10^{5}	2.060	2.63	3.6593
	(next 61 hours)	2.027×10^{10}	-0.109	4.58	0.0945
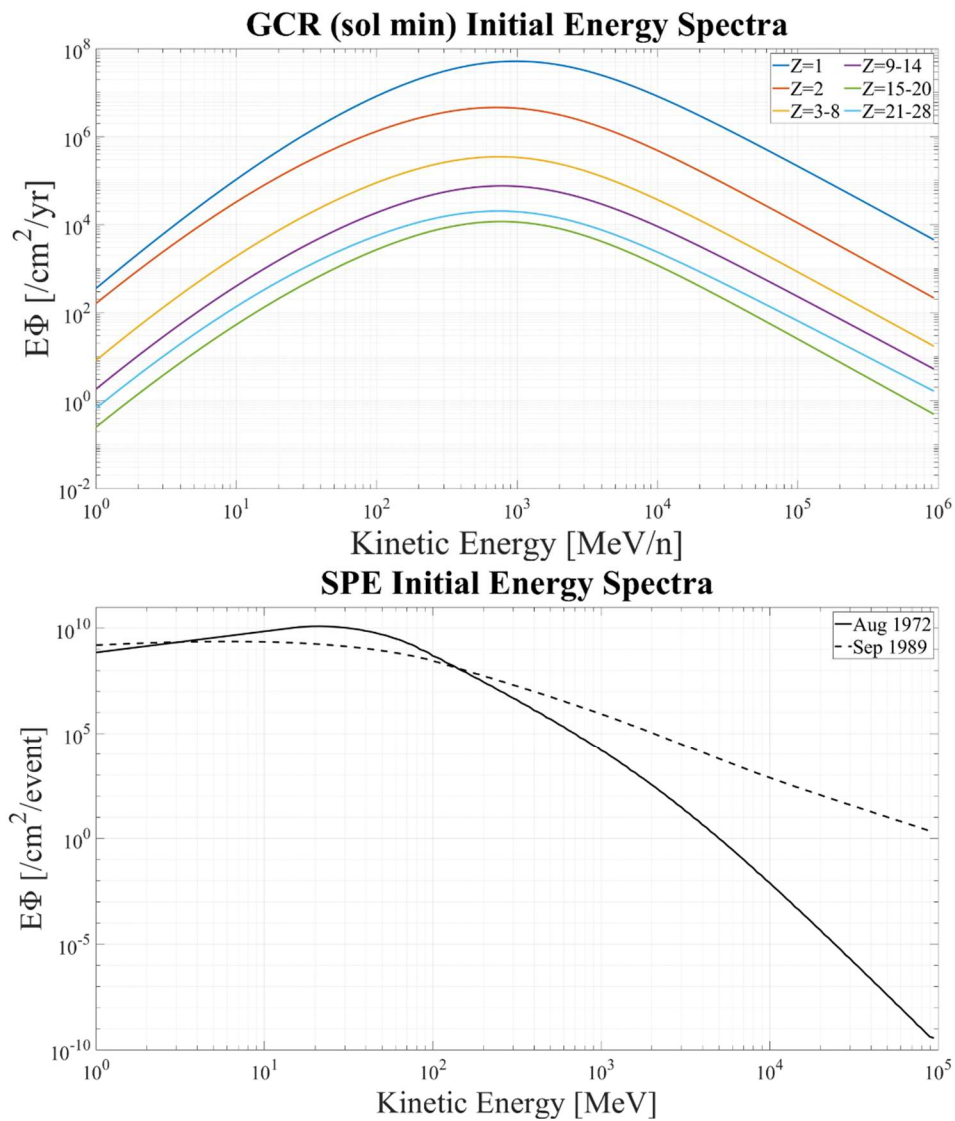
Figure 3.5. Particle energy (lethargy) spectra generated in simulations for GCR near the solar minimum and two large SPEs on August 4, 1972, and September 29, 1989.

3.1.2: Mars Environment

Mars, a terrestrial planet with a pale atmosphere and a mineral-based solid surface, exhibits distinctive characteristics compared to Earth. It possesses 10.7% of Earth's mass, 15.1% of Earth's volume, and 38% of Earth's surface gravity (NASA, 2023). The surface temperature on Mars, measured by Viking spacecraft (Kieffer, 1976), ranges from 183 K to 268 K (-90°C to -5°C or -130°F to 23°F). Travel time from Earth to Mars, contingent on trajectory, typically spans seven to eight months one way, given the current propulsion technology (Landau & Longuski, 2006; Mattfeld et al., 2014). Human missions to Mars are deemed feasible and economically viable in the coming decades, especially when contrasted with other celestial bodies such as Mercury with its extreme surface temperature range, Venus with its hot and dense atmosphere, and the moons of Jupiter and Saturn, which are too far away (Von Braun, 1953; Hoffman, 1997; Lambright, 2014; Musk, 2017).

Mars has an atmosphere thinner than that of Earth, with surface air pressure ranging from 4 to 9 millibars, influenced by factors like time, location, and season (Lewis et al., 1999; Noguchi et al., 2014), while the typical air pressure at sea level on Earth is 1013.25 millibars. This project assumes the Martian atmosphere comprises 95.7% carbon dioxide (CO_2), 2.7% nitrogen (N), and 1.6% argon (Ar) (Noguchi et al., 2014; Hintze, Meier, & Shah, 2018) with a height of 11.1 km and a density of 0.0002 g/cm^3, resulting in a thickness of 22.2 g/cm^2 (NASA, 2023). Notably, the Martian air appears denser near the surface when observed from the surface, as particles approaching from the side need to traverse more air compared to those coming from above. The simulations in this work generate space radiation above the hemispherical atmosphere; hence, the Martian air density increases with the zenith angle to demonstrate different amounts of atmosphere. The depth of atmosphere, denoted as l, along the zenith angle, θ, is defined by:

$$l = \sqrt{x^2 + z^2}, \tag{3.7}$$

where

$$z = h_0 \cos\theta, \tag{3.8}$$

$$x = \sqrt{(r_M + h_0)^2 - (r_M + z)^2}. \tag{3.9}$$

In these equations, θ ranges from 0 to 90°, $r_M = 3389.5$ km is the radius of Mars, $h_0 = 11.1$ km is the height of the atmosphere at $\theta = 0°$, and $\rho_0 = 0.0002$ g/cm^3 is the density of the atmosphere at $\theta = 0°$. Subsequently, the air density ρ as a function of the zenith angle θ for the hemispherical atmosphere is given by:

$$\rho = \rho_0 \frac{1}{h_0} = \rho_0 \left(1 + \frac{4r_M}{h_0} \sin^2\frac{\theta}{2}\right)^{0.5}. \tag{3.10}$$

The physical characteristics of Martian regolith vary with location and differ from sample to sample according to the landing site of the spacecraft. In this project, the regolith has a density of 1.7 g/cm^3, and the chemical composition consists of 46.83% oxygen (O), 23.89% silicon (Si), 7.07% potassium (K), 6.51% iron (Fe), 4.90% aluminum (Al), 4.17% sodium (Na), 3.63% calcium (Ca), 2.18% magnesium (Mg), and 0.82% hydrogen (H), as determined by soil modeling in the On-Line

Tool for the Assessment of Radiation in Space (OLTARIS) (Slaba et al., 2011; Matthiä et al., 2016;

Al Zaman & Kunja, 2023).

3.1.3: Human Phantom

Monte Carlo simulations, vital for comprehending the biological impacts of radiation, necessitate a computational biological target or phantom. A small phantom with simple elemental components, such as a water sphere, has the advantages of fast computation speed and ease of performing (Papadimitroulas et al., 2012; Bermal et al., 2015; Pak & Cucinotta, 2021). It may provide reliable data, including the particle flux and energy deposition in a biological target, since most of the living creatures of interest in radiation science are primarily composed of water. However, their simplicity limits their ability to provide intricate information regarding realistic dose distribution in critical human organs and the potential biomedical risks of radiation exposure.

In contrast, a detailed human phantom becomes instrumental in addressing the complexities of radiation protection studies. One such anthropomorphic mathematical phantom utilized in Monte Carlo simulations (Sato et al., 2003) is the Medical Internal Radiation Dose (MIRD) phantom (Snyder et al., 1969; ICRP, 1975; Snyder et al., 1978; ICRP, 2002) originating in the 1960s. Initially comprising 22 critical human organs for a standard adult, the MIRD phantom evolved in the 1980s to encompass a "family" of phantom series catering to different ages and sexes (Cristy, 1980; Kramer et al., 1982; Cristy & Eckerman, 1987).

Another detailed human anatomy phantom is the Computerized Anatomical Man (CAM) model, developed in the early 1970s with NASA's funding (Kase, 1970; Billings & Yucker, 1973). Subsequently, the female version (Computerized Anatomical Female; CAF) emerged in the early 1990s (Yucker & Huston, 1990; Yucker & Reck, 1992). CAM and CAF have been extensively employed in radiation-induced cancer risk studies for space exploration (Kim et al., 2006; Kim et al., 2009a; Slaba et al., 2010; Cucinotta et al., 2011b) with several programs, including the Baryon Transport Computer Code (BRYNTRN) (Wilson et al., 1988; Cucinotta et al., 1994c) and the high-

charge-and-energy (HZE) Transport Computer Program (HZETRN) (Wilson et al., 1991; Wilson et al., 1995c).

With advancements in tomography and imaging technologies, volumetric pixel (voxel) phantoms with more realistic human anatomy have been developed based on computed tomography (CT) or magnetic resonance imaging (MRI) data. Notable examples include the Male Adult voXel (MAX) and Female Adult voXel (FAX) phantoms (Kramer et al., 2003; Kramer et al., 2004), featuring different elemental compositions of hydrogen (H), carbon (C), nitrogen (N), oxygen (O), sodium (Na), magnesium (Mg), phosphorus (P), sulfur (S), chlorine (Cl), potassium (K), calcium (Ca), iron (Fe), and iodine (I) for soft tissue, adipose, lung, muscle, skin, cartilage, bone, and red bone marrow, and yellow bone marrow based on ICRU Report 44 (ICRU, 1989), while water-equivalent CAM and CAF models are made of hydrogen (H) and oxygen (O) for all tissues and bones. In Figure 3.6, MAX and FAX phantoms are depicted with MIRD phantoms.

The human phantom utilized in this project is the three-dimensional reference male voxel phantom released in 2009 jointly by the International Commission on Radiological Protection (ICRP) and the International Commission on Radiation Units and Measurements (ICRU) in ICRP Publication 110 (ICRP, 2009). Representing a 38-year-old adult male with a height of 176 cm and a weight of 73.146 kg, this phantom was developed using 220 image slices from 122 individuals, containing data for 141 segmented tissue types and 53 material specifications. Details on the organs and materials are listed in ICRP Publication 110 (ICRP, 2009).
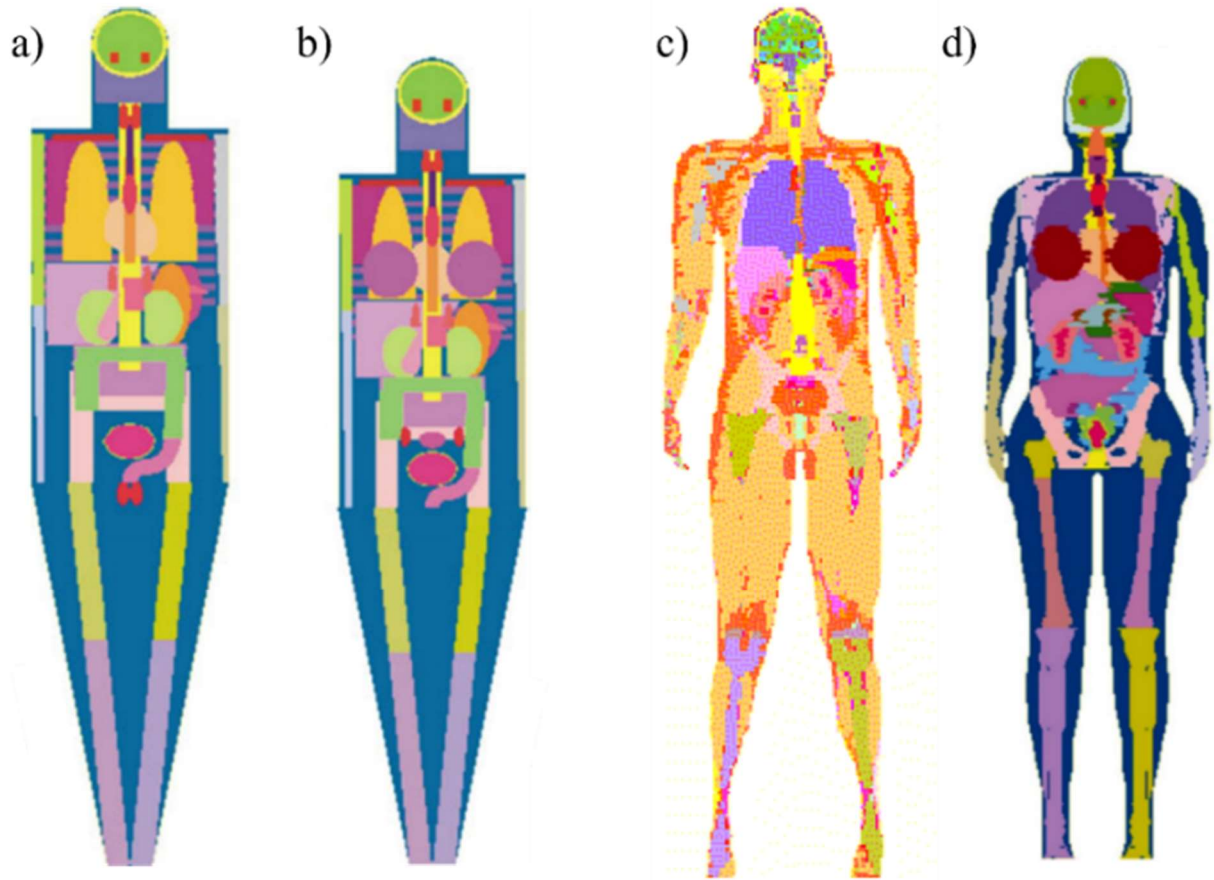
Figure 3.6. Mathematical and voxel human phantoms. a) male adult mathematical MIRD phantom, b) female adult mathematical MIRD phantom, c) male adult voxel phantom (MAX), and d) female adult voxel phantom (FAX). Image reprinted from Kramer et al. (2003) and Kramer et al. (2004).

In this study, the human phantom assumes a standing position inside the spacecraft or habitat. PHITS simulation codes compute the particle fluxes and absorbed doses in each of the 141 tissue types during exposure to GCRs and SPEs in interplanetary space and on the Martian surface behind various shielding levels. Simulation results are then averaged into 15 organs of interest, aligning with epidemiological studies on low LET radiation (NCRP, 2006). These organs include the bladder, bone marrow, brain, breast, colon, esophagus, gonads, liver, lungs, prostate, remainder, salivary glands, skin, stomach, and thyroid. The "remainder" encompasses adrenal glands, gall

bladder, heart, kidneys, lymphatic nodes, muscles, nasal passage, oral mucosa, pancreas, small

intestine, spleen, and thymus (ICRP, 2007). For organs with multiple segments, the flux (F) is

calculated using:

$$F = \frac{\sum_i F_i m_i}{\sum_i m_i},$$
(3.11)

where F_i and m_i represent the particle flux in the i-th segment and the mass of the i-th segment,

respectively.

3.1.4: Physics Models

As discussed in Chapter 2.2.4, PHITS provides an array of physics models tailored for diverse particle types, energy ranges, and scientific objectives. The default physics model for nucleus interaction within PHITS is the original iteration of JQMD. Developed to overcome the constraint of prior hadronic collision models, which often suffered from an excessive number of parameters and limitations in energy or phenomenon coverage (Niita et al., 1995), JQMD is rooted in the Quantum Molecular Dynamics (QMD) and statistical decay model (SDM).

In JQMD, the nucleon state is described by a Gaussian wave function:

$$\phi_i(\mathbf{r}) = \frac{1}{(2\pi L)^{3/4}} \exp\left[-\frac{(\mathbf{r} - \mathbf{R}_i)^2}{4L} + \frac{i}{\hbar}\mathbf{r} \cdot \mathbf{P}_i \right]. \tag{3.12}$$

Here, L is the width, $\mathbf{R}_i$ is the center of position, and $\mathbf{P}_i$ is the center of momentum of the i-th nucleon. The spatial coordinate of the centroid $\mathbf{r_i}$ and the momentum $\mathbf{p_i}$ of the i-th nucleon are given by:

$$\dot{\mathbf{r}}_i = \frac{\mathbf{p_i}}{m} + \frac{\partial \langle \hat{V} \rangle}{\partial \mathbf{p_i}}, \tag{3.13a}$$

$$\dot{\mathbf{p}}_i = -\frac{\partial \langle \hat{V} \rangle}{\partial \mathbf{r_i}}, \tag{3.13b}$$

Here, m is the nucleon rest mass, N is the number of particles, and the potential V of the i-th particle is the sum of Skyrme force, Coulomb interaction, and symmetry terms. In this model, baryon-baryon elastic cross-sections (σ [mb]) are energy-dependent:

$$\sigma = \begin{cases} \dfrac{C_1}{1+100\sqrt{s'}} + C_2, & E \leq 1\,\text{GeV} \\[2ex] C_3\left[1 - \dfrac{2}{\pi}\tan^{-1}(1.5\sqrt{s'} - 0.8)\right] + C_4, & E > 1\,\text{GeV} \end{cases} \tag{3.14}$$

Here, $\sqrt{s'} = 0.4286$ GeV and the parameters are detailed in Table 3.3.

Table 3.3. Parameters for elastic cross-sections in the JQMD model. Table reprinted from Niita et al. (1995).

	p-n	Others
C_1 [mb]	28.0	35.0
C_2 [mb]	27.0	20.0
C_3 [mb]	12.34	9.65
C_4 [mb]	10.0	7.0

On the other hand, the inelastic cross-section is parametrized by VerWest & Arndt (1982):

$$\sigma(s) = \frac{\pi(\hbar c)^2}{2p^2} \alpha \left(\frac{p_r}{p_0}\right)^\beta \frac{m_0^2 \Gamma^2 (q/q_0)^3}{(s^* - m_0^2)^2 + m_0^2 \Gamma^2}, \tag{3.15}$$

where

$$p_0^2 = \frac{1}{4} s_0 - m_N^2, \tag{3.16a}$$

$$s_0 = (m_N + m_0)^2, \tag{3.16b}$$

$$p_r^2(s) = \frac{\left[s - \left(m_N - \langle M \rangle\right)^2\right]\left[s - \left(m_N + \langle M \rangle\right)^2\right]}{4s}, \tag{3.16c}$$

$$q^2(s^*) = \frac{\left[s^* - \left(m_N - m_\pi\right)^2\right]\left[s - \left(m_N + m_\pi\right)^2\right]}{4s^*}, \tag{3.16c}$$

$$s^* = \langle M \rangle^2, \tag{3.16d}$$

$$q_0 = q(m_0^2). \tag{3.16e}$$

70

Table 3.4. Parameters for the Briet-Wigner distribution. Values obtained from VerWest & Arndt (1982).

	Δ	N^*
M_0 [MeV]	1220	1430
Γ_0 [MeV]	120	200

The mean mass of the resonance, denoted as $\langle M \rangle$, is used in this formula, with M_0 and Γ_0 presented in Table 3.4.

Following the dynamic interaction of particles with QMD, the SDM engages in the statistical stage. The emission probability P_x of a light particle x is described by the Fermi gas model:

$$P_x = (2J_x + 1)m_x\epsilon\sigma_x(\epsilon)\rho(E)d\epsilon. \tag{3.17}$$

In this equation, J_x is the spin, m_x is the mass, ϵ is the kinetic energy of the particle, $\sigma_x(\epsilon)$ is the inverse cross-section, and $\rho(E)$ is the level density of the residual nucleus with the excitation energy E.

JQMD has undergone testing in the energy range of 100 MeV to 3 GeV and demonstrated good agreement with secondary neutron yield. However, certain assumptions underlie the nucleon-nucleon interaction in this model, leading to underestimated production cross-sections for projectile-like fragments. Consequently, JQMD-2.0, the advanced version, was introduced. Noteworthy improvements include enhanced fragment production in nucleus-nucleus reactions and the adoption of a Lorentz-covariant equation of motion for nucleon-nucleon collisions (Ogawa

et al., 2015a; Ogawa et al., 2015b; Ogawa et al., 2016). The Lorentz-covariant formulation is expressed as:

$$\dot{\mathbf{r}}_{\mathbf{i}} = \frac{\mathbf{p}_{\mathbf{i}}}{2p_i^0} + \sum_{j}^{N} \frac{m}{p_j^0} \frac{\partial \langle \hat{V}_j \rangle}{\partial \mathbf{p}_{\mathbf{i}}}, \tag{3.18a}$$

$$\dot{\mathbf{p}}_{\mathbf{i}} = -\sum_{j}^{N} \frac{m}{p_j^0} \frac{\partial \langle \hat{V}_j \rangle}{\partial \mathbf{r}_{\mathbf{i}}}, \tag{3.18b}$$

$$p_j^0 = \sqrt{\mathbf{p}_{\mathbf{i}}^2 + m^2 + 2m \langle \hat{V}_j \rangle}. \tag{3.18c}$$

In contrast to the earlier JQMD version, JQMD-2.0 has exhibited improved agreement with experimental data regarding heavy fragment and secondary neutron production cross-sections, albeit with increased computation time. Given the pivotal role of accurate high-energy ion transport in space radiation studies, JQMD-2.0 has been specifically chosen for nucleus-nucleus reactions in this project.

For other interactions, the recommended physics models and data libraries depicted in Figure 2.9 have been adopted. An additional option of EGM has been incorporated to compute the radiation environment inside spacecraft and space habitats, ensuring precise secondary neutron, photon, and electron generation in the shielding material. However, for the computation of tissue-specific absorbed dose and particle fluxes in the human phantom, EGM and EGS5 have not been applied to optimize computational speed and enhance statistical stability.

3.2: Dosimetric Quantity Assessment

As discussed in Chapter 2.1.4, exposure to space radiation and secondary particles induces various biomedical consequences. The fundamental quantity to assess radiation effects is absorbed dose, denoted as D [Gy], which is expressed as:

$$D = \frac{d\bar{\varepsilon}}{dm}.$$ (3.19)

Here, $d\bar{\varepsilon}$ [J] represents the mean energy deposited in a matter of mass dm [kg]. The relationship between absorbed dose (D [Gy]) and fluence (F [1/cm^2]) is established as (Cucinotta, Kim, & Chappell, 2011b):

$$D = \frac{FL}{6.24}.$$ (3.20)

In this equation, the fluence (F) represents the number of particles per unit area, and L [keV/μm] denotes LET, as defined in Chapter 2.1.1.

The biological effects of radiation extend beyond the mere absorbed dose quantity, influenced by factors such as particle type, particle energy, exposure duration, and organ or tissue type (ICRP, 1991; Durante & Cucinotta, 2008; Cucinotta & Durante, 2009; Cucinotta, Kim, & Chappell, 2011b). For radiological protection purposes, ICRP Publications 26 and 60 (ICRP, 1977; ICRP, 1991) introduced two quantities: dose equivalent (H [Sv]) and effective dose (E [Sv]).

The dose equivalent (H [Sv]) is expressed as the product of the absorbed dose (D [Gy]) and the radiation quality factor (QF), representing the biological effectiveness of the radiation:

$$H = D \cdot QF. \tag{3.21}$$

For terrestrial radiation sources, ICRP Publication 60 (ICRP, 1991) suggests that QF depends on LET (L [keV/μm]):

$$QF(L) = \begin{cases} 1, & L < 10\,\mathrm{keV}/\mu m \\ 0.32L - 2.2, & 10\,\mathrm{keV}/\mu m \le L \le 100\,\mathrm{keV}/\mu m \\ 300/\sqrt{L}, & L > 100\,\mathrm{keV}/\mu m \end{cases} \tag{3.22}$$

In the NASA Space Cancer Risk (NSCR) model, the space radiation quality factor is defined differently, considering details of a particle's microscopic energy deposition or track structure (Cucinotta, Kim, & Chappell, 2012; Cucinotta, Kim, & Chappell, 2013a; Cucinotta, To, & Cacao, 2017; Cucinotta et al., 2020a; Cucinotta & Saganti, 2022a; Cucinotta, 2022b):

$$QF(Z,E) = Q_L(Z,E) + Q_H(Z,E). \tag{3.23}$$

Here, low ionization density track contribution (Q_L) and high ionization density track contribution (Q_H) are defined by:

$$Q_L(Z,E) = [1 - P(Z,E)], \tag{3.24a}$$

$$Q_H(Z, E) = 6.24 \Sigma_0 P(Z, E) / (\alpha_\gamma L), \qquad (3.24b)$$

with the parametric function P defined as:

$$P(Z, E) = [1 - \exp(-Z^{*2} / \kappa\beta^2)]^m [1 - \exp(-E / 0.2)]. \qquad (3.25)$$

Here, E is the particle's kinetic energy in the unit of [MeV/u] for nuclei and [MeV] for other particles, L [keV/µm] is the particle's LET, Z is the particle's charge number, $Z^* = Z[1 - \exp(-125\beta / Z^{2/3})]$ is the particle's effective charge number, and β is the particle's relative speed to the light. The other parameters used in this calculation are listed in Table 3.5. The model accounts for secondary electrons with sufficient energy to cause additional ionizations nearby, called delta-rays, of which generation is proportional to Z^{*2}/β^2. The term $[1 - \exp(-E / 0.2)]$ is for "thindown" where the particle track width is smaller than the target at low energy, which has less impact on space radiation exposure since low energy-contribution is minimal for heavy ions. Additional considerations of non-targeted effects on the quality factor are described in recent publications (Cucinotta, 2024); however, they are not used in the present work. The LET values, ICRP quality factors, and NSCR quality factors for selected mesons and ions are presented in Figure 3.7.

On another note, ICRP Publication 110 (ICRP, 2007) defines quality factors for electrons, muons, and photons as 1. The neutron quality factor (QF_n) is presented as a continuous function of neutron energy (E_n [MeV]):

$$QF_n(E_n) = \begin{cases} 2.5 + 18.2e^{-[\ln(E_n)]^2/6}, & E_n < 1\,\text{MeV} \\ 5.0 + 17.0e^{-[\ln(2E_n)]^2/6}, & 1\,\text{MeV} < E_n < 50\,\text{MeV} \\ 2.5 + 3.25e^{-[\ln(0.04E_n)]^2/6}, & E_n > 50\,\text{MeV} \end{cases} \tag{3.26}$$

Effective dose (E [Sv]) is assessed by combining the dose equivalent (H_T) in organs or tissues (T) with tissue weighting factors (w_T):

$$E = \sum_T H_T w_T. \tag{3.27}$$

Tissue weighting factors express the susceptibility of different organs or tissues to radiation-induced risks. Table 3.6 provides a comparison of tissue weighting factors in ICRP Publication 103 (ICRP, 2007) and the NSCR model.

Table 3.5. Parameters in the NSCR model. Values obtained from Cucinotta, To, & Cacao (2017), Cucinotta (2024), and Pak & Cucinotta (2024).

Parameter	Low Z (Z ≤ 2)	High Z (Z > 2)
m	3 ± 0.5	3 ± 0.5
κ	624 ± 69	1000 ± 150
Σ_0/α_γ, μm^2 Gy	$(4728 \pm 1378)/6.24$ for solid cancer $(1750 \pm 250)/6.24$ for leukemia	$(4728 \pm 1378)/6.24$ for solid cancer $(1750 \pm 250)/6.24$ for leukemia
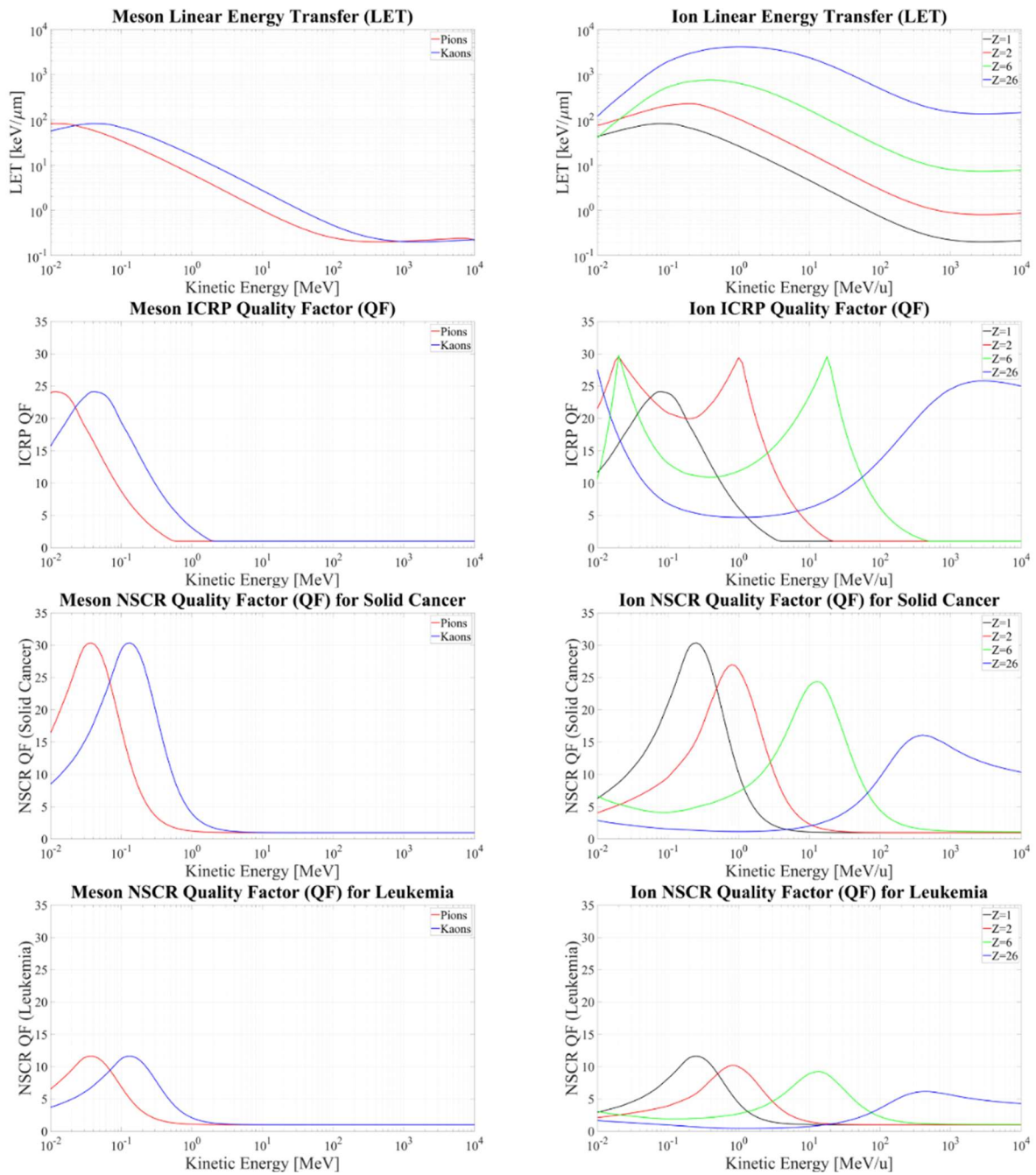
Figure 3.7. The LET values and quality factors for pions, kaons, Z=1 ions, Z=2 ions, Z=6 ions, and Z=26 ions.

Table 3.6. Tissue weighting factors for the effective dose evaluation. Values obtained from ICRP (2007) and Pak & Cucinotta (2024).

Organs	ICRP Publication 103	NSCR Model (Male)
Bladder	0.04	0.04
Bone Marrow	0.12	0.10
Bone Surface	0.01	0.00
Brain	0.01	0.03
Breast	0.12	0.00
Colon	0.12	0.20
Esophagus	0.04	0.02
Gonads	0.08	0.00
Liver	0.04	0.10
Lungs	0.12	0.22
Oral Cavity	0.00	0.02
Prostate	0.00	0.02
Remainder	0.12	0.10
Salivary Glands	0.01	0.02
Skin	0.01	0.01
Stomach	0.12	0.10
Thyroid	0.04	0.02
Sum	1.00	1.00

Chapter 4: Analysis

4.1: Radiation Environment in Interplanetary Space and on the Martian Surface

A comprehensive set of simulations has been undertaken to assess the radiation environment within spacecraft and space habitats under various thicknesses of aluminum shielding in interplanetary space and on the Martian surface. The primary focus is on understanding the mixed-field radiation composed of both primary radiation penetrating the shielding and secondary radiation resulting from interactions between the primary radiation and the shielding material. Utilizing a combination of JQMD-2.0, EGM, and EGS5, the accurate secondary radiation environment for Mars exploration has been evaluated. The human phantom is not reconstructed in this series of simulations to reduce the computation time and increase statistical stability.

For interplanetary space, simulations consider a hollow aluminum sphere spacecraft with a 5-meter inner diameter and shielding thicknesses ranging from 1 to 50 g/cm^2. The energy spectra of each particle are recorded at 1 micrometer behind the shielding. For the Martian surface, the space habitat is modeled as a hemispherical building with a 2.5-meter inner radius and shielding thicknesses ranging from 1 to 50 g/cm^2. Energy spectra of downward particles penetrating the Martian atmosphere and upward particles reflected from the ground are computed separately. The particle fluxes are recorded 1 micrometer behind the shielding for downward particles and 1 micrometer above the Martian surface for upward particles. To record the particle fluence in the PHITS simulation codes, the [T-Cross] tally has been used, and only the particles in the inward direction have been considered for both interplanetary space and the Martian surface.

The number of GCR particles generated in this project is 1×10^7, 4×10^6, 1×10^6, 5×10^5, 2.5×10^5, and 1×10^5 for Z=1, Z=2, Z=3-8, Z=9-14, Z=15-20, and Z=21-28 ions, respectively, for interplanetary space, and the computation time was around 7 to 10 days. For the Martian surface,

1×10^6, 5×10^5, 1×10^5, 6×10^4, 5×10^4, and 2×10^4 numbers of Z=1, Z=2, Z=3-8, Z=9-14, Z=15-20, and Z=21-28 ions were generated, respectively, and each simulation took around 4 to 6 days. On the other hand, SPE simulations used 1×10^{10} initial protons for both interplanetary space and the Martian surface, and around 3 to 4 days were taken.

Figure 4.1 illustrates the energy spectra of protons (^{1}H ions), deuterons (^{2}H ions), tritons (^{3}H ions), ^{3}He ions, ^{4}He ions, heavy ions, positive and negative pions (π^+ and π^-), positive and negative muons (μ^+ and μ^-), positive and negative kaons (K^+ and K^-), photons (γ), neutrons (n), and negative and positive electrons (e$^-$ and e$^+$) during one-year GCR exposure near the solar minimum behind different shielding aluminum in interplanetary space. It is anticipated in the figure that significant amounts of secondary radiation, especially pions, neutrons, photons, and electrons, are produced in interplanetary space. The sudden increase in the ^{2}H and ^{3}H fluxes at 3 GeV/u is due to the change of the physics model from JQMD-2.0 to JAMQMD. Figure 4.2 compares the particle fluxes behind thin (5 g/cm^2 Al) and typical (20 g/cm^2 Al) shielding, showing that while the shape of energy spectra remains similar, the number of short-range primary ions decreases along with shielding thickness, and generation of secondary particle, including mesons, leptons, photons, neutrons, and secondary Z=1 ions, increases.

Figure 4.1. Ion and non-ion energy (lethargy) spectra during annual exposure to GCR near the solar minimum behind 1, 2, 5, 10, 20, and 50 g/cm^2 aluminum shielding in interplanetary space.

Figure 4.2. Comparison of ion and non-ion energy (lethargy) spectra behind thin (5 g/cm^2 Al) and typical (20 g/cm^2 Al) shielding during annual exposure to GCR near the solar minimum in interplanetary space.

Figures 4.3 and 4.4 show downward and upward energy spectra inside the Martian habitat during one-year GCR exposure, respectively. The presence of the Martian atmosphere causes a shift in the peak of downward proton spectra from approximately 1 GeV to a few hundred MeV and a decrease in the flux around one order of magnitude compared to interplanetary space. It has been shown that GCR ions heavier than helium particles cannot penetrate the Martian atmosphere and are absorbed or attenuated before reaching the ground. It is also found that the upward or albedo particles reflected by or generated in the ground are nonnegligible. Notably, the upward neutron and photon fluxes are revealed to be similar levels of their downward flux for E < 10 MeV. In addition, electrical and other devices, as well as astronauts, inside the Martian habitat are expected to be continuously exposed to a number of protons coming from the Martian surface with around 100 MeV kinetic energy during GCR exposure. Compared to the interplanetary cruise phase, less exposure to the charged particles is anticipated, while exposure to the low-energy neutrons will be more severe since more secondary neutrons are generated in the atmosphere and the ground.

Figure 4.5 compares downward and upward ion and non-ion energy spectra behind thin (5 g/cm^2 Al) and typical (20 g/cm^2 Al) shielding on the Martian surface, indicating minimal variation with shielding, while the low-energy neutron flux is slightly increased with thicker shielding.
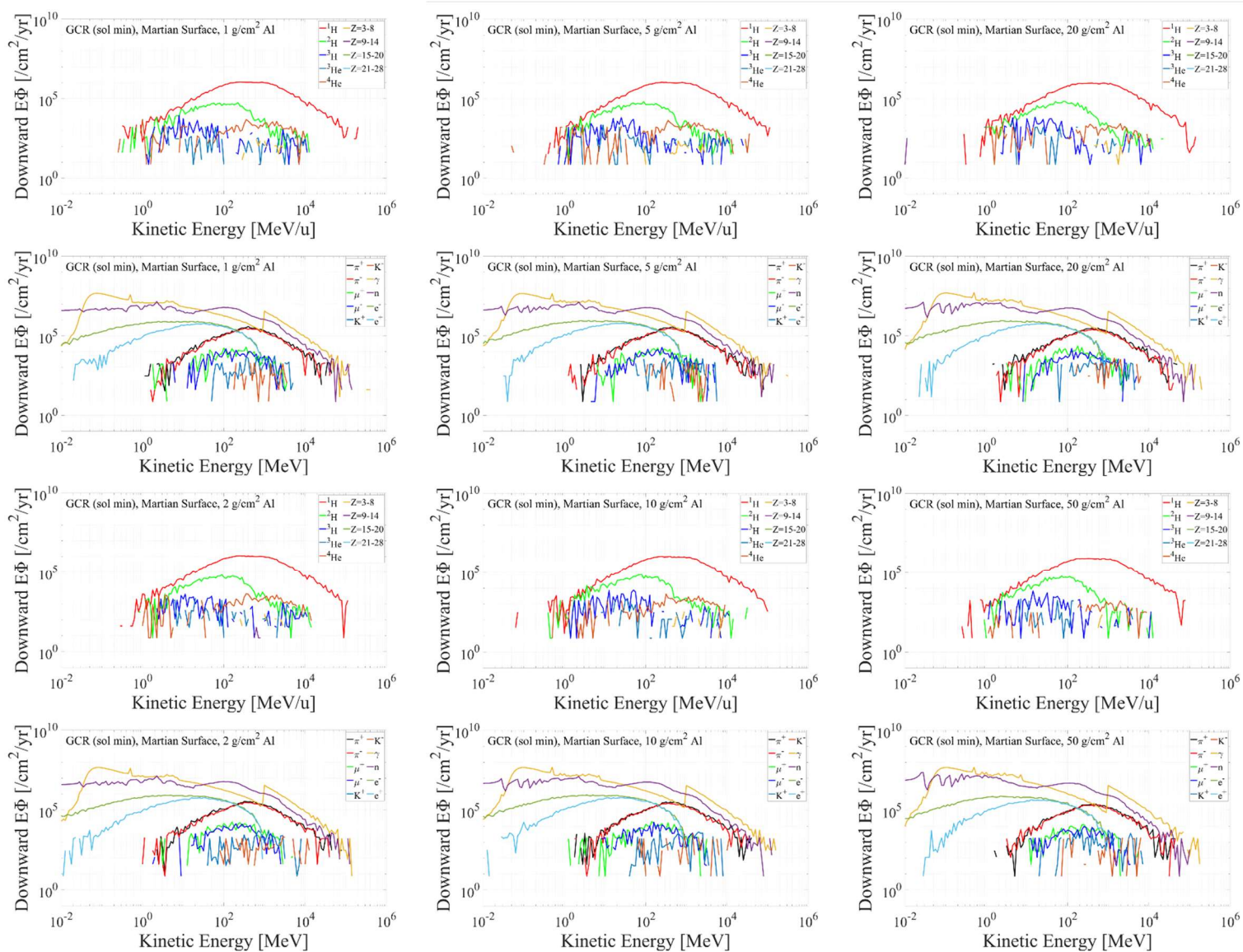
Figure 4.3. Downward ion and non-ion energy (lethargy) spectra during annual exposure to GCR near the solar minimum behind 1, 2, 5, 10, 20, and 50 g/cm² aluminum shielding on the Martian surface.
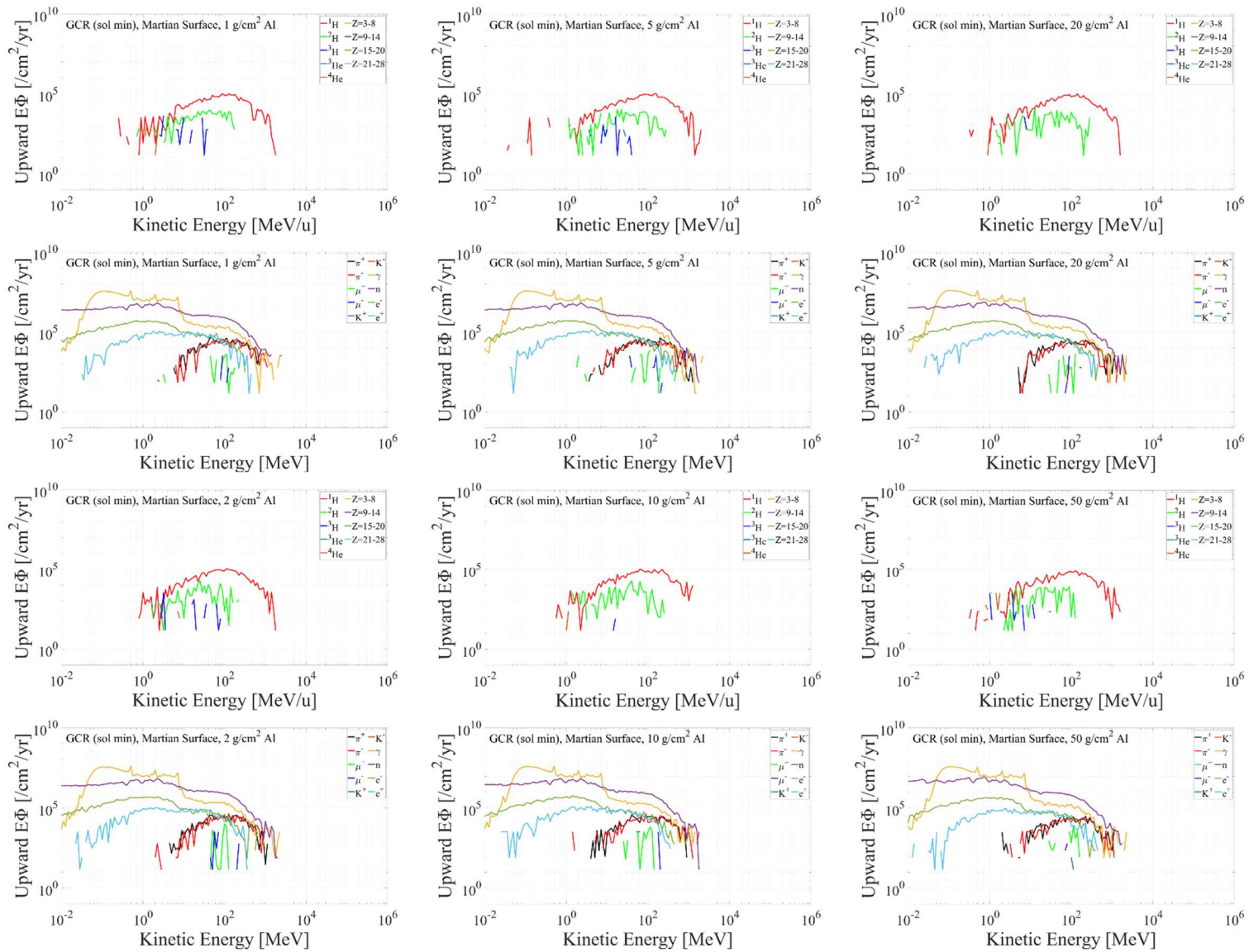
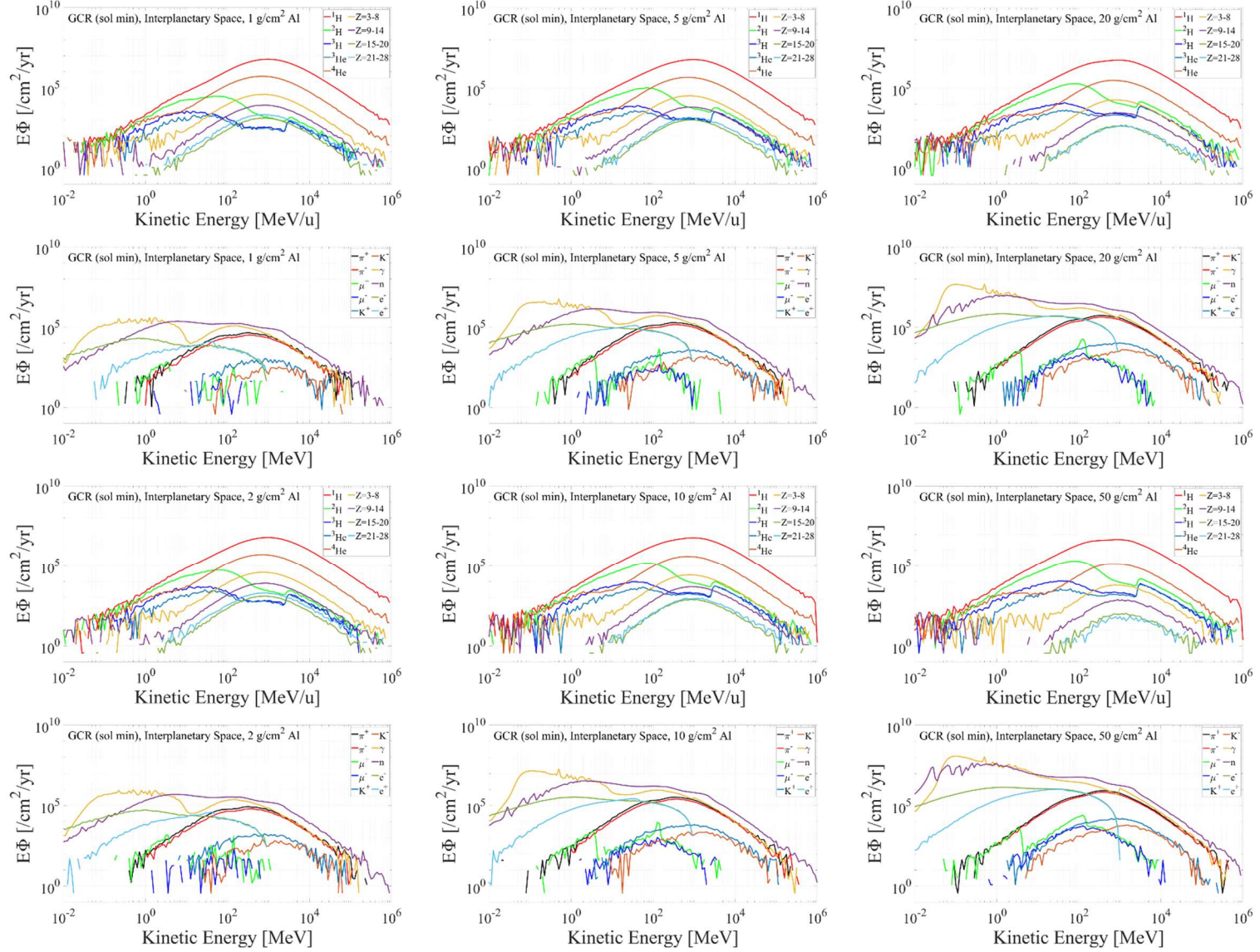Figure 4.4. Upward ion and non-ion energy (lethargy) spectra during annual exposure to GCR near the solar minimum behind 1, 2, 5, 10, 20, and 50 g/cm² aluminum shielding on the Martian surface.
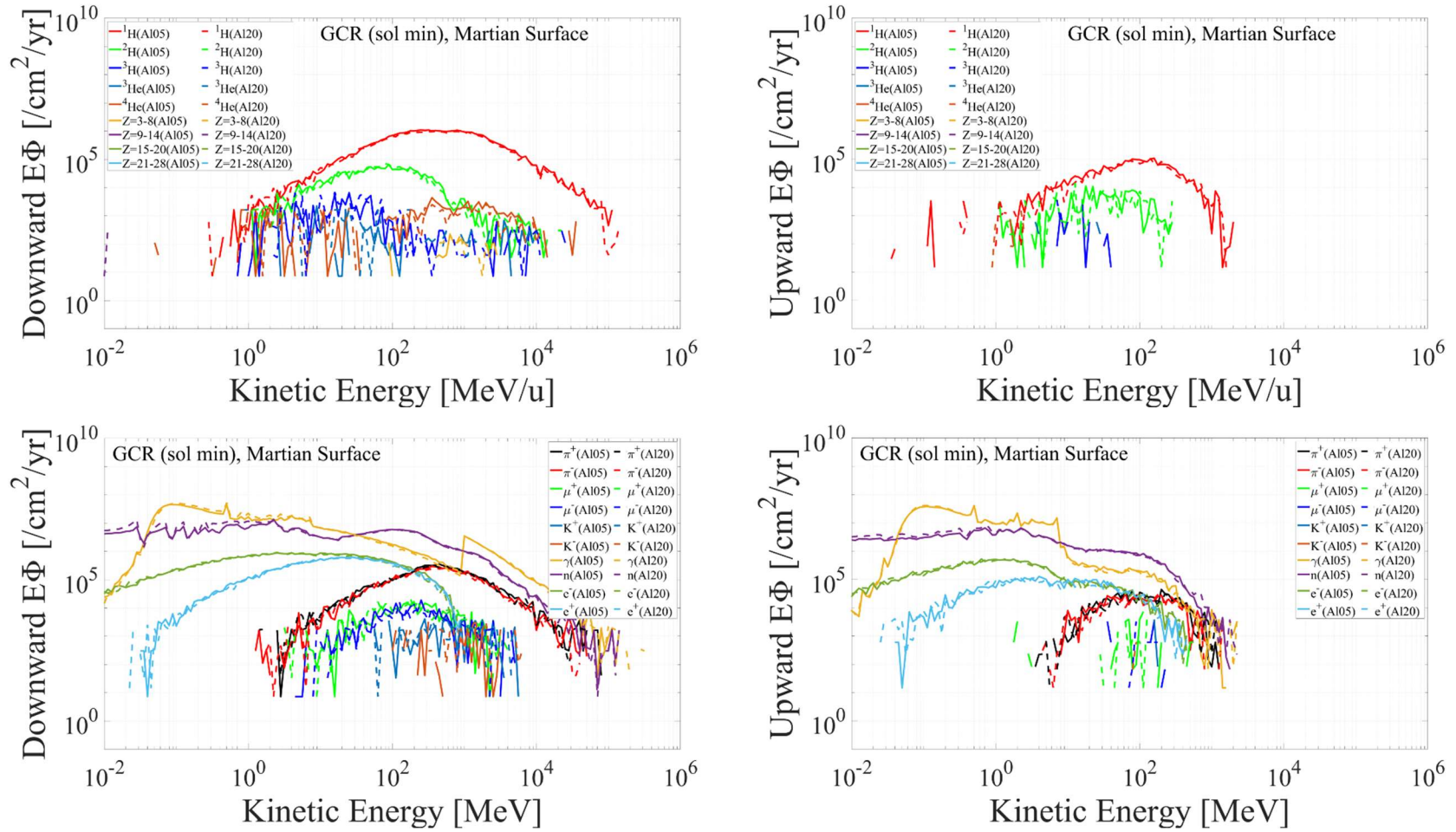
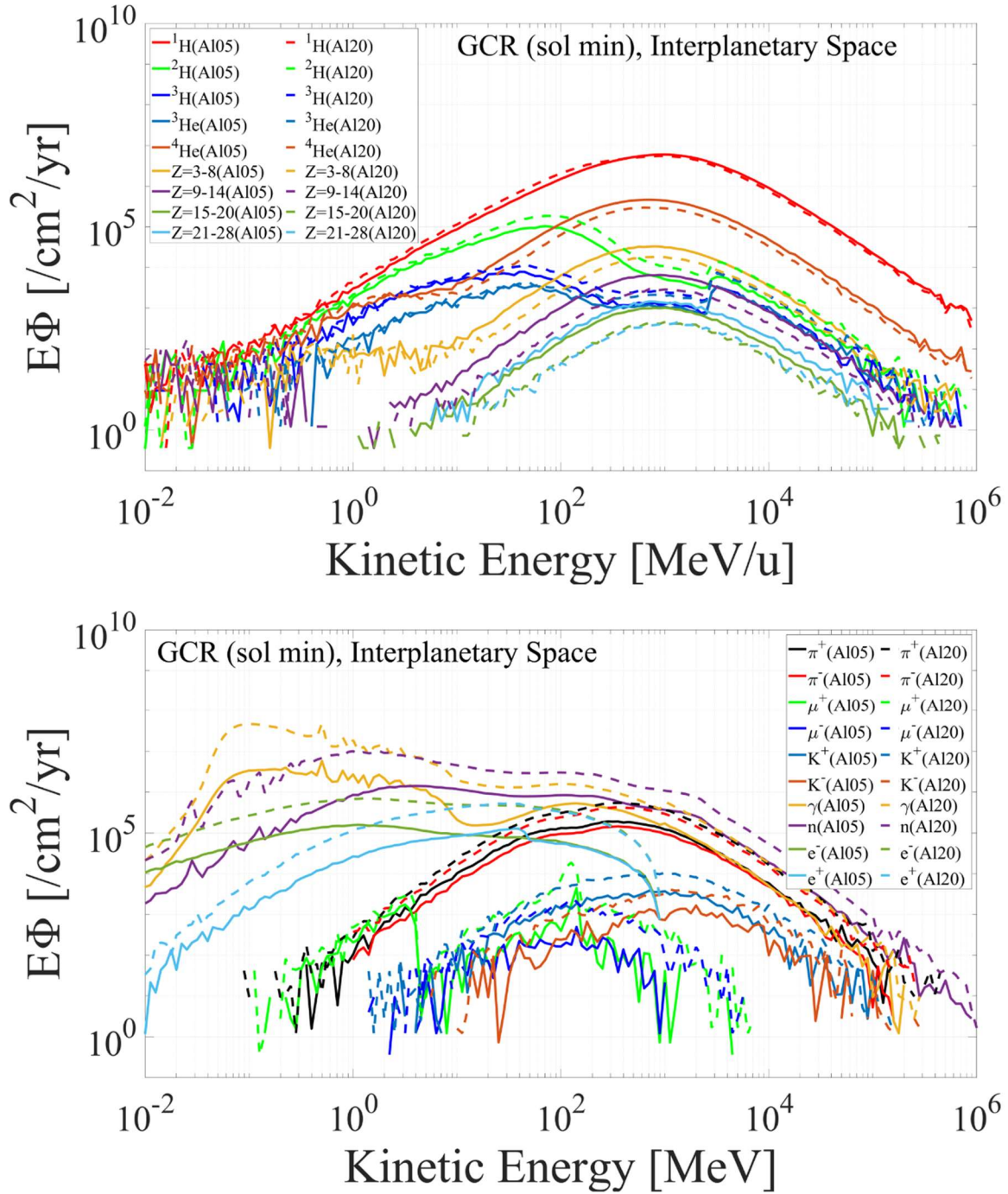Figure 4.5. Comparison of downward and upward ion and non-ion energy (lethargy) spectra behind thin (5 g/cm^2 Al) and typical (20 g/cm^2 Al) shielding during annual exposure to GCR near the solar minimum on the Martian surface.

Energy spectra during exposure to SPEs in August 1972 (Figure 4.6) and September 1989 (Figure 4.7) indicate a greater flux of low-energy protons and a lesser flux of high-energy protons during exposure to SPE in 1972 compared to SPE in 1989, as anticipated from their initial flux illustrated in Figure 3.4. For both events, heavy ions are barely shown behind aluminum shielding, while a number of secondary pions are generated during exposure to high-energy protons in the 1989 SPE spectra. The electron and photon fluxes drop at around 1 MeV and change according to the pion flux for the energy range greater than 1 MeV.

Figure 4.8 illustrates the impact of shielding depth on the particle fluxes, highlighting that the number of protons with kinetic energy less than 400 MeV decreases significantly with heavier shielding, while it does not dramatically vary for higher energy range. Unlike GCR, secondary ^{2}H, ^{3}H, ^{3}He, and ^{4}He ions and low-energy ($<$ 10 MeV) electrons and photons tend to decrease with more shielding for SPE. In contrast, the number of secondary neutrons, pions, and high energy ($\geq$ 10 MeV) electrons and photons is shown to be increased along the shielding depth.

Figure 4.9 depicts downward and upward energy spectra inside the Martian habitat for 5 g/cm^2 and 20 g/cm^2 aluminum shielding. The simulation suggests that the proton flux decreases with heavier shielding while the overall particle flux is less dependent on aluminum shielding depth due to atmospheric shielding. Minimal $Z \geq 2$ ion fluxes inside the Martian habitat are expected during exposure to SPE, and the non-ion fluxes are anticipated to be much lower compared to interplanetary space or GCR exposure.
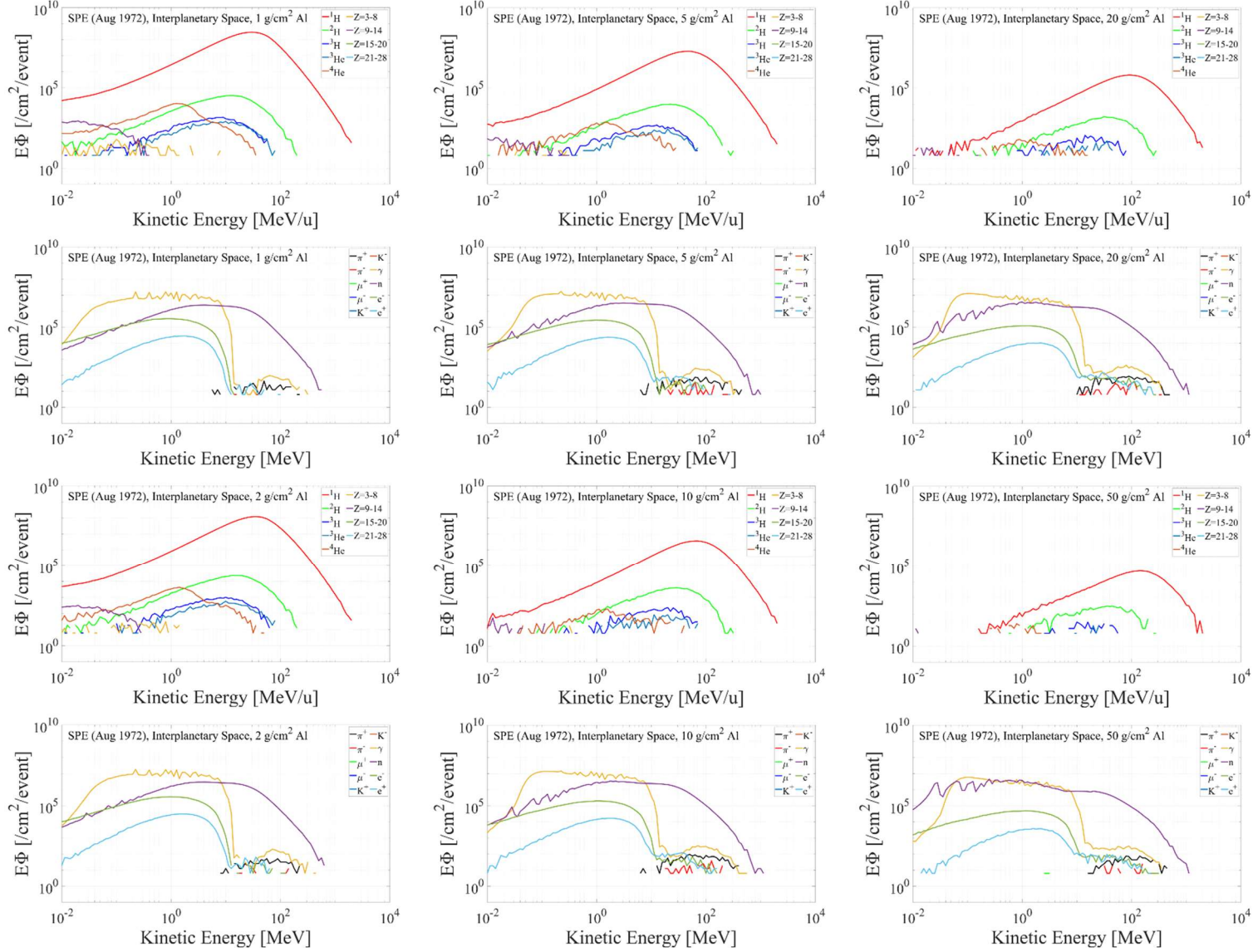
Figure 4.6. Ion and non-ion energy (lethargy) spectra during exposure to SPE on August 4, 1972, behind 1, 2, 5, 10, 20, and 50 g/cm^2 aluminum shielding in interplanetary space.
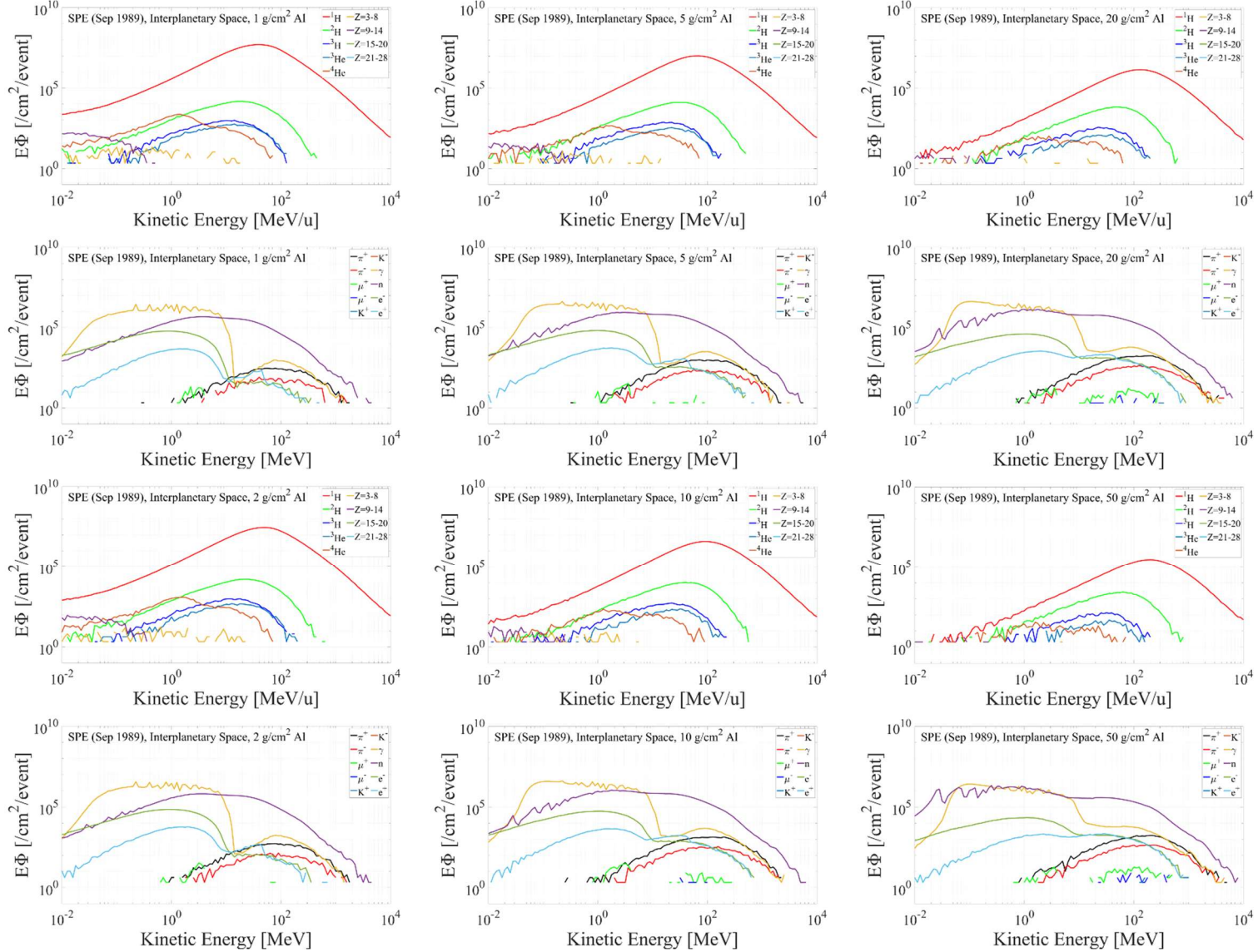
Figure 4.7. Ion and non-ion energy (lethargy) spectra during exposure to SPE on September 29, 1989, behind 1, 2, 5, 10, 20, and 50 g/cm^2 aluminum shielding in interplanetary space.
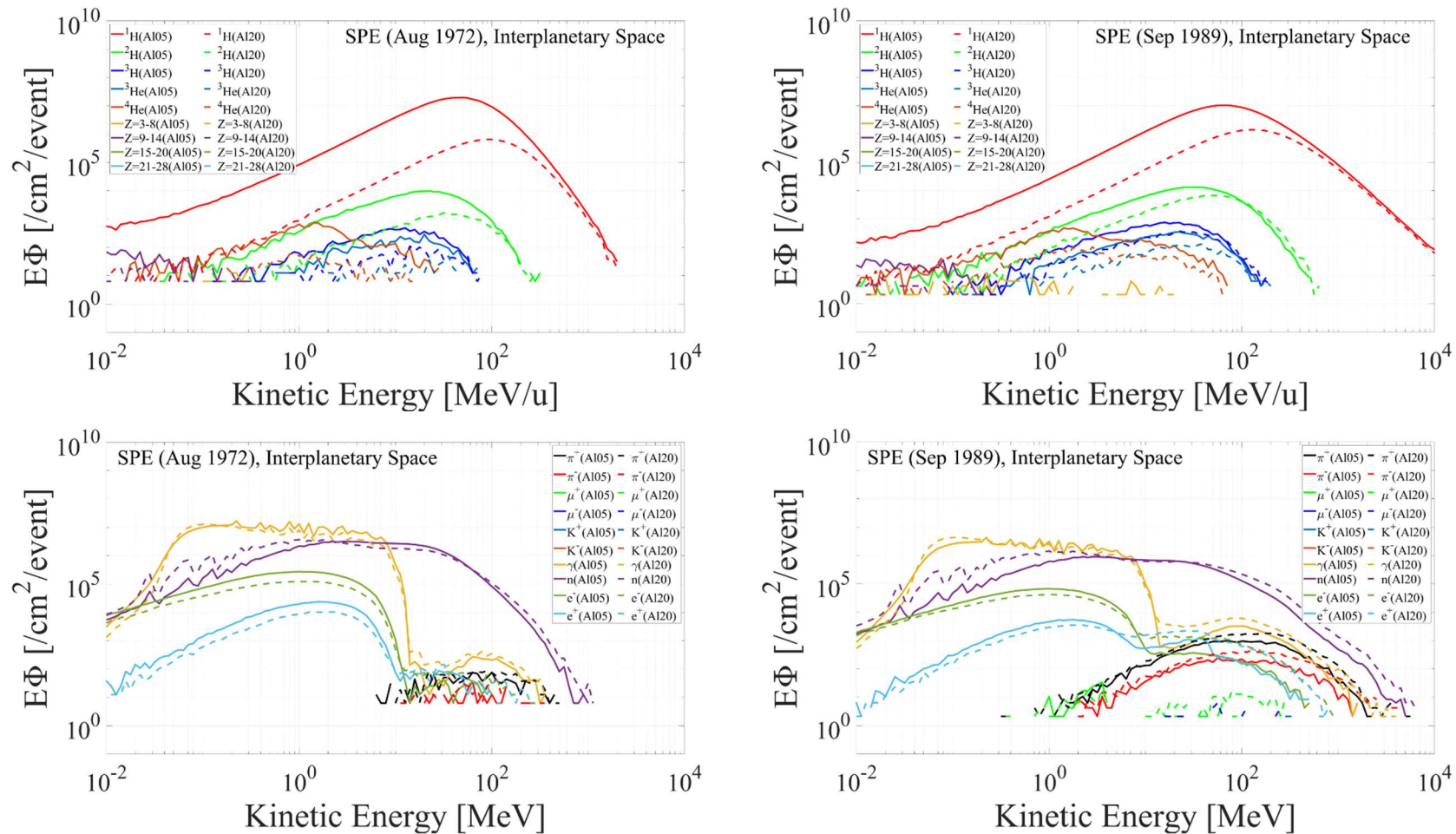
Figure 4.8. Comparison of ion and non-ion energy (lethargy) spectra behind thin (5 g/cm^2 Al) and typical (20 g/cm^2 Al) shielding for SPE exposure in interplanetary space.
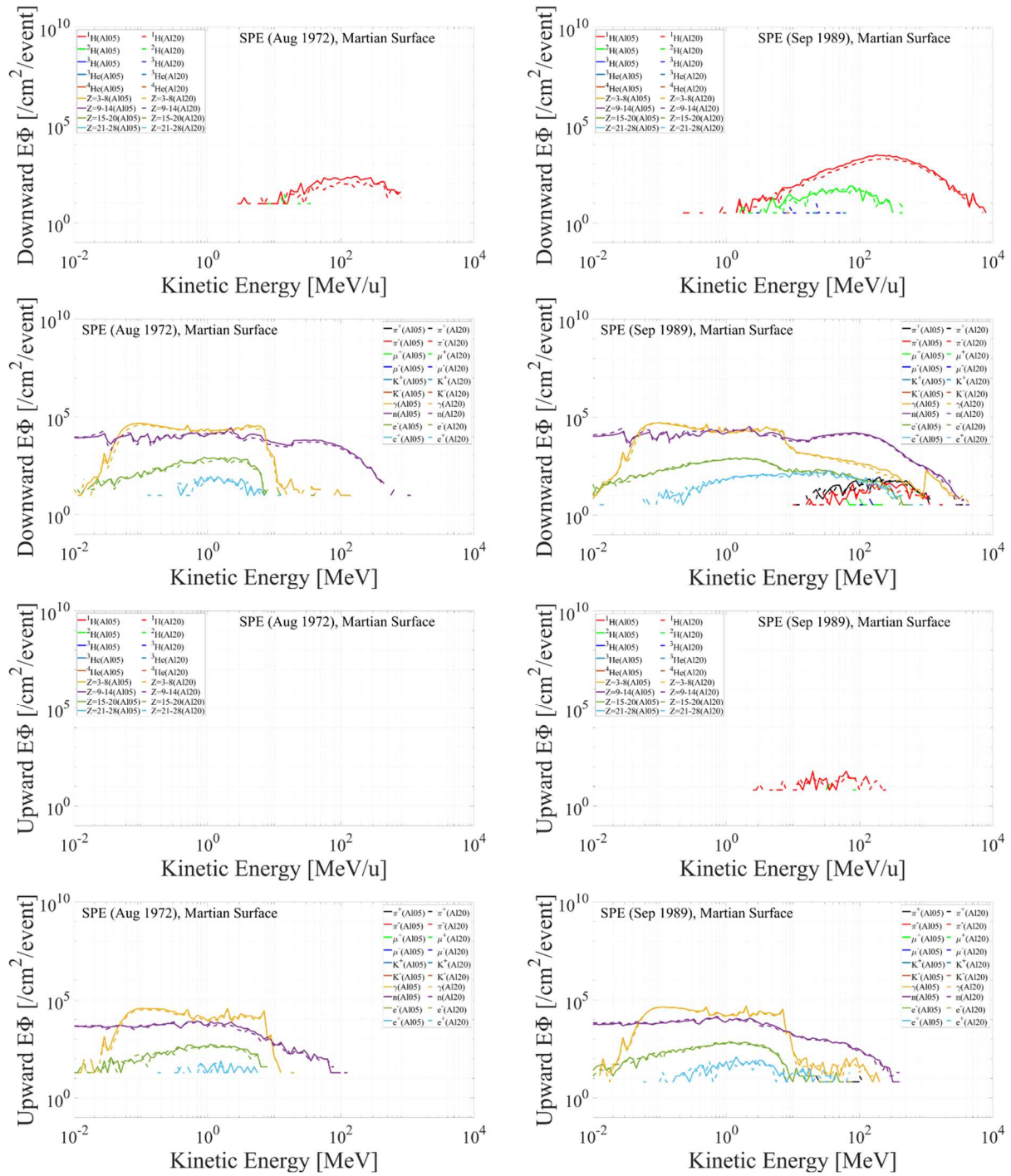
Figure 4.9. Comparison of downward and upward ion and non-ion energy (lethargy) spectra behind thin (5 g/cm^2 Al) and typical (20 g/cm^2 Al) shielding for SPE exposure on the Martian surface.

4.2: Tissue-specific Dose Quantities of Secondary Radiation in Interplanetary Space

In this chapter, simulations have been conducted to reconstruct the ICRP male human phantom within a spherical spacecraft situated in interplanetary space. The spacecraft has a 2-meter inner diameter and is equipped with aluminum shielding of varying thickness (1, 2, 5, 10, 20, and 50 g/cm^2). Due to the intricate geometry of the human phantom, computational challenges arose when using EGM and EGS5, resulting in unacceptable statistical instability. Consequently, EGM and EGS5 were not employed in contrast to the simulations discussed in Chapter 4.1. Instead, JQMD-2.0 was utilized for realistic nucleus interaction and secondary neutron generation.

The PHITS codes utilized in this chapter generated 1×10^8, 6×10^7, 2×10^7, 8×10^6, 6×10^6, and 3×10^6 numbers of Z=1, Z=2, Z=3-8, Z=9-14, Z=15-20, and Z=21-28 initial GCR ions, respectively. The simulations required varying computation time, with thin shielding taking approximately 1 to 2 days and thick shielding necessitating 5 days to 2 weeks. For SPEs, 2.5×10^8 protons were generated for both events in August 1972 and September 1989, with each code requiring one week of computation time.

The energy spectra of particles in each human organ were computed using the [T-Track] tally and subsequently converted to dose quantities. Figure 4.10 illustrates tissue-specific absorbed doses during exposure to GCR near the solar minimum in interplanetary space. The total absorbed dose, encompassing the contribution of all particles, is higher in external organs like the skin and lower in internal organs like the bladder. A notable observation is the decrease in $Z \geq 2$ ion contribution with increasing aluminum and tissue shielding thickness, while proton and secondary contributions rise, leading to an increased total absorbed dose with heavier aluminum shielding.
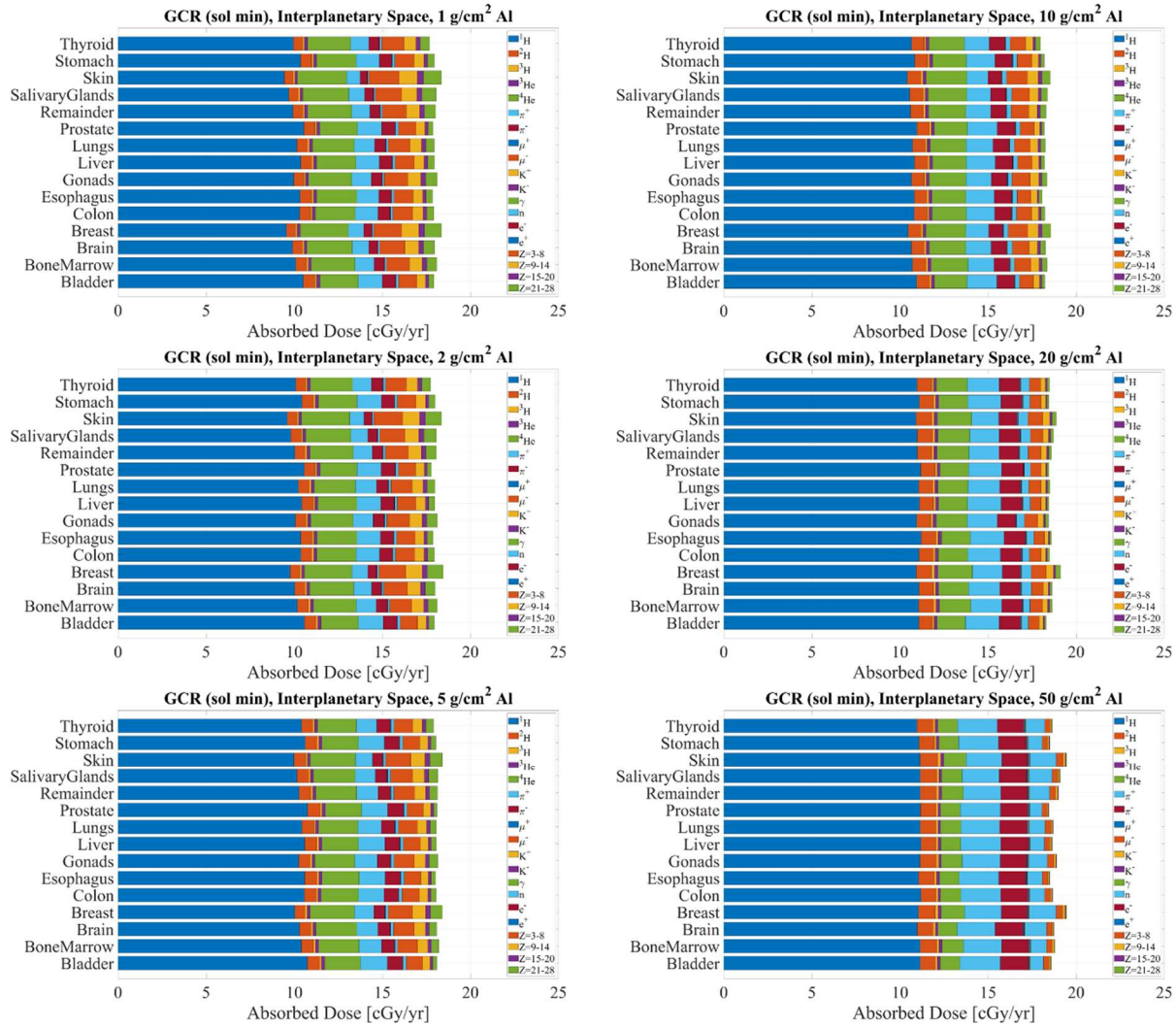
Figure 4.10. The absorbed dose in human organs during annual exposure to GCR near the solar minimum behind 1, 2, 5, 10, 20, and 50 g/cm^2 aluminum shielding in interplanetary space.

The increase in the absorbed dose of protons and secondary particles with augmented aluminum shielding is depicted in Figure 4.11. Proton dose includes contributions from both primary and secondary protons. For secondary mesons, less tissue shielding results in a lower absorbed dose for thin aluminum shielding, with the difference between organs diminishing as shielding increases. The absorbed dose of secondary neutrons in organs with less tissue shielding is also lower for thin (< 10 g/cm^2) aluminum shielding, but it becomes the opposite for heavier (≥ 10 g/cm^2) aluminum shielding. For instance, the neutron absorbed dose is lowest in skin and breast for 1 g/cm^2 aluminum shielding, while it is highest for 50 g/cm^2 aluminum shielding. Like secondary pions and kaons, the absorbed dose of protons is lowest in the organs with less tissue shielding for thin aluminum shielding, and it becomes very close to each other in all organs with heavy aluminum shielding.

The tissue-specific dose equivalent, assessed with the ICRP quality factor, is presented in Figure 4.12. Notably, the total dose equivalent strongly depends on the heavy ion contribution due to the increased quality factor of heavy ions. In instances of minimized aluminum and tissue shielding, such as skin behind 1 g/cm^2 aluminum, the dose equivalent can be as high as 77.2 cSv/yr during exposure to GCR near the solar minimum, while in organs behind heavy shielding, like prostate behind 50 g/cm^2 aluminum, it can be as low as 38.1 cSv/yr.

While the heavy ion dose equivalent decreases with shielding thickness, the dose equivalent of protons and secondary particles tends to increase, aligning with their augmented dose. Figure 4.13 indicates that the difference between the absorbed dose and the dose equivalent of secondary mesons is not significant, unlike heavy ions, suggesting the dominance of secondary mesons with energy greater than 1 MeV, i.e., with the low (~1) quality factor.
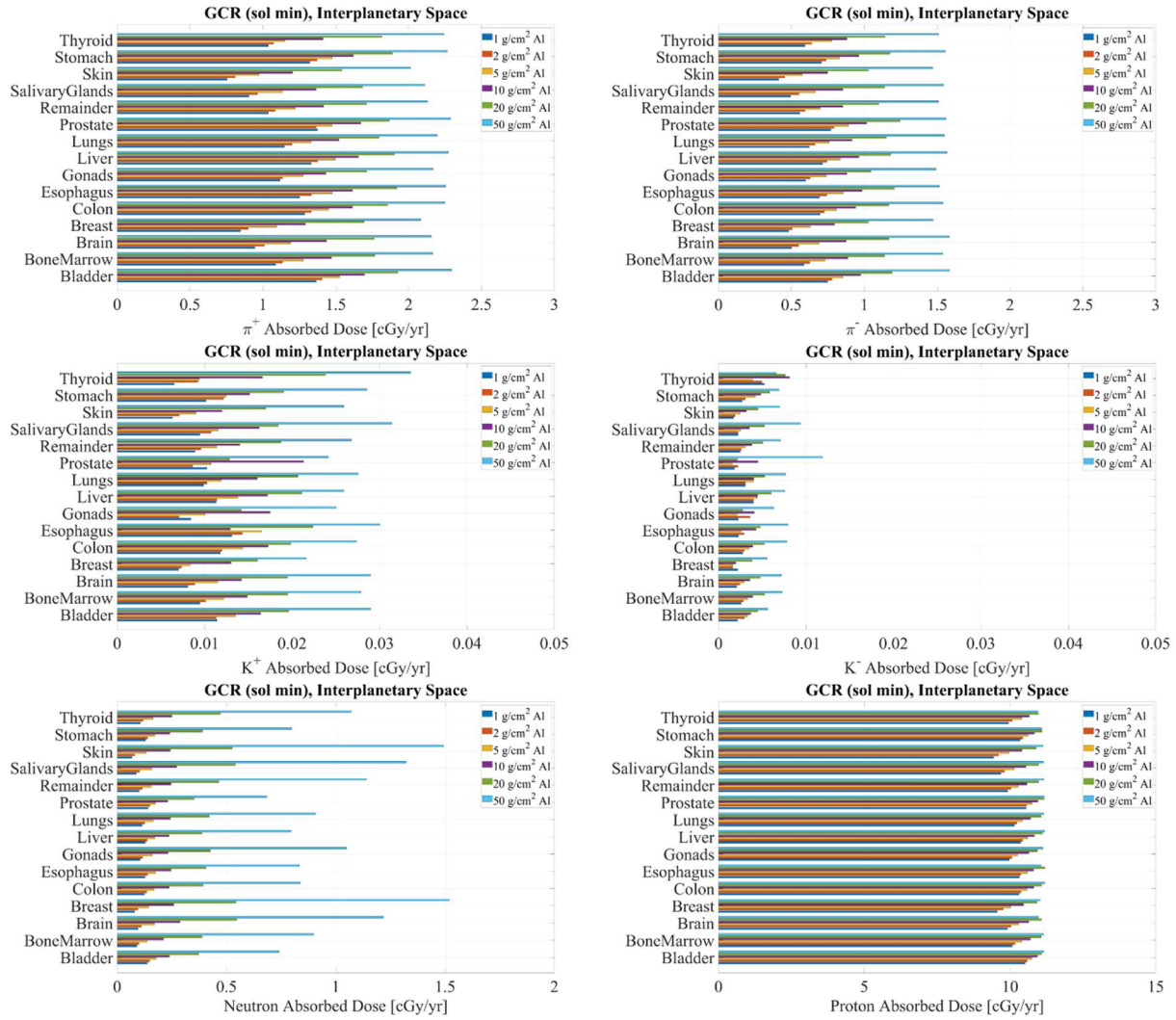
Figure 4.11. The absorbed dose of pions, kaons, neutrons, and protons in human organs during annual exposure to GCR near the solar minimum behind 1, 2, 5, 10, 20, and 50 g/cm^2 aluminum shielding in interplanetary space.

Figure 4.12. The ICRP dose equivalent in human organs during annual exposure to GCR near the solar minimum behind 1, 2, 5, 10, 20, and 50 g/cm² aluminum shielding in interplanetary space.

Figure 4.13. The ICRP dose equivalent of pions, kaons, neutrons, and protons in human organs during annual exposure to GCR near the solar minimum behind 1, 2, 5, 10, 20, and 50 g/cm^2 aluminum shielding in interplanetary space.

97

Evidence of this phenomenon is presented in Figure 4.14 and Figure 4.15, illustrating the meson, neutron, and the proton fluxes in human organs behind 5 g/cm^2 and 20 g/cm^2 aluminum shielding. As anticipated, the flux of secondary mesons increases with energy until a few hundred MeV, followed by a decline. This peak in the energy spectra is due to the primary GCR spectra and the dynamic process of meson production. The proton flux also exhibits a peak at a few hundred MeV, attributed to the absorption and energy reduction of GCR ions in the aluminum shielding. Neutron energy spectra remain relatively flat due to the generation of low-energy neutrons.

The shape of the particle energy spectra behind different shielding depths is similar to each other, while increased shielding induces more secondary yield, which results in a higher flux of secondary mesons and neutrons in human organs. As a large number of protons are also generated by the interaction between GCR heavy ions and the aluminum shielding, the proton flux also increases with increased shielding amount, even though primary GCR protons are attenuated by the shielding.
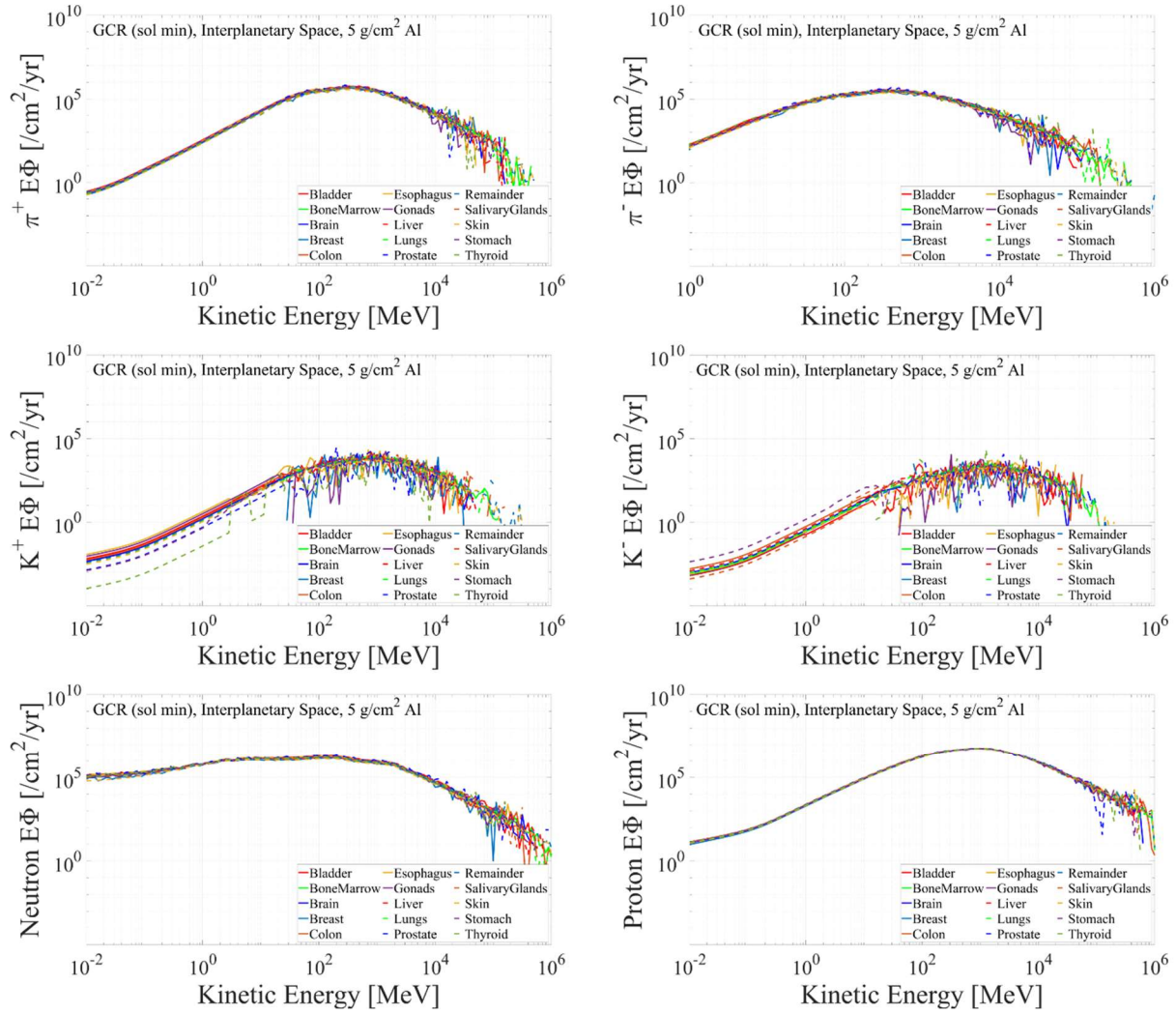
Figure 4.14. The energy (lethargy) spectra of pions, kaons, neutrons, and protons in human organs during annual exposure to GCR near the solar minimum behind 5 g/cm² aluminum shielding in interplanetary space.
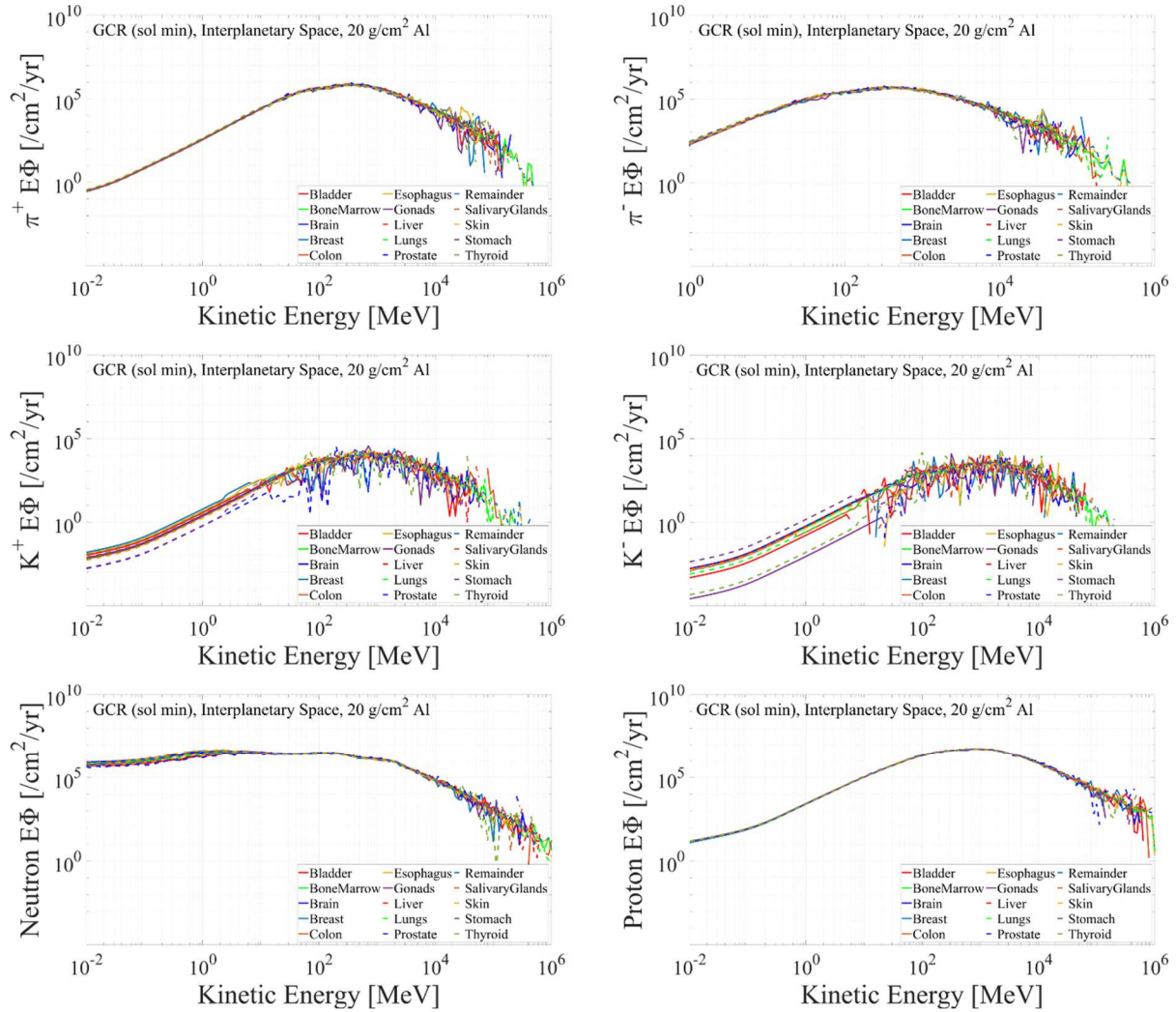
Figure 4.15. The energy (lethargy) spectra of pions, kaons, neutrons, and protons in human organs during annual exposure to GCR near the solar minimum behind 20 g/cm^2 aluminum shielding in interplanetary space.

The dose equivalent assessed by the NSCR quality factors is shown in Figure 4.16. Parameters for leukemia were used for bone marrow, and parameters for solid cancer were applied to all other organs. As shown in Figure 3.6, the quality factor for leukemia is lower than for solid cancer, which results in a decreased dose equivalent in bone marrow than in other organs. Compared to

the ICRP model, the NSCR model for solid cancer suggests a higher dose equivalent of the particles lighter than the Z=2 ion. This trend is more apparent in Figure 4.17, where increased dose equivalents of mesons and protons are suggested compared to the values in Figure 4.13. On the other hand, the NSCR model provides a lower dose equivalent of heavy ions than the ICRP model, resulting in a decreased dose equivalent for thin shielding but a similar dose equivalent for thick shielding. In other words, the NSCR dose equivalent reduces relatively slowly with increasing aluminum shielding depth. In addition, it is indicated that the total dose equivalent may even increase with heavy (≥ 50 g/cm^2 aluminum) shielding due to the increased amount of secondary neutrons, even though the heavy ion dose equivalent reduces. Figure 4.18 illustrates the effective dose of mesons, neutrons, and protons, along with the total effective dose, assessed with both ICRP and NSCR models. A rise in secondary effective dose with shielding thickness is evident, as listed in Table 4.1, suggesting that the NSCR effective dose of protons and secondary mesons is higher than their ICRP effective dose. The neutron NSCR effective dose behind thick shielding is indicated to be lower than the neutron ICRP effective dose due to different tissue weighting factors. Specifically, the breast dose equivalent, which is higher compared to other organs, is not taken into account to assess the effective dose for males in the sex-dependent NSCR model, while the tissue weighting factor for the breast is 0.12 for both males and females in the ICRP model. The total effective dose assessed with the NSCR model is also lower compared to the ICRP model due to the different tissue weighting factors and decreased heavy ion effective dose. As indicated by the dose equivalent, slower changes in total NSCR effective dose compared to the ICRP model and a slight increase at 50 g/cm^2 shielding is shown. The simulation suggests 59.5 cSv and 43.4 cSv of the total effective dose with ICRP and NSCR models, respectively, during annual exposure

101

to GCR near the solar minimum behind 1 g/cm^2 aluminum shielding, and it is reduced to 45.3 cSv

and 38.7 cSv with each model for the typical (20 g/cm^2) aluminum shielding.
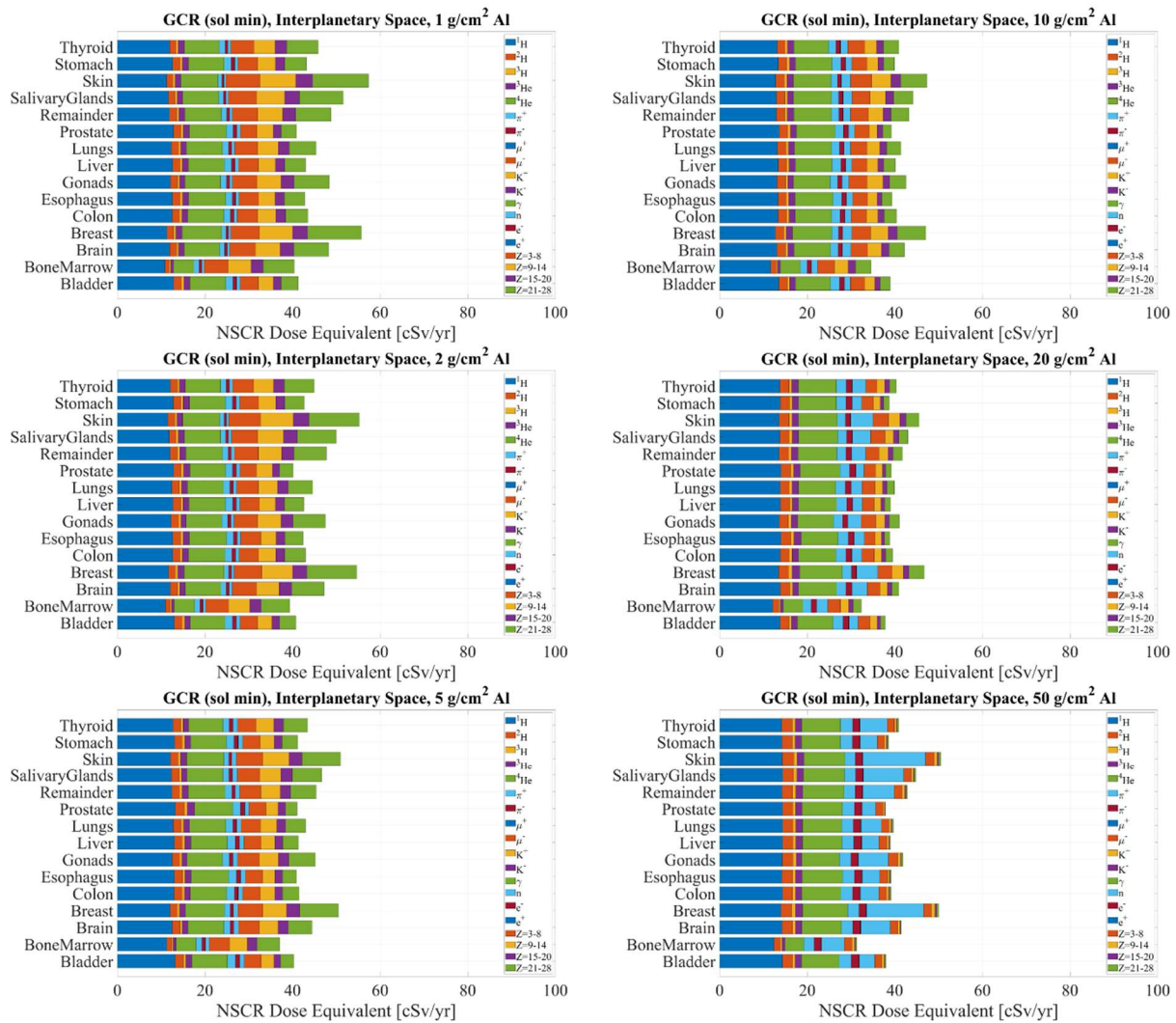
Figure 4.16. The NSCR dose equivalent in human organs during annual exposure to GCR near the solar minimum behind 1, 2, 5, 10, 20, and 50 g/cm^2 aluminum shielding in interplanetary space.
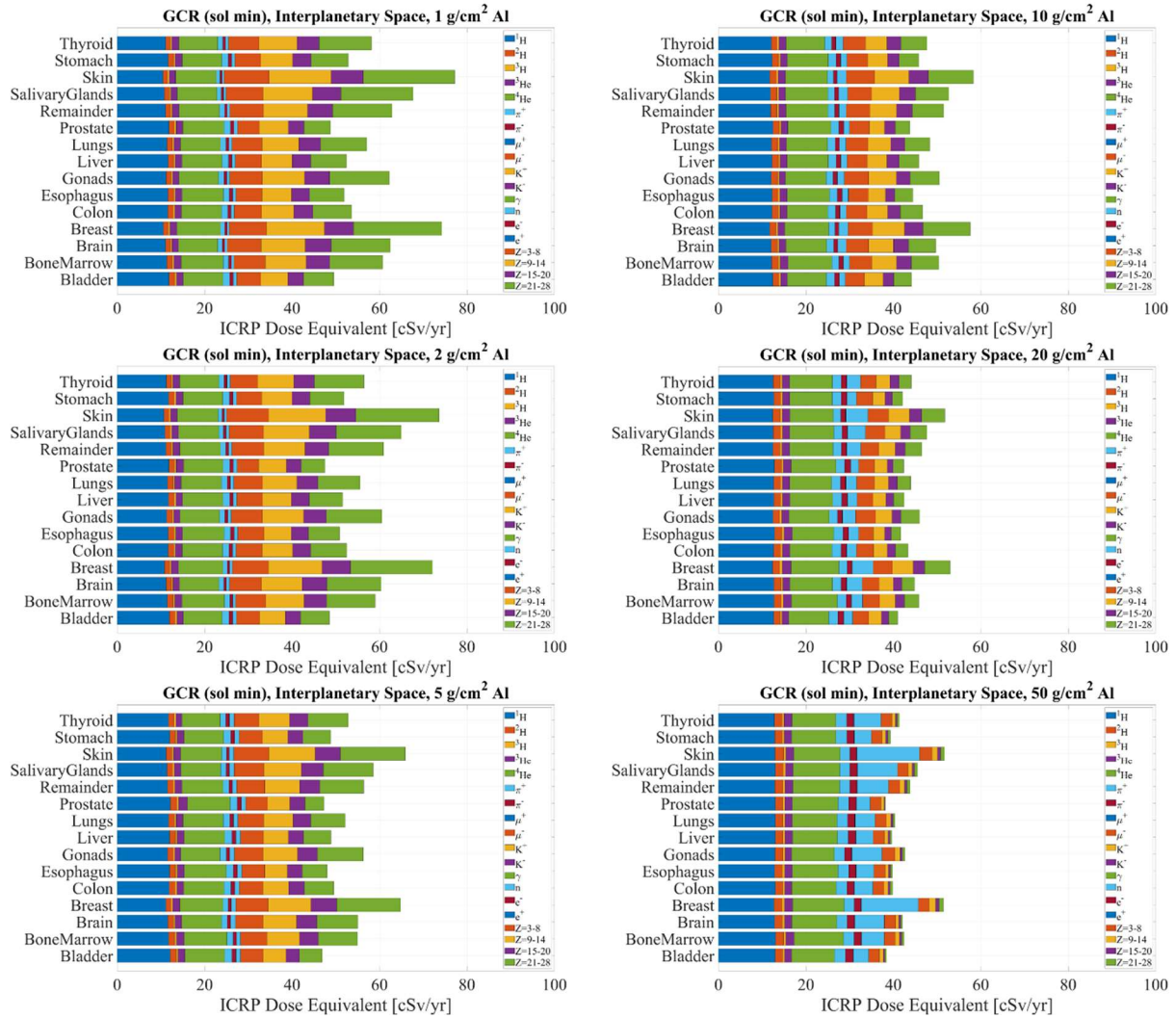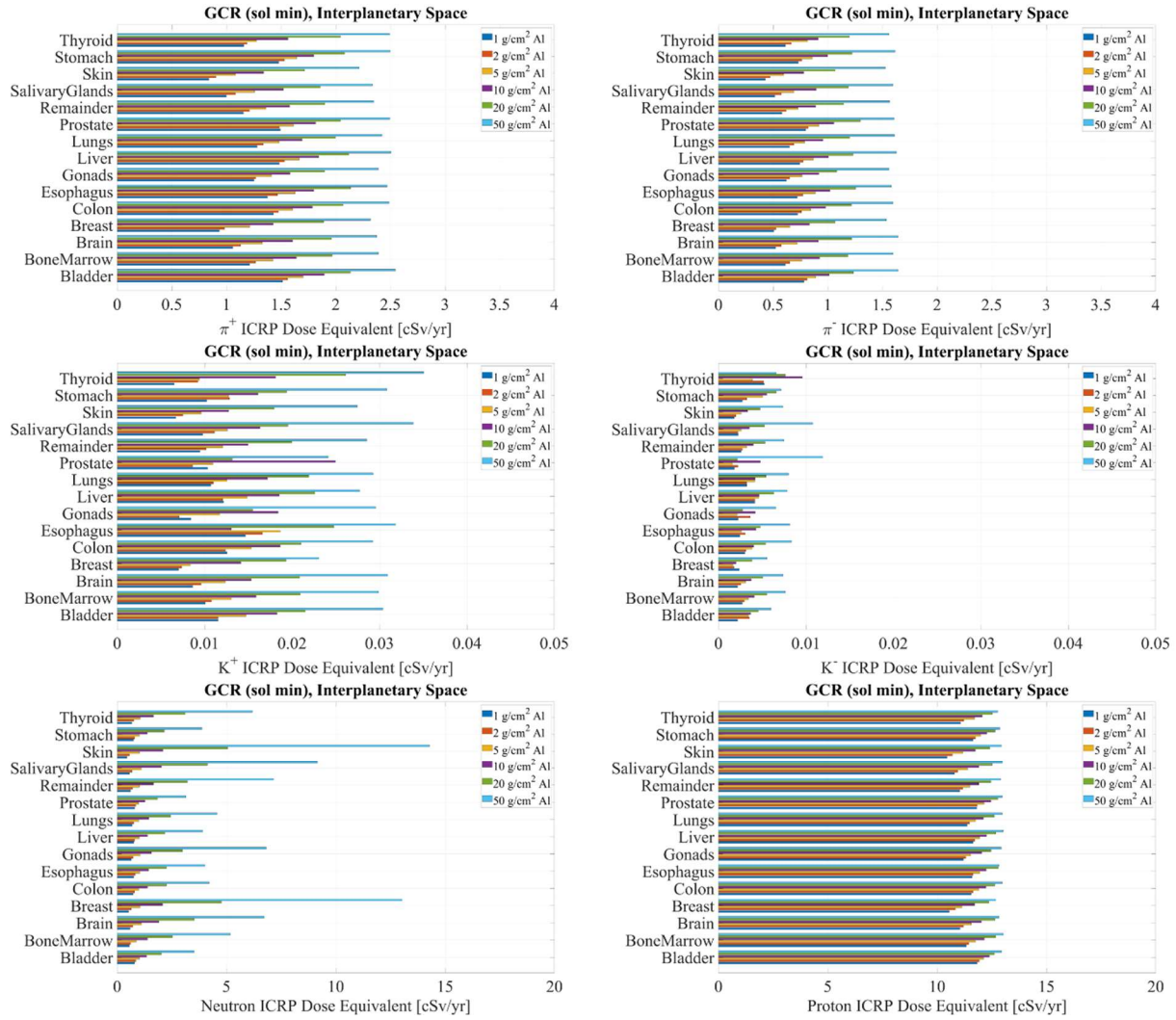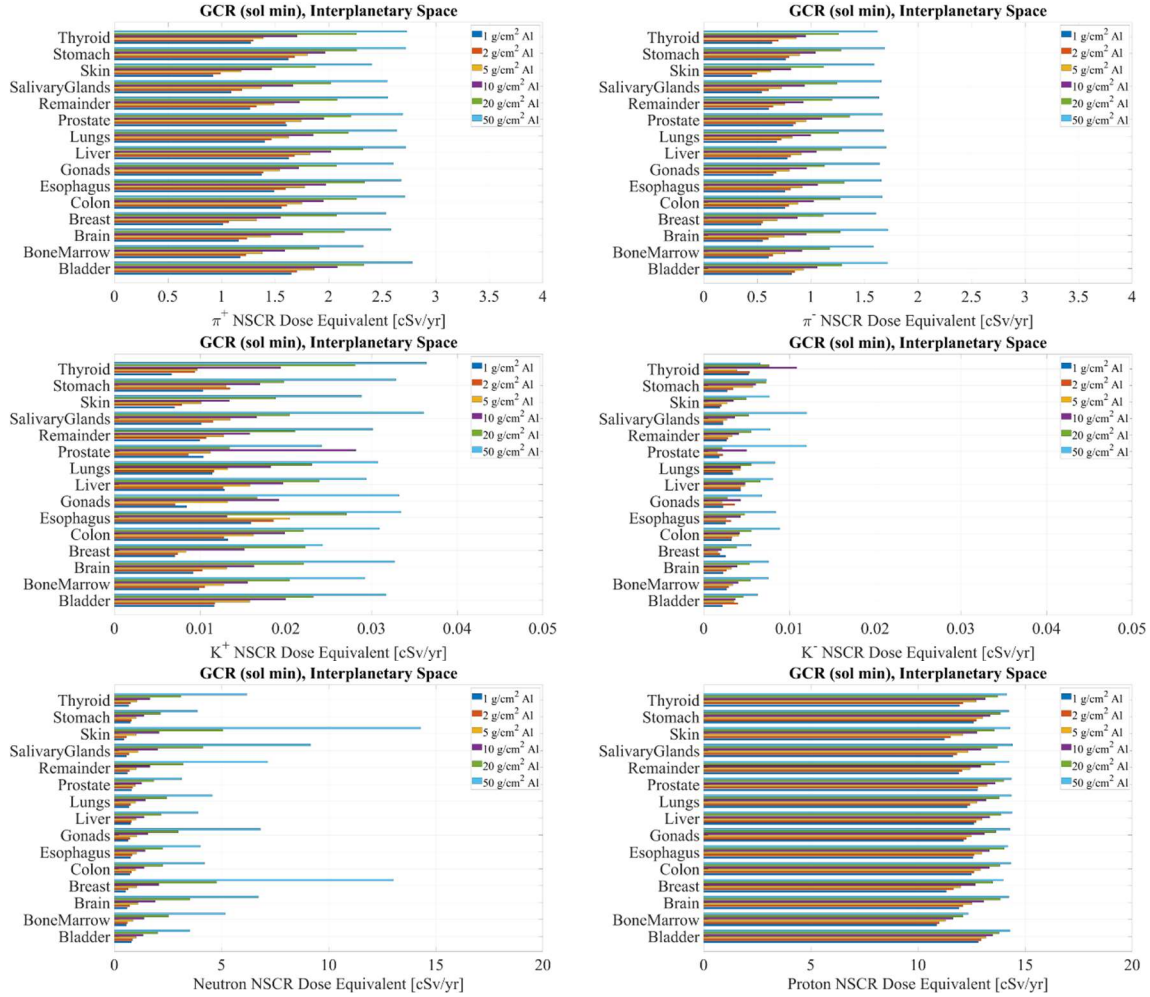
Figure 4.17. The NSCR dose equivalent of pions, kaons, neutrons, and protons in human organs during annual exposure to GCR near the solar minimum behind 1, 2, 5, 10, 20, and 50 g/cm^2 aluminum shielding in interplanetary space.

Table 4.1. The sum of the effective doses of neutrons, pions, and kaons (with % contribution to the total) and the total effective dose during annual exposure to GCR near the solar minimum behind 1, 2, 5, 10, 20, and 50 g/cm^2 aluminum shielding in interplanetary space.

	Neutron + Pion + Kaon Effective Dose [cSv/yr]		Total Effective Dose [cSv/yr]	
Shielding	ICRP	NSCR	ICRP	NSCR
1 g/cm^2 Al	2.56 (4.31%)	2.83 (6.51%)	59.5	43.4
2 g/cm^2 Al	2.72 (4.70%)	2.99 (7.01%)	57.9	42.7
5 g/cm^2 Al	3.26 (6.04%)	3.50 (8.49%)	53.9	41.2
10 g/cm^2 Al	4.17 (8.43%)	4.36 (11.0%)	49.5	39.7
20 g/cm^2 Al	6.04 (13.3%)	6.01 (15.5%)	45.3	38.7
50 g/cm^2 Al	10.2 (24.0%)	9.31 (23.9%)	42.5	39.0
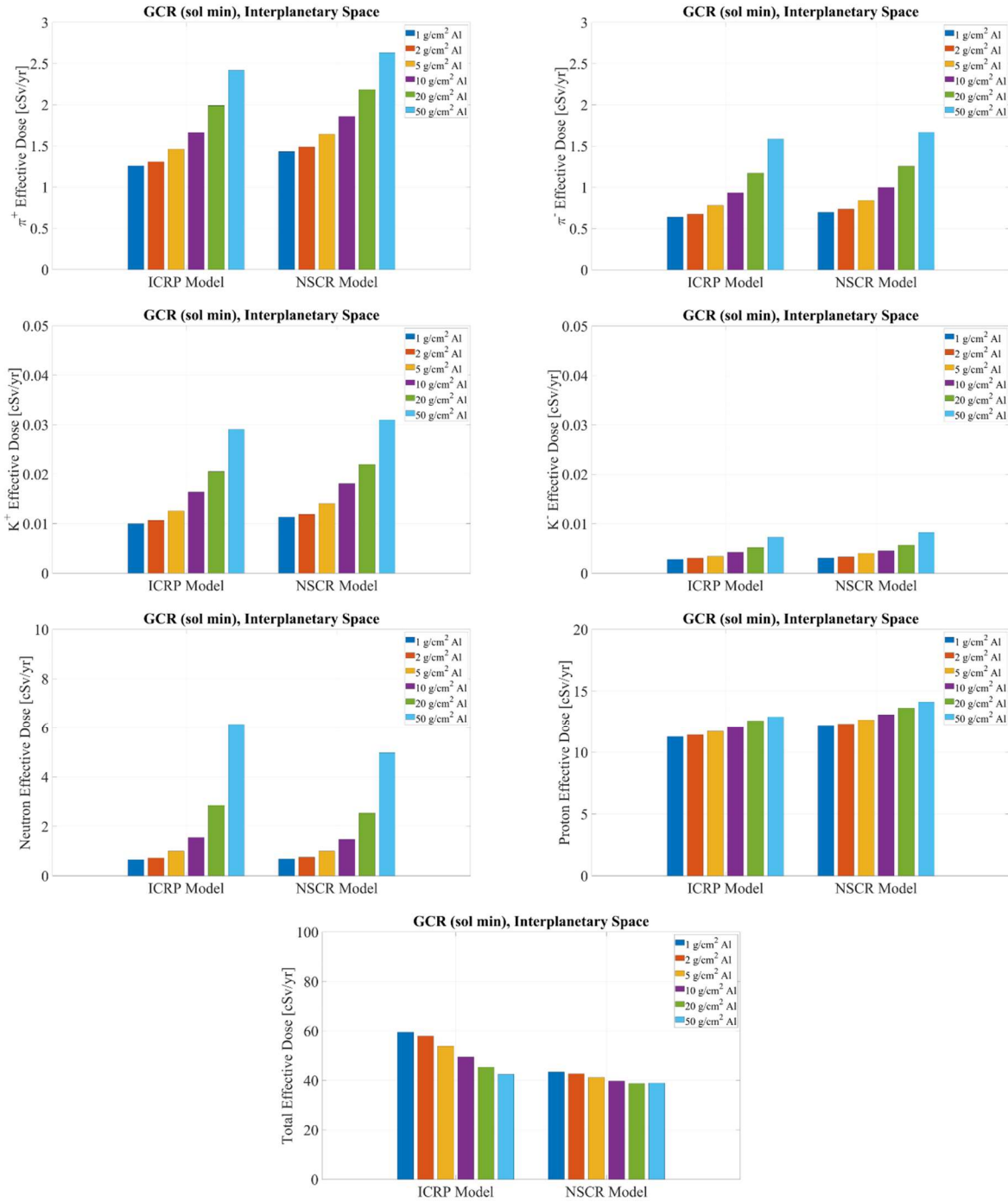
Figure 4.18. The effective dose of pions, kaons, neutrons, and protons, and the total effective dose assessed with the ICRP and NSCR models for annual exposure to GCR near the solar minimum behind 1, 2, 5, 10, 20, and 50 g/cm² aluminum shielding in interplanetary space.

The absorbed dose during exposure to large SPEs in interplanetary space is investigated in Figure 4.19. Unlike GCR exposure, the absorbed dose during SPE exposure exhibits significant variation with tissue shielding due to a high number of low-energy protons with a short range.

The disparity is particularly pronounced with thin aluminum shielding. For example, the absorbed dose in the skin during exposure to the 1972 SPE behind 1 g/cm^2 aluminum is 822 cGy, while it is 5.79 cGy in the prostate. The variation of the absorbed dose from organ to organ decreases as the aluminum shielding depth increases, i.e., the total (aluminum + tissue) shielding amounts become closer to each other for different organs, though the difference is still noticeable compared to GCR exposure. It is observed that the absorbed dose behind thin shielding is higher for the 1972 SPE compared to the 1989 SPE due to the high overall initial proton flux in the 1972 event. Conversely, the absorbed dose for the 1989 SPE behind thick shielding is higher than for the 1972 SPE, attributed to the 1989 event containing more high-energy protons capable of penetrating heavy aluminum shielding.

The simulation indicates little to no secondary mesons in human organs during SPE exposure. This is attributed to the reduced number of high-energy protons and the absence of heavy ions in the energy range of 300 – 5000 MeV/u, which is crucial for meson production. Protons and secondary neutrons play a dominant role in dose quantities. Figure 4.20 illustrates the total absorbed dose, as well as the absorbed dose of protons and secondary neutrons for the 1972 SPE and the 1989 SPE behind different shielding amounts. The decrease in total and proton absorbed dose with increased shielding is evident, while neutron absorbed dose peaks at around 10 g/cm^2 shielding depth for the 1972 SPE and around 20 g/cm^2 for the 1989 SPE.
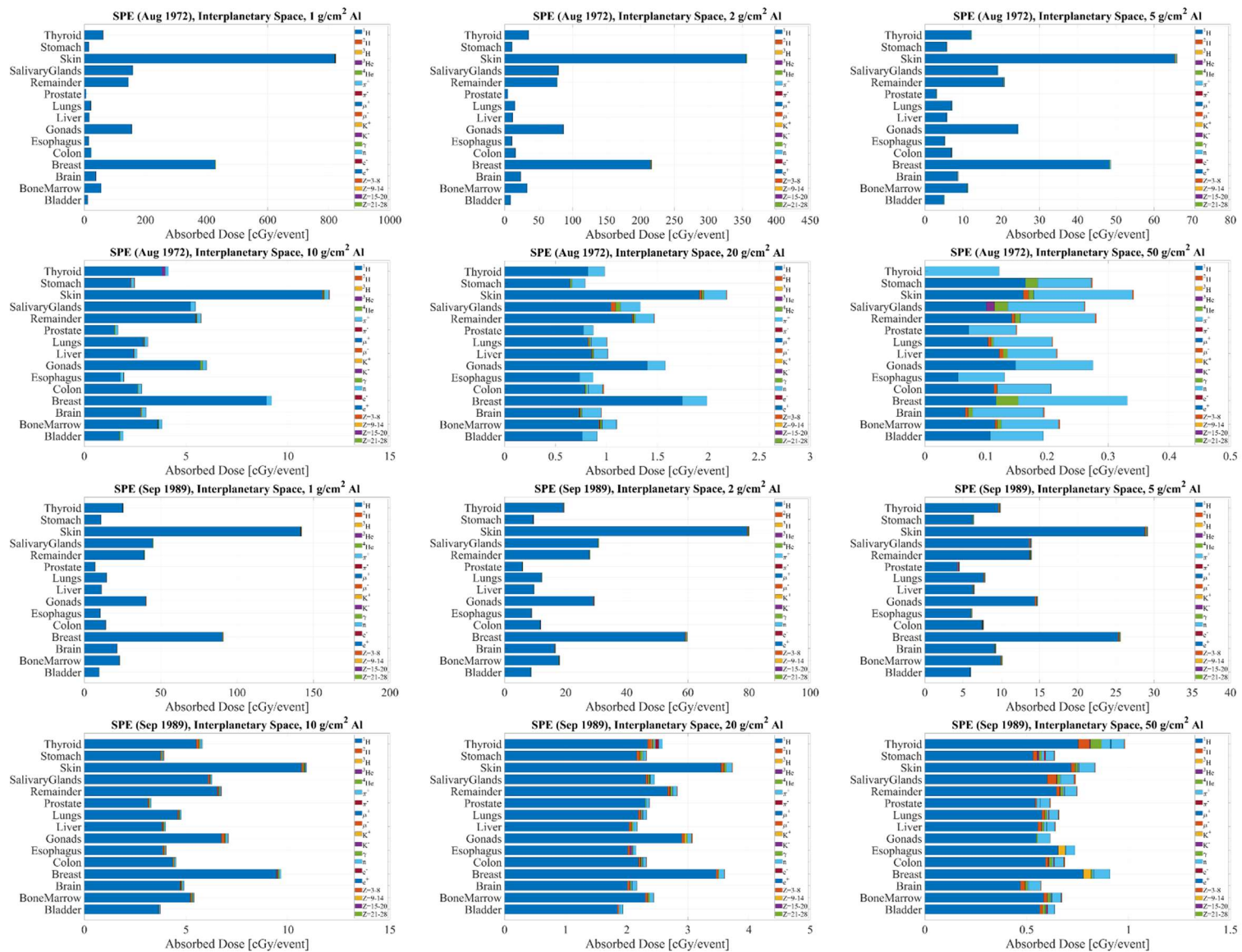
Figure 4.19. The absorbed dose in human organs during exposure to SPEs on August 4, 1972, and September 29, 1989, behind 1, 2, 5, 10, 20, and 50 g/cm² aluminum shielding in interplanetary space.
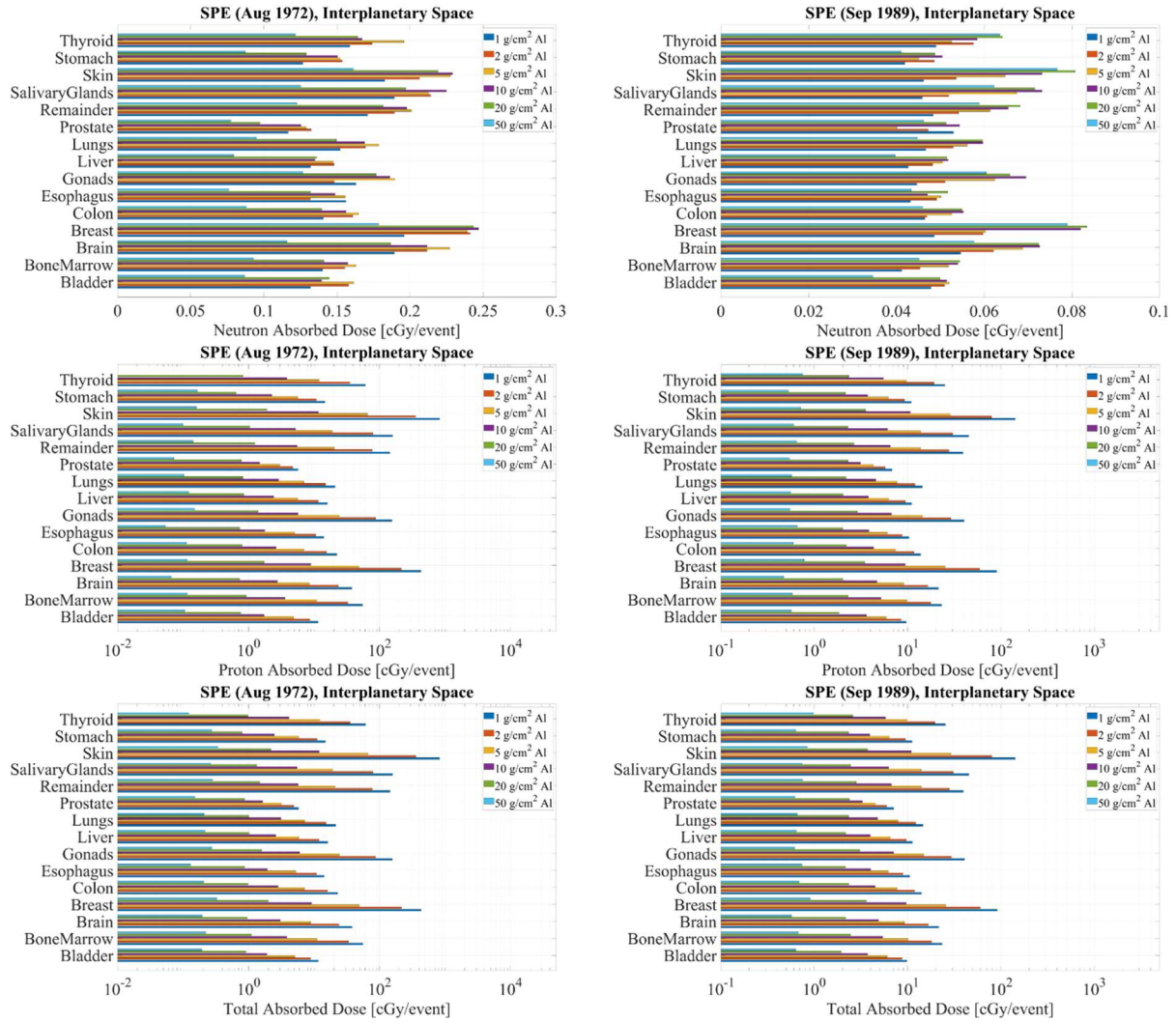
Figure 4.20. The absorbed dose of neutrons and protons and the total absorbed dose in human organs during exposure to SPEs on August 4, 1972, and September 29, 1989, behind 1, 2, 5, 10, 20, and 50 g/cm^2 aluminum shielding in interplanetary space.
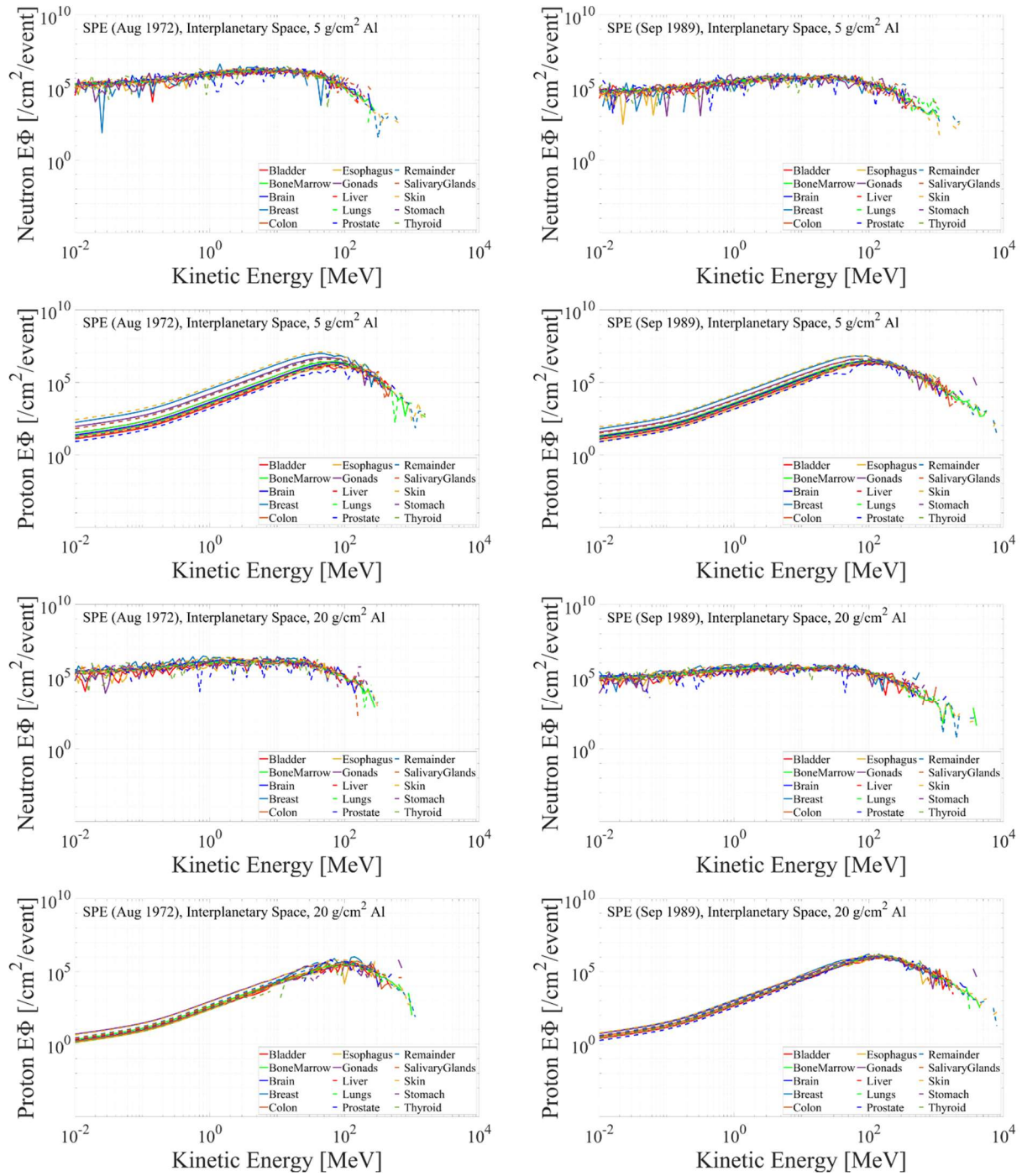
Figure 4.21. The neutron and proton energy (lethargy) spectra in human organs behind 5 g/cm^2 and 20 g/cm^2 aluminum shielding during exposure to SPEs on August 4, 1972, and September 29, 1989.

The tissue-specific energy spectra of neutrons and protons behind 5 g/cm^2 and 20 g/cm^2 aluminum shielding for the 1972 SPE and the 1989 SPE are depicted in Figure 4.21. As anticipated by their initial spectra, an increased flux of high-energy protons and neutrons is suggested for the 1989 SPE compared to the 1972 SPE. The proton fluxes exhibit different levels in various organs for 5 g/cm^2 aluminum, while they become closer and peak at higher energy as shielding increases. Similar to GCR exposure, the neutron flux shows less variation over a wide energy range, while the change in energy spectra with shielding thickness is relatively smaller compared to GCR exposure.

The ICRP dose equivalent in each human organ during exposure to the 1972 SPE and the 1989 SPE behind varying aluminum shielding is presented in Figure 4.22. The skin dose equivalent behind 1 g/cm^2 aluminum shielding is notably high, reaching 1387 cSv for the 1972 SPE and 226 cSv for the 1989 SPE, while the dose equivalent in internal organs such as the prostate can be as low as 7.97 cSv for the 1972 SPE and 10.3 cSv for the 1989 SPE. However, the dose equivalent can be effectively reduced by a typical amount of spacecraft shielding, like 20 g/cm^2 aluminum. Behind 20 g/cm^2 aluminum shielding, the dose equivalent is as high as 5.41 cSv and 6.07 cSv in external organs for the 1972 SPE and 1989 SPE, respectively, and as low as 1.30 cSv and 2.49 cSv in internal organs for each event. The proton dose decreases dramatically with shielding depth, making secondary neutrons important for thicker shielding. Although the absorbed value of neutron dose equivalent decreases for more than 10 ~ 20 g/cm^2 aluminum shielding, their contribution to the total dose equivalent increases. For example, the dose equivalent of neutrons in the skin behind 20 g/cm^2 aluminum for the 1972 SPE is 2.41 cSv, constituting 44.5% of the total dose equivalent, while it is 1.61 cSv and 78.3% for 50 g/cm^2 aluminum. Figure 4.23 displays the neutron, proton, and total ICRP dose equivalent for different shielding amounts during exposure

to SPEs in August 1972 and September 1989, illustrating the dramatic decrease in proton and total dose equivalent with increased shielding and the peak in the neutron dose equivalent at $10 \sim 20$ g/cm^2 shielding depth, consistent with the absorbed dose tendency.

Figures 4.24 and 4.25 present the NSCR version of Figures 4.22 and 4.23. As shown for GCR exposure, the NSCR parameters for solid cancer suggest a lower dose equivalent of heavy ions and a higher dose equivalent of particles lighter than Z=2 ions compared to the ICRP model. This results in an increased total dose equivalent due to the dominant contribution of protons and neutrons, unlike the important heavy ion contribution for GCR exposure.
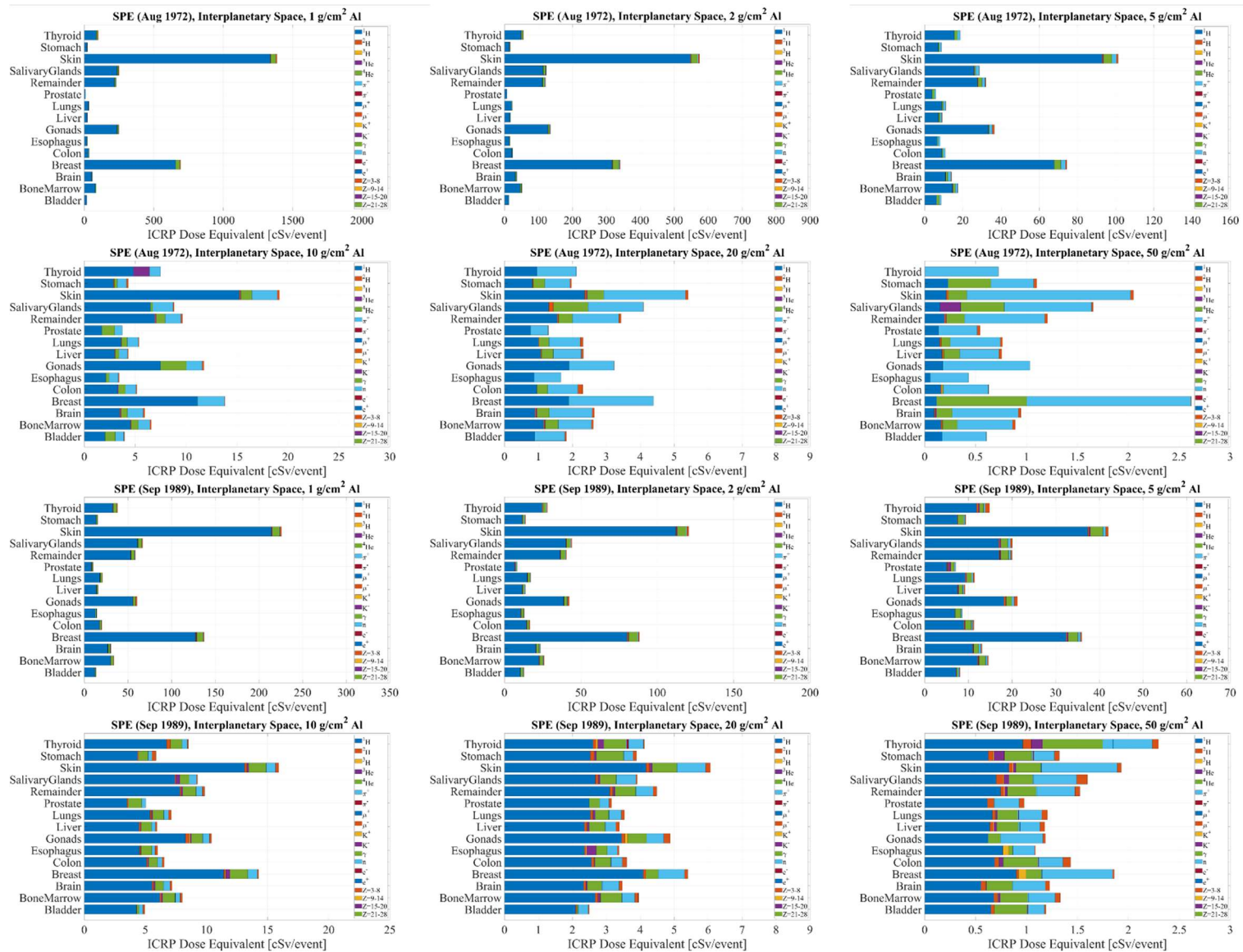
Figure 4.22. The ICRP dose equivalent in human organs during exposure to SPEs on August 4, 1972, and September 29, 1989, behind 1, 2, 5, 10, 20, and 50 g/cm² aluminum shielding in interplanetary space.

111
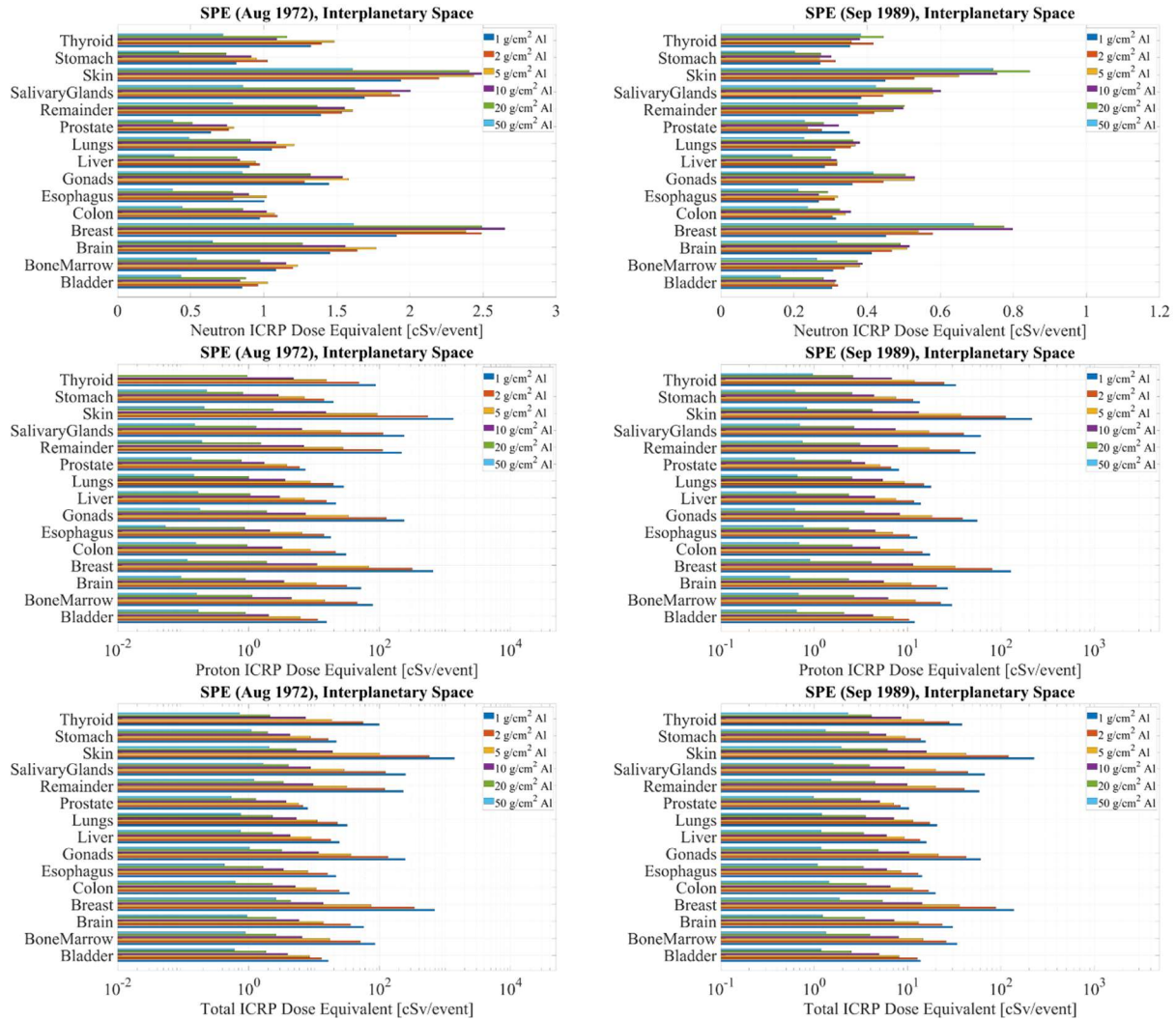
Figure 4.23. The ICRP dose equivalent of neutrons and protons and the total ICRP dose equivalent during exposure to SPEs on August 4, 1972, and September 29, 1989, behind 1, 2, 5, 10, 20, and 50 g/cm^2 aluminum shielding in interplanetary space.
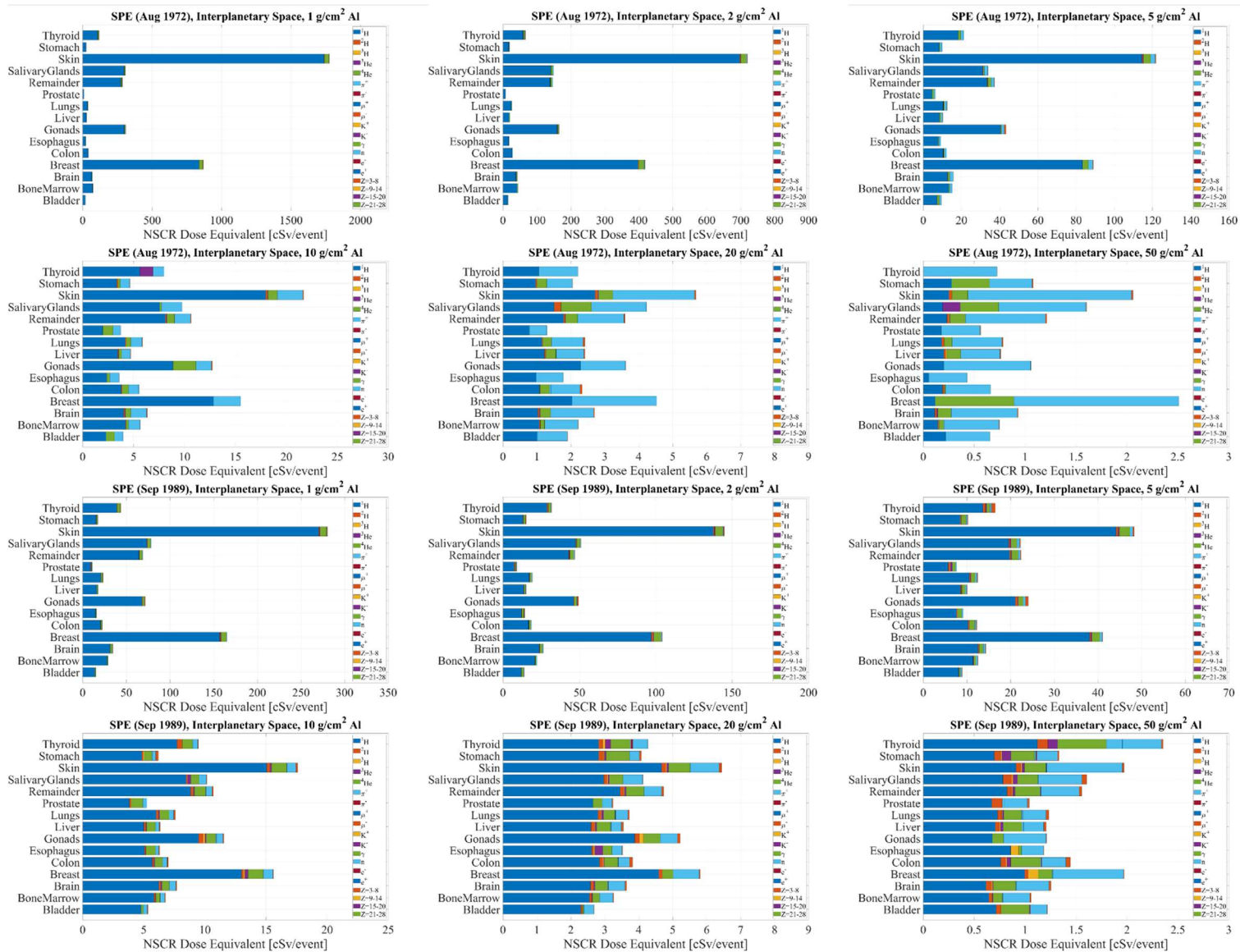
Figure 4.24. The NSCR dose equivalent in human organs during exposure to SPEs on August 4, 1972, and September 29, 1989, behind 1, 2, 5, 10, 20, and 50 g/cm^2 aluminum shielding in interplanetary space.
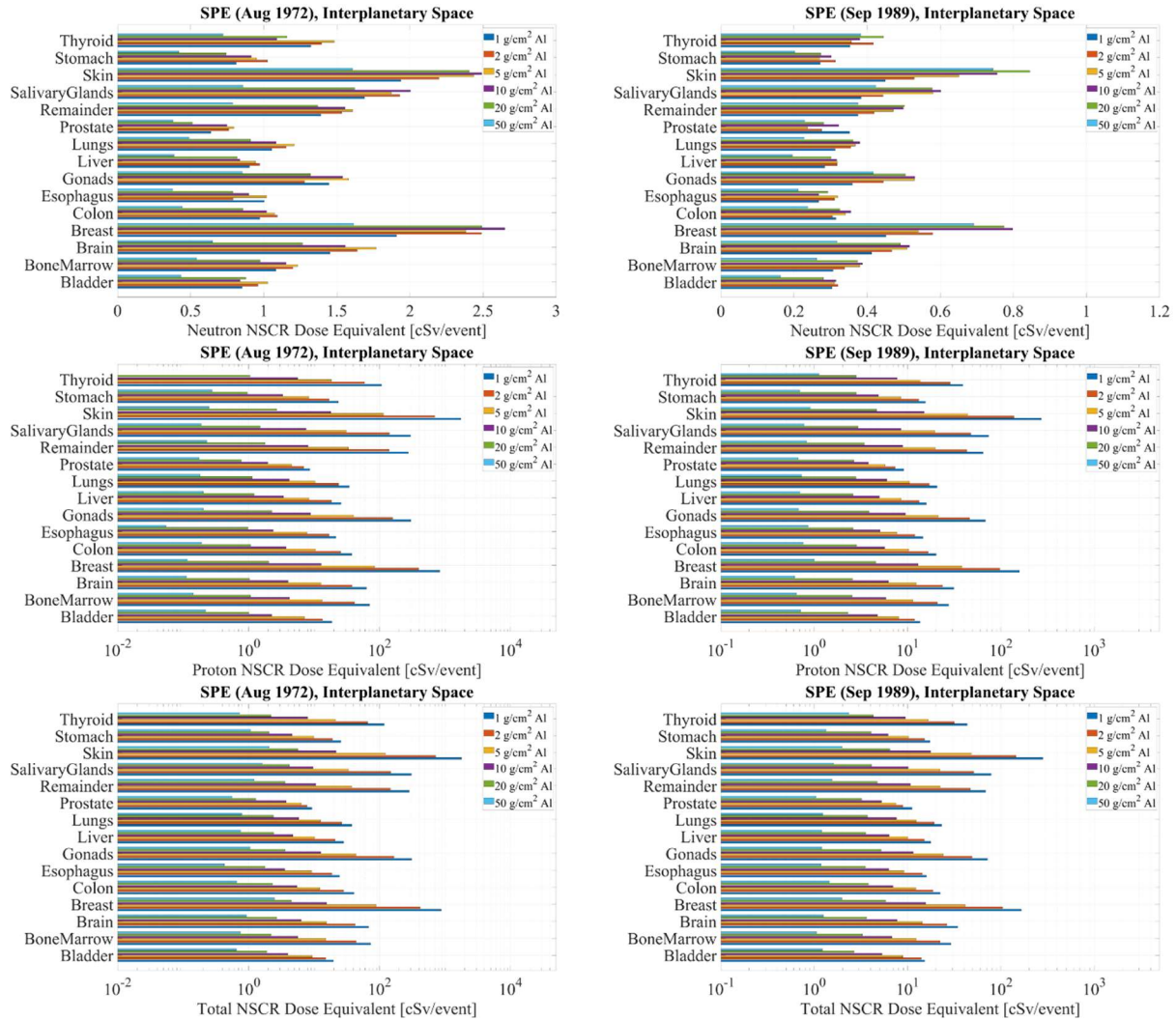
Figure 4.25. The NSCR dose equivalent of neutrons and protons and the total NSCR dose equivalent during exposure to SPEs on August 4, 1972, and September 29, 1989, behind 1, 2, 5, 10, 20, and 50 g/cm^2 aluminum shielding in interplanetary space.

The effective dose of neutrons and protons, along with the total effective dose assessed with the ICRP and NSCR models, is shown in Figure 4.26. The NSCR effective dose is generally lower than the ICRP effective dose, even though the NSCR dose equivalent is higher than the ICRP dose equivalent in most organs. This trend is attributed to the difference in ICRP and NSCR tissue weighting factors, as aforementioned for GCR exposure. Hence, the proton effective dose is higher with the NSCR model than with the ICRP model for 50 g/cm^2 aluminum, where the proton dose equivalent in breast is not significant, while the neutron and total dose equivalent is lower with the NSCR model. While proton and total effective dose decrease with aluminum shielding, as shown in Tables 4.2 and 4.3, the neutron effective dose is maximized behind 5 g/cm^2 and 10 g/cm^2 aluminum shielding for the 1972 SPE and the 1989 SPE, respectively, where the additional tissue shielding exists in the human body. At the same time, their contribution to the total effective dose drastically increases with the shielding amount. The total effective dose during exposure for the 1972 SPE behind 1 g/cm^2 aluminum shielding is 176 cSv and 93.6 cSv with the ICRP and NSCR models, respectively, significantly reducing to 2.77 cSv and 2.51 cSv behind typical (20 g/cm^2) aluminum shielding with each model. In the case of the 1989 SPE, 46.1 cSv and 31.8 cSv of the ICRP and NSCR effective dose decreases to 4.08 cSv and 3.81 cSv, respectively.

Table 4.2. The neutron (with % contribution to the total) and total effective doses during exposure to SPE on August 4, 1972, behind 1, 2, 5, 10, 20, and 50 g/cm^2 aluminum shielding in interplanetary space.

	Neutron Effective Dose [cSv/event]		Total Effective Dose [cSv/event]	
Shielding	ICRP	NSCR	ICRP	NSCR
1 g/cm^2 Al	1.20 (0.68%)	1.07 (1.14%)	176	93.6
2 g/cm^2 Al	1.35 (1.47%)	1.19 (2.32%)	92.2	51.4
5 g/cm^2 Al	1.39 (5.57%)	1.21 (7.32%)	24.9	16.6
10 g/cm^2 Al	1.34 (17.9%)	1.13 (18.1%)	7.51	6.23
20 g/cm^2 Al	1.19 (43.1%)	0.97 (38.8%)	2.77	2.51
50 g/cm^2 Al	0.70 (63.1%)	0.53 (61.4%)	1.10	0.86

Table 4.3. The neutron (with % contribution to the total) and total effective doses during exposure to SPE on September 29, 1989, behind 1, 2, 5, 10, 20, and 50 g/cm² aluminum shielding in interplanetary space.

	Neutron Effective Dose [cSv/event]		Total Effective Dose [cSv/event]	
Shielding	ICRP	NSCR	ICRP	NSCR
1 g/cm² Al	0.34 (0.73%)	0.32 (1.00%)	46.1	31.8
2 g/cm² Al	0.38 (1.18%)	0.35 (1.46%)	32.6	23.8
5 g/cm² Al	0.40 (2.40%)	0.37 (2.72%)	16.6	13.5
10 g/cm² Al	0.44 (5.21%)	0.38 (5.11%)	8.46	7.51
20 g/cm² Al	0.43 (10.5%)	0.37 (9.65%)	4.08	3.81
50 g/cm² Al	0.33 (23.0%)	0.26 (19.3%)	1.43	1.34
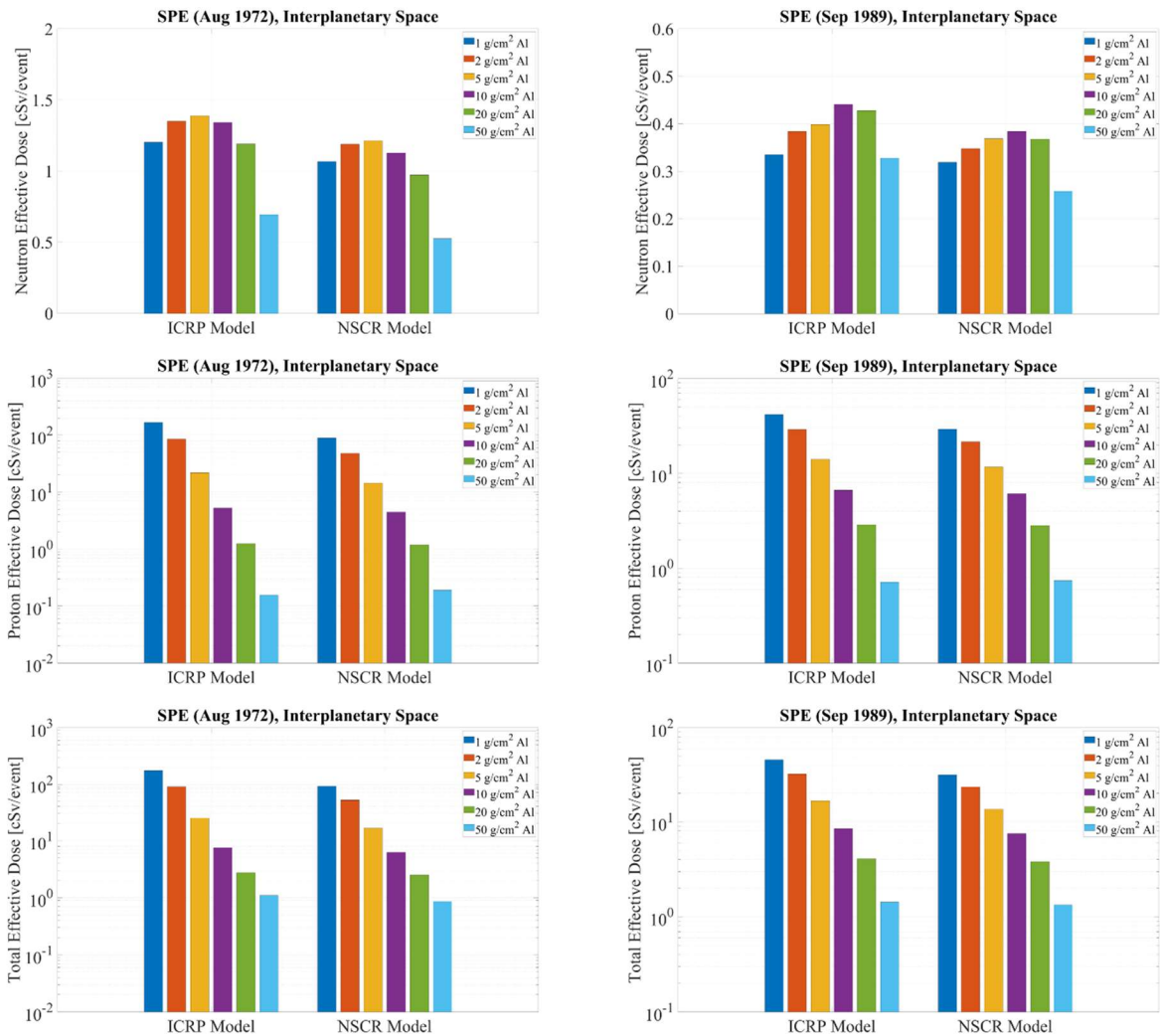
Figure 4.26. The effective dose of neutrons and protons and the total effective dose assessed with the ICRP and NSCR models during exposure to SPEs on August 4, 1972, and September 29, 1989, behind 1, 2, 5, 10, 20, and 50 g/cm² aluminum shielding in interplanetary space.

4.3: Tissue-specific Dose Quantities of Secondary Radiation on the Martian Surface

This chapter focuses on evaluating dose quantities on the surface of Mars, employing the ICRP male human phantom positioned within a hemispherical habitat with a 2-meter inner radius and varying aluminum shielding (1, 2, 5, 10, 20, and 50 g/cm^2). Utilizing the PHITS simulation codes with the JQMD-2.0 physics, particle energy spectra are recorded in human organs using the [T-Track] tally and subsequently converted to dose quantities.

For GCR, simulations involved the generation of 8×10^7, 4×10^7, 1×10^7, 5×10^6, 3×10^6, and 1×10^6 numbers of Z=1, Z=2, Z=3-8, Z=9-14, Z=15-20, and Z=21-28 ions, respectively, with the computation time ranging from 3 to 4 days. Conversely, SPE simulations for the events on August 4, 1972, and September 29, 1989, required 10 days for each exposure scenario, generating 2×10^8 to 3×10^8 initial protons. The findings indicate that the effective dose on the Martian surface for any considered SPE exposure cases is generally below 0.1 cSv regardless of shielding thickness, while the effective dose during GCR exposure ranges from 13.2 cSv to 17.0 cSv depending on shielding depth and assessment model. However, deriving meaningful tissue-specific dose quantities for SPE exposure proved challenging due to particle attenuation by the atmosphere, leading to statistically insufficient hits on human organs. Consequently, the tissue-specific dose quantities only for GCR exposure, recognized as the dominant source of radiation exposure on the Martian surface, are presented in this chapter.

Figure 4.27 and Figure 4.28 illustrate the tissue-specific absorbed dose during exposure to GCR near the solar minimum on the surface of Mars. Assuming the human phantom is in a standing position, a significantly higher dose equivalent is indicated in the head, including the brain and salivary glands, compared to the pelvic organs, including the prostate and gonads, since the atmosphere is thin at zenith and becomes thicker near ground.

Figure 4.27. The absorbed dose in human organs during annual exposure to GCR near the solar minimum behind 1, 2, 5, 10, 20, and 50 g/cm² aluminum shielding on the Martian surface.
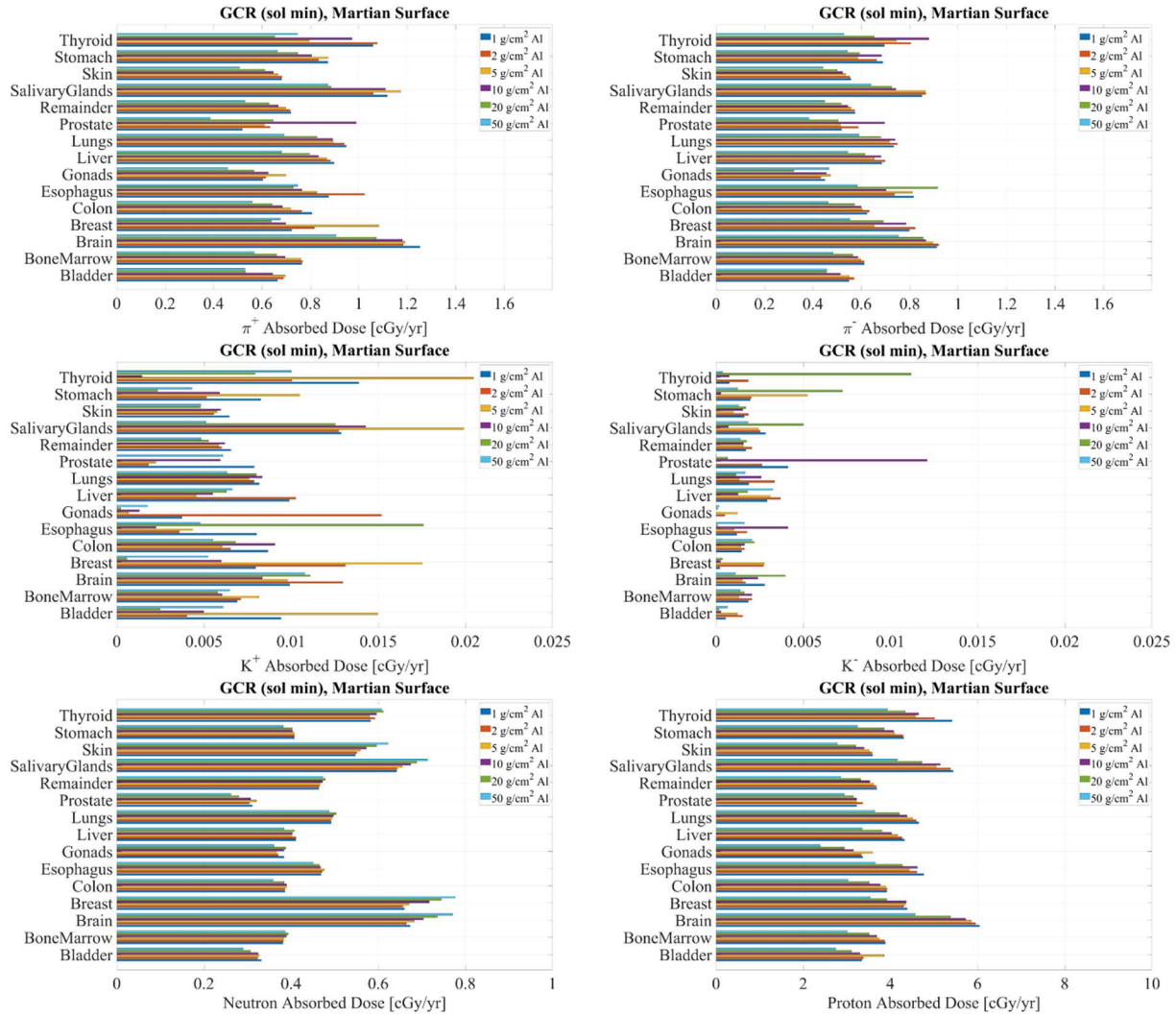
Figure 4.28. The absorbed dose of pions, kaons, neutrons, and protons in human organs during annual exposure to GCR near the solar minimum behind 1, 2, 5, 10, 20, and 50 g/cm² aluminum shielding on the Martian surface.

In contrast to interplanetary space, the absorbed dose of secondary mesons tends to decrease with increased aluminum shielding, while the kaon dose exhibits substantial variation and statistical instability. This phenomenon is attributed to the significant attenuation of primary GCR ions in the additional heavy shielding of the atmosphere, as evidenced by the decreased proton and total dose with increased shielding. The tendency of neutron dose depends on the type of organs or tissue shielding. Organs with less tissue shielding, such as the brain, breast, salivary glands, and skin, show an increase in neutron dose along with aluminum shielding depth, akin to interplanetary space. However, for organs with more tissue shielding, such as the bladder and prostate, the neutron dose decreases with increased aluminum shielding, resembling other particles on the Martian surface. This is possibly due to the attenuation of low-energy neutrons in tissues – hydrogen-rich material – effective in neutron shielding. This phenomenon leads to less variation of the neutron absorbed dose from organ to organ for thin aluminum shielding compared to thick aluminum shielding.

Figure 4.29 and Figure 4.30 depict the tissue-specific energy spectra of protons and secondary pions, kaons, and neutrons for annual GCR exposure behind 5 and 20 g/cm^2 aluminum shielding, respectively. A higher flux of protons and pions is shown with less shielding, such as in the brain or salivary glands behind 5 g/cm^2 aluminum, while increased statistical instability for kaons is indicated. Contrasted with typical (20 g/cm^2) aluminum shielding, the low-energy neutron fluxes in various organs are closer to each other behind thin (5 g/cm^2) aluminum shielding, as suggested by the neutron absorbed dose.
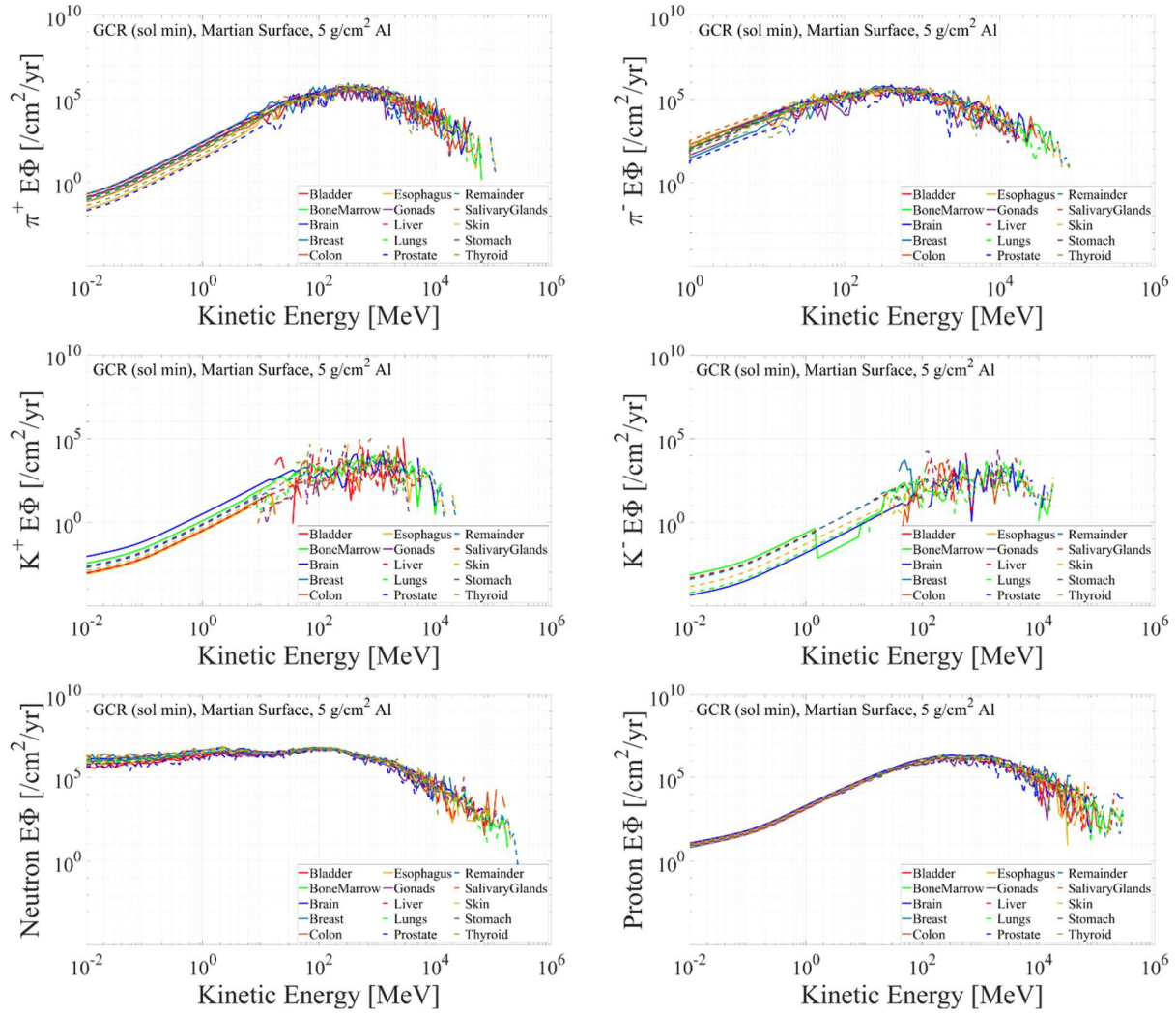
Figure 4.29. The energy (lethargy) spectra of pions, kaons, neutrons, and protons in human organs during annual exposure to GCR near the solar minimum behind 5 g/cm^2 aluminum shielding on the Martian surface.
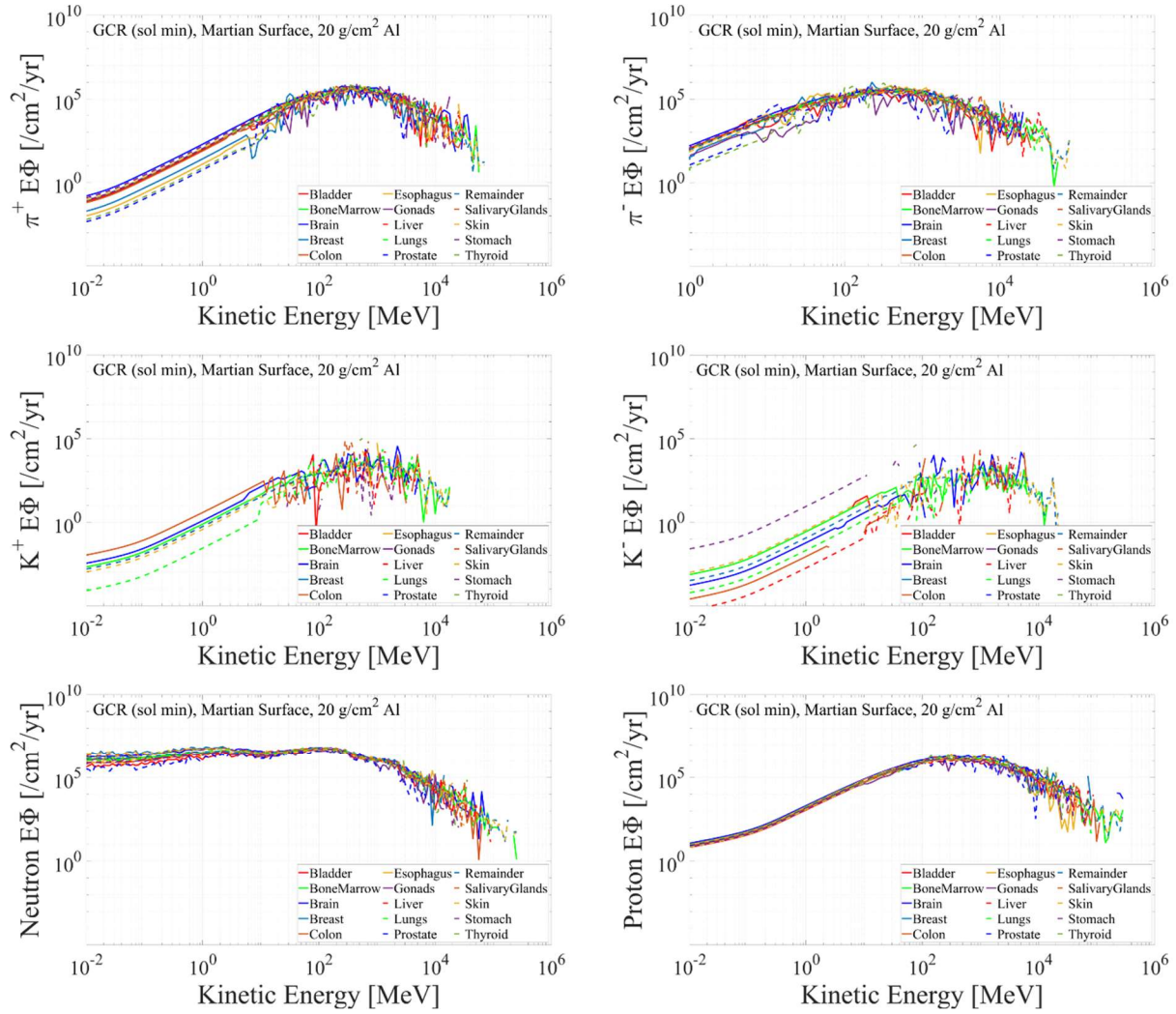
Figure 4.30. The energy (lethargy) spectra of pions, kaons, neutrons, and protons in human organs during annual exposure to GCR near the solar minimum behind 20 g/cm^2 aluminum shielding on the Martian surface.

The dose equivalent estimated with the ICRP model is shown in Figure 4.31 and Figure 4.32. Because primary GCR heavy ions are mostly attenuated in the atmosphere, their contribution to the total dose equivalent is minimal, while light ions, pions, and neutrons play a major role. The total dose equivalent predominantly varies with the total absorbed dose rather than relying heavily on heavy ion contribution. In annual GCR exposure scenarios considered, tissue-specific dose equivalent on the Martian surface ranges from 9.81 cSv in organs behind thick shielding, such as gonads behind 50 g/cm^2 aluminum, to 23.5 cSv in organs behind thin shielding, like the brain behind 1 g/cm^2 aluminum. Compared to interplanetary space, the variation of secondary meson and neutron dose equivalents for different aluminum shielding depths is suggested to be reduced due to the attenuation of primary GCR ions, which can generate secondaries.

Figure 4.33 and Figure 4.34 introduce the dose equivalent evaluated with the NSCR model. While the total NSCR dose equivalent is much smaller than the total ICRP dose equivalent behind thin shielding in interplanetary space, there is no significant difference in NSCR and ICRP dose equivalents on the Martian surface, except for bone marrow, which uses the parameters for leukemia. This is attributed to the lack of heavy ions, which have a higher ICRP quality factor compared to the NSCR model, while protons with a slightly higher NSCR quality factor dominate the dose equivalent. Consequently, the decrease in heavy ion dose equivalent and the increase in proton dose equivalent result in similar total dose equivalents with both models.
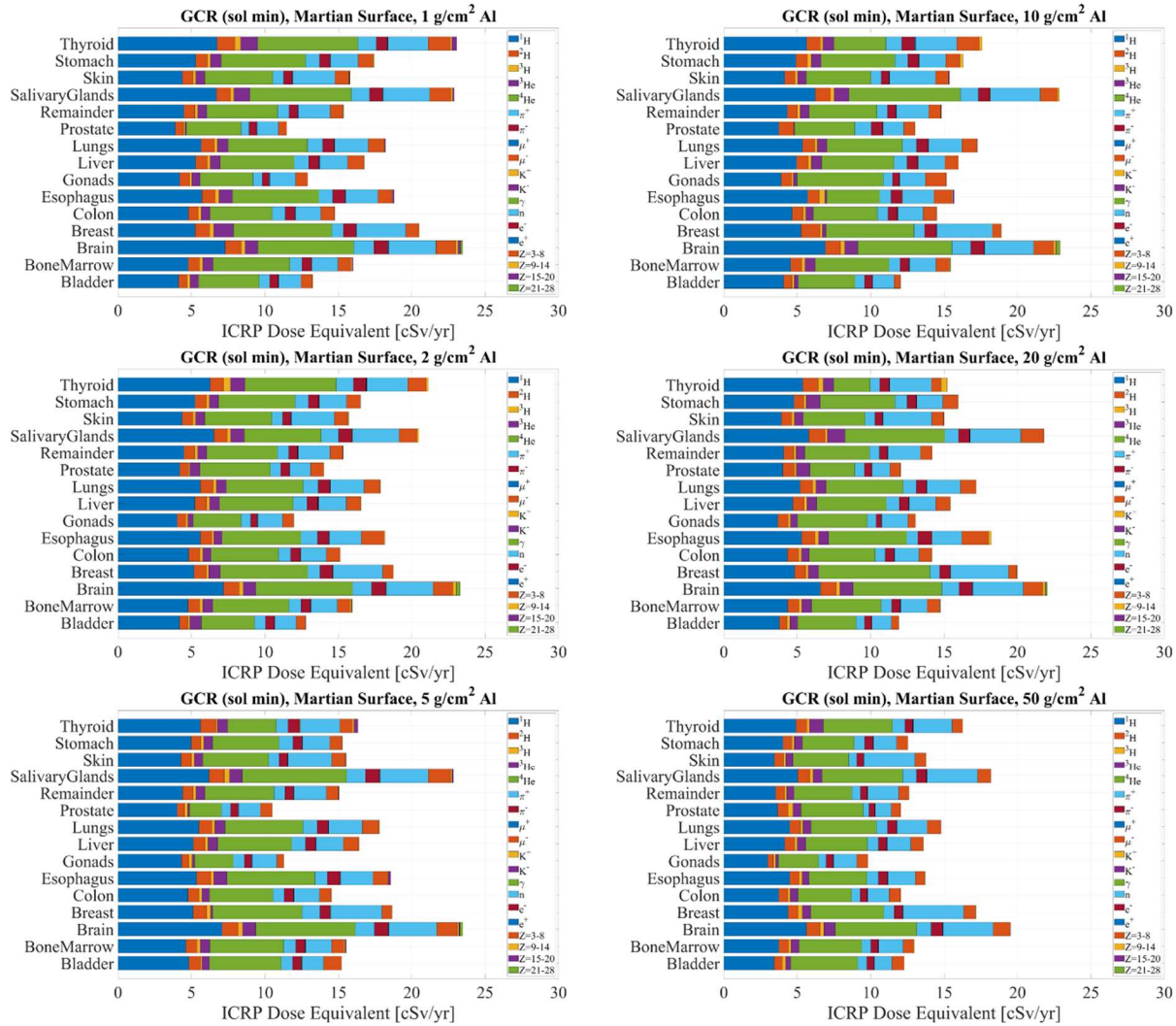
Figure 4.31. The ICRP dose equivalent in human organs during annual exposure to GCR near the solar minimum behind 1, 2, 5, 10, 20, and 50 g/cm^2 aluminum shielding on the Martian surface.
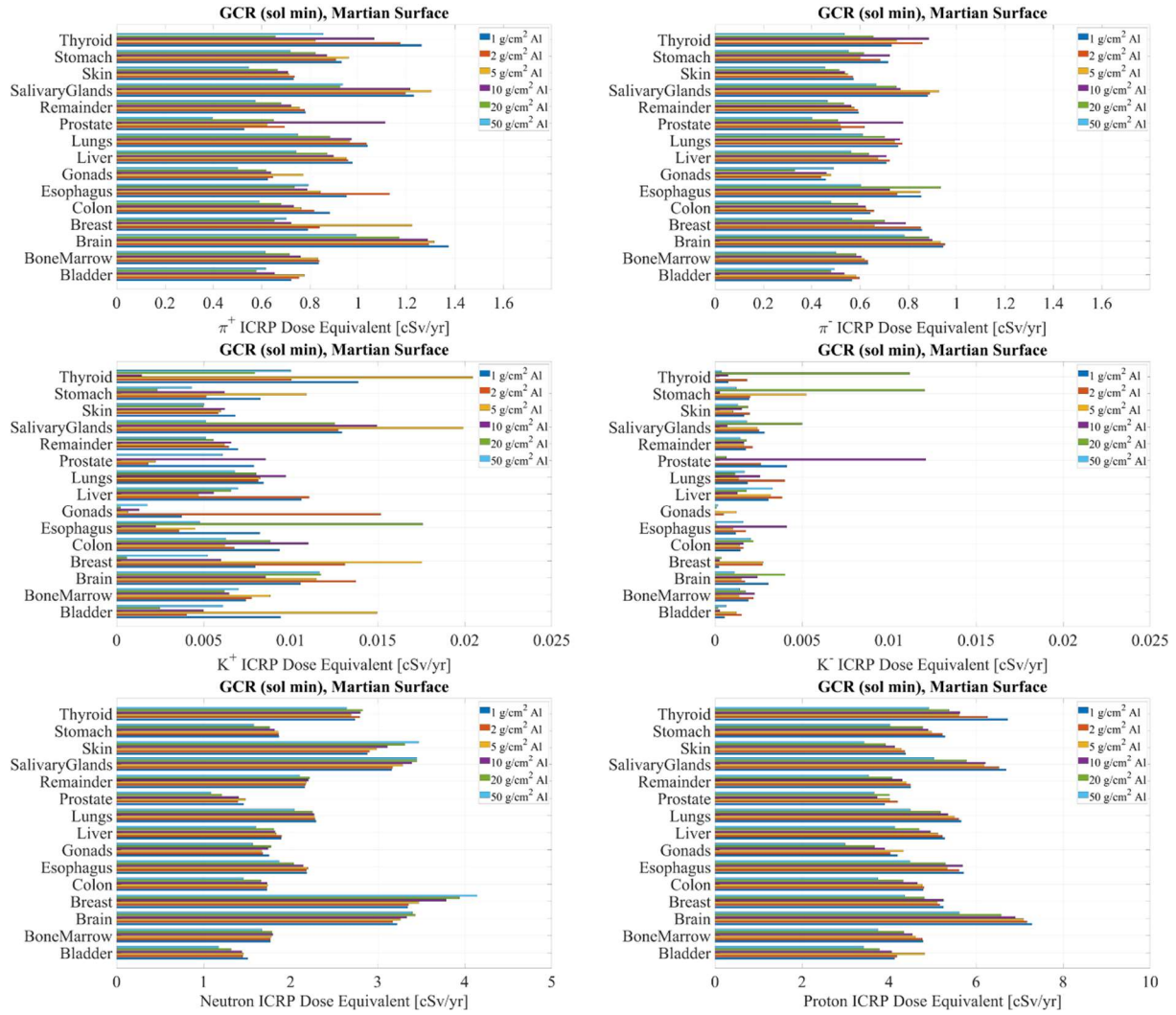
Figure 4.32. The ICRP dose equivalent of pions, kaons, neutrons, and protons in human organs during annual exposure to GCR near the solar minimum behind 1, 2, 5, 10, 20, and 50 g/cm^2 aluminum shielding on the Martian surface.

125
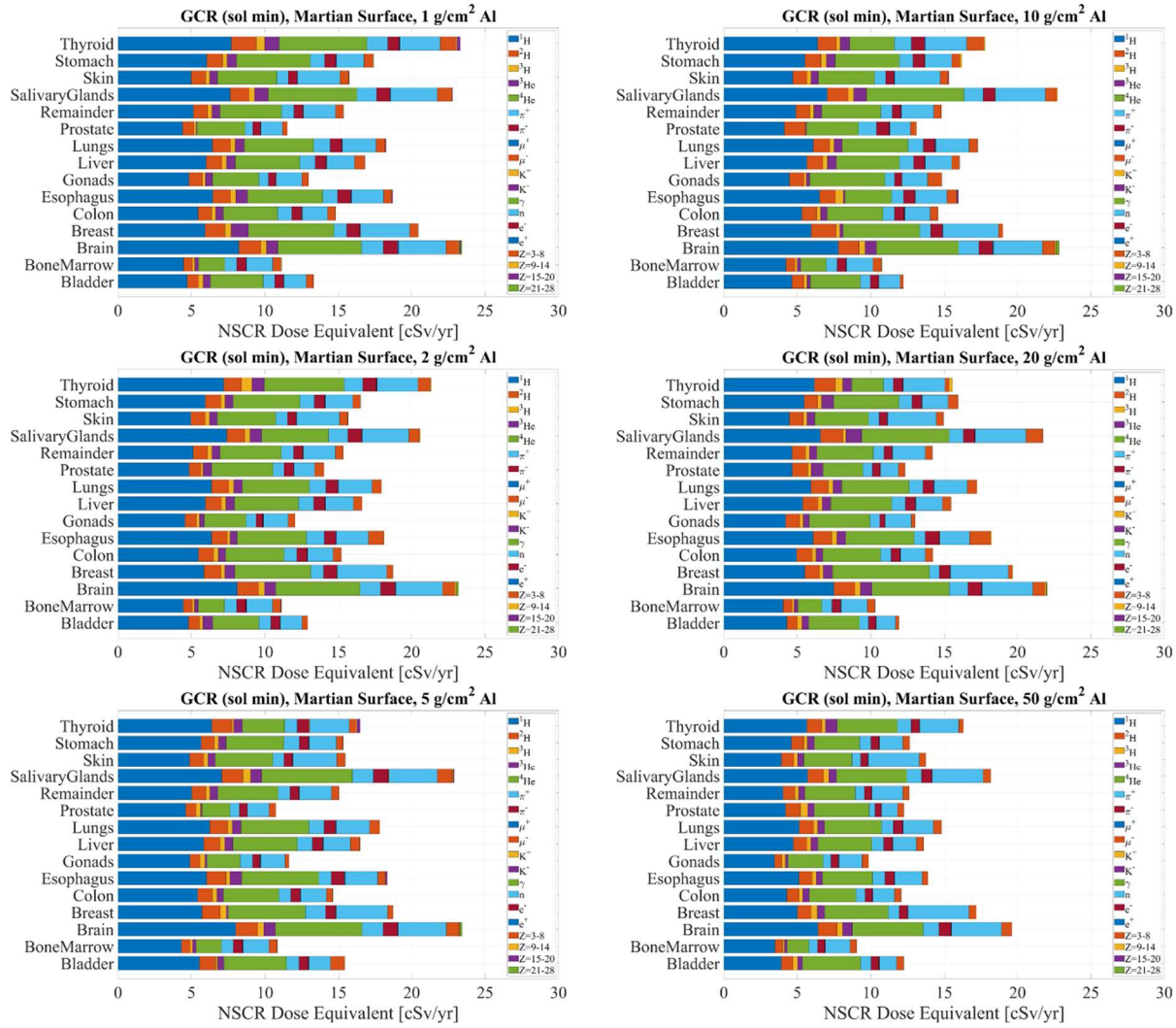
Figure 4.33. The NSCR dose equivalent in human organs during annual exposure to GCR near the solar minimum behind 1, 2, 5, 10, 20, and 50 g/cm^2 aluminum shielding on the Martian surface.
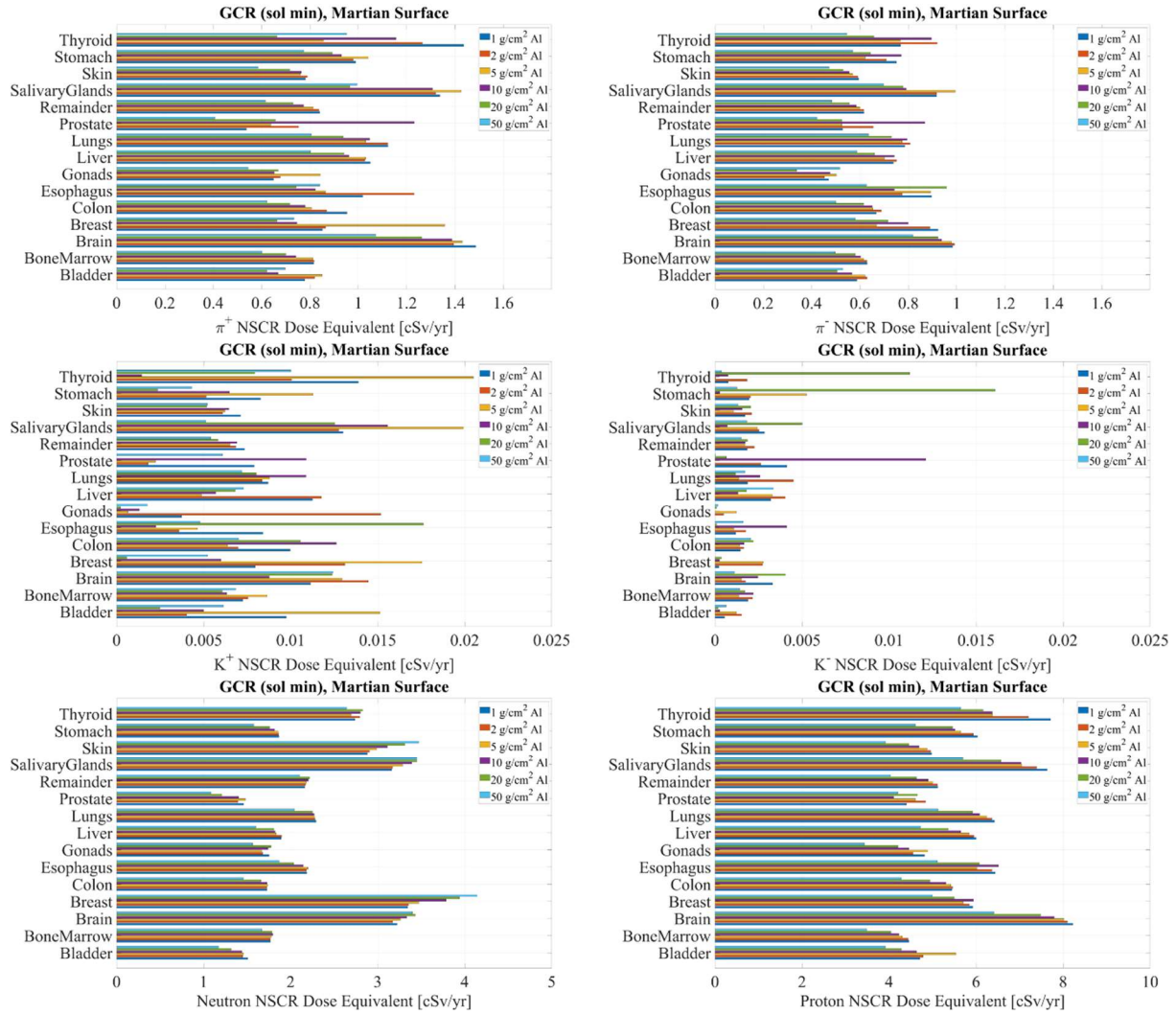
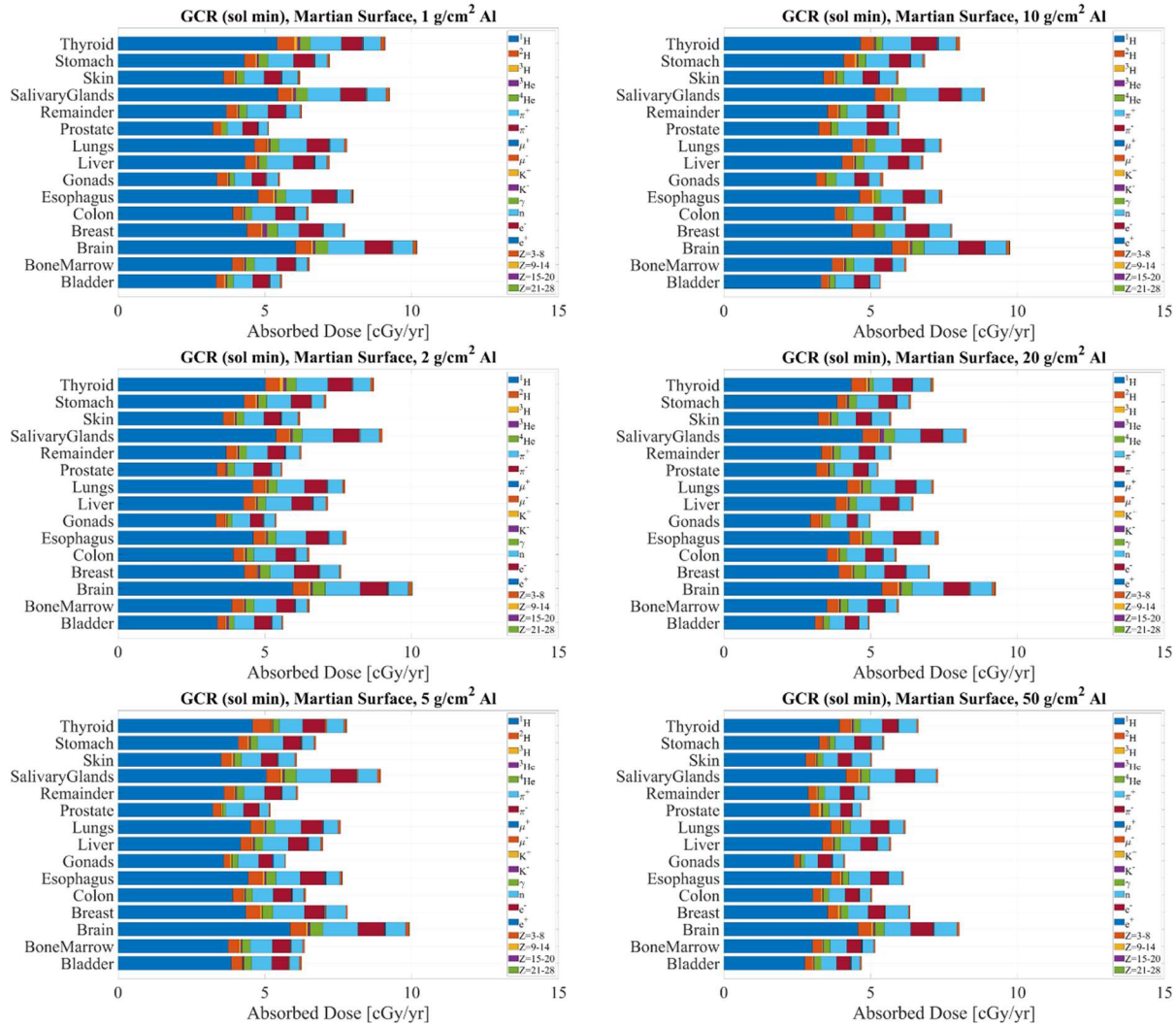Figure 4.34. The ICRP dose equivalent of pions, kaons, neutrons, and protons in human organs during annual exposure to GCR near the solar minimum behind 1, 2, 5, 10, 20, and 50 g/cm^2 aluminum shielding on the Martian surface.

The total effective dose and pion, kaon, neutron, and proton effective doses assessed with the ICRP and NSCR models are shown in Figure 4.35. Unlike the increased meson, neutron, and proton effective doses along the shielding depth in interplanetary space, they tend to decrease with shielding on the surface of Mars, while the trend in kaon effective dose is not clear due to statistical instability. Additionally, the tendency of the positive pion ICRP effective dose is vague, while a clear decrease is shown with the NSCR model. The neutron effective dose is less dependent on the aluminum shielding amount until 20 g/cm^2 because the neutron dose equivalent decreases in organs with more tissue shielding and increases in organs with less tissue shielding. The total effective dose is suggested to be slightly reduced from 17.0 cSv and 16.4 cSv behind 1 g/cm^2 aluminum with the ICRP and NSCR models, respectively, to 15.7 cSv and 15.3 cSv behind the typical (20 g/cm^2) aluminum shielding with each model. Further decreases to 13.5 cSv and 13.2 cSv are plausible with thicker (50 g/cm^2) aluminum shielding. As shown in Table 4.4, the sum of the effective doses of neutrons, pions, and kaons gradually decreases with aluminum shielding, while their contribution to the total effective dose tends to increase slightly but is less dependent on shielding compared to interplanetary space.

Table 4.4. The sum of the effective doses of neutrons, pions, and kaons (with % contribution to the total) and the total effective dose during annual exposure to GCR near the solar minimum behind 1, 2, 5, 10, 20, and 50 g/cm^2 aluminum shielding on the Martian surface.

	Neutron + Pion + Kaon Effective Dose [cSv/yr]		Total Effective Dose [cSv/yr]	
Shielding	ICRP	NSCR	ICRP	NSCR
1 g/cm^2 Al	3.73 (22.0%)	3.79 (23.1%)	17.0	16.4
2 g/cm^2 Al	3.72 (22.7%)	3.78 (23.4%)	16.4	16.2
5 g/cm^2 Al	3.71 (23.3%)	3.71 (23.4%)	16.0	15.9
10 g/cm^2 Al	3.68 (22.9%)	3.70 (23.7%)	16.1	15.6
20 g/cm^2 Al	3.55 (22.6%)	3.52 (23.1%)	15.7	15.3
50 g/cm^2 Al	3.29 (24.4%)	3.17 (24.0%)	13.5	13.2
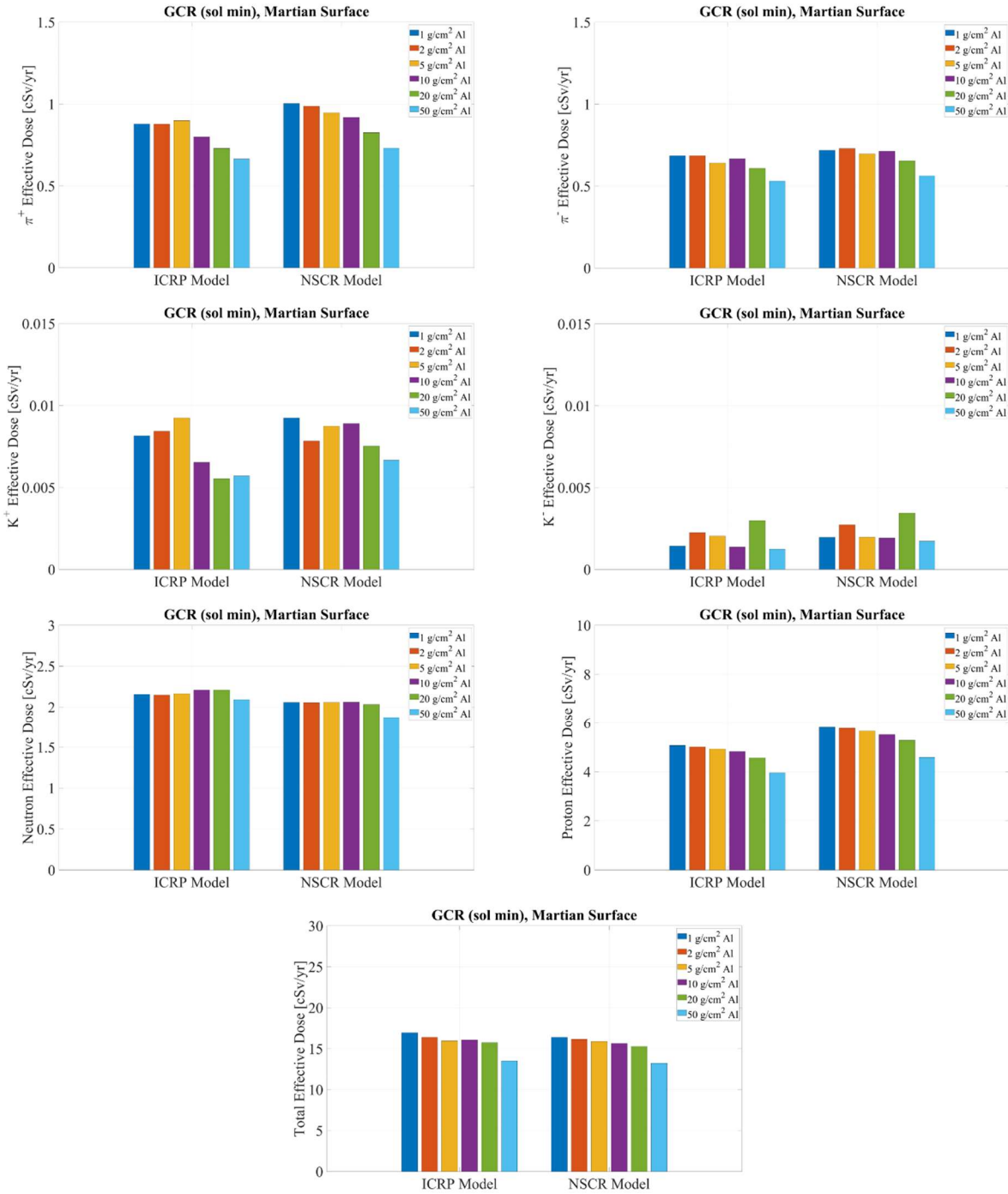
Figure 4.35. The effective dose of pions, kaons, neutrons, and protons, and the total effective dose assessed with the ICRP and NSCR models for annual exposure to GCR near the solar minimum behind 1, 2, 5, 10, 20, and 50 g/cm² aluminum shielding on the Martian surface.

Chapter 5: Conclusion

The present project undertakes an assessment of the absorbed dose, dose equivalent, and effective dose of secondary particles for Mars exploration. While prior studies have investigated the dose equivalent of HZE particles (Naito & Kodaira, 2022) and absorbed dose of pions (Aghara et al., 2009; Slaba et al., 2013) for deep space and LEO, this project represents the inaugural endeavor to furnish detailed information regarding tissue-specific dosimetric quantities for Mars exploration, encompassing various secondary particles within a realistic human voxel phantom for males. Diverging from previous research, which predominantly relied on the ICRP model (developed for ground-based exposures) for dose equivalent assessment (Sato et al., 2011), this work offers a comprehensive analysis between the ICRP and NSCR models, alongside furnishing tissue-specific particle energy spectra for protons and major secondary particles.

The findings of this project demonstrate a commendable alignment between the assessed dose equivalent and measurements. In the interplanetary space scenario, the total dose equivalent in the skin, where tissue shielding is minimal, behind 5 g/cm^2 aluminum shielding, is estimated to be 65.9 cSv/yr using the quality factors delineated in ICRP Publication 60. This approximation closely corresponds to the measured value of 67.2 ± 12.1 cSv/yr obtained from the Mars Science Laboratory Radiation Assessment Detector (MSL/RAD) during the cruise phase, which entailed an average of approximately 8 g/cm^2 aluminum-equivalent shielding without tissues (Zeitlin et al., 2013). Similarly, the anticipated dose equivalent for the brain behind identical shielding on the Martian surface is projected to be 23.5 cSv/yr, a figure akin to the measured value of 23.4 ± 4.38 cSv/yr recorded by MSL/RAD on the Martian surface (Hassler et al., 2014).

The results of this study suggest that secondary pions pose significant health risks in the context of GCR exposure, while they are of lesser concern for SPE exposure due to the diminished

intensity of high-energy particles capable of engendering pions, which have a production threshold of approximately 290 MeV. Conversely, a notable surge in secondary neutron contributions to dosimetric quantities is observed with increasing aluminum shielding depth in the context of SPE exposure, particularly during events such as the one in August 1972 characterized by substantial flux of low-energy protons. However, this phenomenon is attributed not to an escalation in neutron dose but rather to a significant decrease in proton dose, suggesting that augmenting shielding depth reduces dosimetric quantities of SPE protons effectively while mitigating secondary neutrons yields a considerable reduction in total dosimetric quantities during exposure to large SPEs.

The escalation in secondary neutrons and mesons remains a prominent concern for GCR exposure. The proliferation of neutrons and charged pions in interplanetary space and on the Martian surface leads to dense energy deposition within a small tissue volume by producing high-LET target fragments, precipitating heightened DNA DSBs, chromosome aberrations, and cellular lethality.

Although devising countermeasures against secondary particles for Mars exploration poses challenges, primarily owing to their increased fluxes behind heavier shielding, the adoption of low-Z materials as shielding holds promise due to their diminished production cross-sections for neutrons and pions, thereby curbing secondary generation and mitigating dosimetric quantities.

Limitations inherent in this project include statistical instability in results and constraints associated with the selected physics models. While statistical uncertainties in dosimetric quantities for GCR exposure in interplanetary space are predominantly less than 1%, they range from less than 5% to over 10% across the organ types on the Martian surface due to the reduced number of particles reaching human organs owing to significant attenuation in the Martian atmosphere. For SPEs featuring a substantial flux of low-energy protons, statistical errors generally remain below 3% with thin (1 g/cm^2 aluminum) shielding, while they span between 6 and 15% with thick (50

g/cm^2 aluminum) shielding. Furthermore, the EPDL97 (Cullen et al., 1997) has been adopted instead of the newer EGS5 algorithm (Hirayama et al., 2005) for electron, positron, and photon transport, as the latter entails computation times over five times longer, which might result in slightly reduced total dosimetric quantities due to potential underestimation of electron and positron dosimetric quantities.

Future works should prioritize reducing uncertainties associated with the assessment of dosimetric quantities and enhancing computing power to facilitate the application of more intricate and realistic physics models. Similar calculations using a female phantom model should also be investigated. Additionally, employing the EGM for neutron transport, coupled with the adoption of the EGS5 algorithm for secondary electron and positron transport, promises deeper insights into exposure to secondary neutrons by furnishing data on neutron-induced fragments. However, leveraging EGS5 and EGM for human phantom simulations necessitates advanced computing technologies and resources. Beyond these considerations, exploring diverse materials viable for radiation shielding in space exploration is imperative to mitigate the impact of secondary particles on human crews. Given that roughly 10% to 40% of the effective dose for Mars exploration is attributed to secondary mesons and neutrons, substantial strides in safeguarding human crews are anticipated through measures aimed at reducing secondary particle generation.

Bibliography

Adriani, O., Barbarino, G. C., Bazilevskaya, G. A., Bellotti, R., Boezio, M., Bogomolov, E. A., ... & Zverev, V. G. (2014). The PAMELA Mission: Heralding a new era in precision cosmic ray physics. *Physics Reports*, *544*(4), 323-370.

Aghara, S. K., Blattnig, S. R., Norbury, J. W., & Singleterry, R. C. (2009). Monte Carlo analysis of pion contribution to absorbed dose from galactic cosmic rays. *Nuclear Instruments and Methods in Physics Research Section B: Beam Interactions with Materials and Atoms*, *267*(7), 1115-1124.

Agostinelli, S., Allison, J., Amako, K. A., Apostolakis, J., Araujo, H., Arce, P., ... & Geant4 Collaboration. (2003). GEANT4—a simulation toolkit. *Nuclear instruments and methods in physics research section A: Accelerators, Spectrometers, Detectors and Associated Equipment*, *506*(3), 250-303.

Ainsworth, E. J., Fry, R. J., Grahn, D., Williamson, F. S., Brennan, P. C., Stearner, S. P., ... & Rust, J. H. (1973). *Late effects of neutron or gamma irradiation in mice*. Argonne National Lab., IL.

Allison, J., Amako, K., Apostolakis, J. E. A., Araujo, H. A. A. H., Dubois, P. A., Asai, M. A. A. M., ... & Yoshida, H. A. Y. H. (2006). Geant4 developments and applications. *IEEE Transactions on nuclear science*, *53*(1), 270-278.

Allison, J., Amako, K., Apostolakis, J., Arce, P., Asai, M., Aso, T., ... & Yoshida, H. (2016). Recent developments in Geant4. *Nuclear instruments and methods in physics research section A: Accelerators, Spectrometers, Detectors and Associated Equipment*, *835*, 186-225.

Al Zaman, M. A., & Kunja, L. A. (2023). Effectiveness of radiation shields constructed from Martian regolith and different polymers for human habitat on Mars using MULASSIS/GEANT4 and OLTARIS. *AIP Advances*, *13*(8).

Amian, W. B., Byrd, R. C., Goulding, C. A., Meier, M. M., Morgan, G. L., Moss, C. E., & Clark, D. A. (1992). Differential neutron production cross sections for 800-MeV protons. *Nuclear science and engineering*, *112*(1), 78-86.

Armstrong, T. W., & Chandler, K. C. (1973). *SPAR, a FORTRAN program for computing stopping powers and ranges for muons, charged pions, protons, and heavy ions* (No. ORNL-4869). Oak Ridge National Lab., TN, USA.

Attix, F. H. (2008). *Introduction to radiological physics and radiation dosimetry*. John Wiley & Sons.

Badhwar, G. D., & O'Neill, P. M. (1994). Long-term modulation of galactic cosmic radiation and its model for space exploration. *Advances in Space Research*, *14*(10), 749-757.

Baker, D. N. (1998). What is space weather?. *Advances in Space Research*, *22*(1), 7-16.

Baker, D. N. (2002). How to cope with space weather. *Science*, *297*(5586), 1486-1487.

Band, D., Matteson, J., Ford, L., Schaefer, B., Palmer, D., Teegarden, B., ... & Lestrade, P. (1993). BATSE observations of gamma-ray burst spectra. I-Spectral diversity. *Astrophysical Journal, Part 1 (ISSN 0004-637X), vol. 413, no. 1, p. 281-292.*, *413*, 281-292.

Barkas, W. H. (1953). The range correction for electron pick-up. *Physical Review*, *89*(5), 1019.

Battistoni, G., Boehlen, T., Cerutti, F., Chin, P. W., Esposito, L. S., Fassò, A., ... & Smirnov, G. (2015). Overview of the FLUKA code. *Annals of Nuclear Energy*, *82*, 10-18.

Battistoni, G., Bauer, J., Boehlen, T. T., Cerutti, F., Chin, M. P., Dos Santos Augusto, R., ... & Vlachoudis, V. (2016). The FLUKA code: an accurate simulation tool for particle therapy. *Frontiers in oncology*, *6*, 116.

Belkic, D. (2012). *Theory of heavy ion collision physics in hadron therapy*. Academic Press.

Bell, J. S., & Squires, E. J. (1959). A formal optical model. *Physical Review Letters*, *3*(2), 96.

Bernal, M. A., Bordage, M. C., Brown, J. M. C., Davídková, M., Delage, E., El Bitar, Z., ... & Incerti, S. (2015). Track structure modeling in liquid water: A review of the Geant4-DNA very low energy extension of the Geant4 Monte Carlo simulation toolkit. *Physica Medica*, *31*(8), 861-874.

Bielajew, A. F. (2001). Fundamentals of the Monte Carlo method for neutral and charged particle transport. The University of Michigan. *Ann Arbor*, *178*.

Billings, M. P., & Yucker, W. R. (1973). Summary final report. The computerized anatomical man (CAM) model. *Report*, *1600*, G4655.

Bizzarri, M., Monici, M., & van Loon, J. J. (2015). How microgravity affects the biology of living systems. *BioMed research international*, *2015*.

Bolst, D., Cirrone, G. A., Cuttone, G., Folger, G., Incerti, S., Ivanchenko, V., ... & Guatelli, S. (2017). Validation of Geant4 fragmentation for heavy ion therapy. *Nuclear Instruments and Methods in Physics Research Section A: Accelerators, Spectrometers, Detectors and Associated Equipment*, *869*, 68-75.

Boudard, A., Cugnon, J., David, J. C., Leray, S., & Mancusi, D. (2013). New potentialities of the Liège intranuclear cascade model for reactions induced by nucleons and light charged particles. *Physical Review C*, *87*(1), 014606.

Bradbury, P., Wu, H., Choi, J. U., Rowan, A. E., Zhang, H., Poole, K., ... & Chou, J. (2020). Modeling the Impact of Microgravity at the Cellular Level: Implications for Human Disease. *Frontiers in Cell and Developmental Biology*, *8*, 96.

Bradt, H. L., & Peters, B. (1950). The heavy nuclei of the primary cosmic radiation. *Physical Review*, *77*(1), 54.

Bruno, A., Bazilevskaya, G. A., Boezio, M., Christian, E. R., De Nolfo, G. A., Martucci, M., ... & Zampa, N. (2018). Solar energetic particle events observed by the PAMELA mission. *The Astrophysical Journal*, *862*(2), 97.

Butts, J., & Katz, R. (1967). Theory of RBE for heavy ion bombardment of dry enzymes and viruses. *Radiation research*, *30*(4), 855-871.

Chancellor, J. C., Scott, G. B., & Sutton, J. P. (2014). Space radiation: the number one risk to astronaut health beyond low earth orbit. *Life*, *4*(3), 491-510.

Chiba, G., Okumura, K., Sugino, K., Nagaya, Y., Yokoyama, K., Kugo, T., ... & Okajima, S. (2011). JENDL-4.0 benchmarking for fission reactor applications. *Journal of nuclear science and technology*, *48*(2), 172-187.

Coleman, W. A., & Armstrong, T. W. (1970). *NUCLEON--MESON TRANSPORT CODE NMTC* (No. ORNL-4606). Oak Ridge National Lab., Tenn..

Cristy, M. (1980). *Mathematical phantoms representing children of various ages for use in estimates of internal dose* (No. NUREG/CR-1159; ORNL/NUREG/TM-367). Oak Ridge National Lab., TN, USA.

Cristy, M., & Eckerman, K. F. (1987). *Specific absorbed fractions of energy at various ages from internal photon sources* (No. ORNL/TM-8381/VI).

Cucinotta, F. A., Khandelwal, G. S., Townsend, L. W., & Wilson, J. W. (1989). Correlations in α-α scattering and semi-classical optical models. *Physics Letters B*, *223*(2), 127-132.

Cucinotta, F. A. (1994a). *Multiple-scattering model for inclusive proton production in heavy ion collisions* (No. NAS 1.60: 3470).

Cucinotta, F. A., Townsend, L. W., Wilson, J. W., Golightly, M. J., & Weyland, M. (1994b). Analysis of radiation risk from alpha particle component of solar particle events. *Advances in Space Research*, *14*(10), 661-670.

Cucinotta, F. A., Wilson, J. W., & Badavi, F. F. (1994c). *Extension of the BRYNTRN code to monoenergetic light ion beams* (No. L-17394).

Cucinotta, F. A., & Wilson, J. W. (1996). *Study of Analytic Statistical Model for Decay of Light and Medium Mass Nuclei in Nuclear Fragmentation* (No. NAS 1.60: 3594).

Francis A, C., John W, W., & John W, N. (1998). Parameterizations of Pion Energy Spectrum in Nucleon-Nucleon Collisions. NASA/TM-1998-208722.

Cucinotta, F. A., Wilson, J. W., Tripathi, R. K., & Townsend, L. W. (1998b). Microscopic fragmentation model for galactic cosmic ray studies. *Advances in Space Research*, *22*(4), 533-537.

Cucinotta, F. A., Schimmerling, W., Wilson, J. W., Peterson, L. E., Badhwar, G. D., Saganti, P. B., & Dicello, J. F. (2001). Space radiation cancer risks and uncertainties for Mars missions. *Radiation research*, *156*(5), 682-688.

Cucinotta, F. A., & Durante, M. (2006a). Cancer risk from exposure to galactic cosmic rays: implications for space exploration by human beings. *The lancet oncology*, *7*(5), 431-435.

Cucinotta, F. A., Kim, M. H. Y., & Ren, L. (2006b). Evaluating shielding effectiveness for reducing space radiation cancer risks. *Radiation Measurements*, *41*(9-10), 1173-1185.

Cucinotta, F. A., Wilson, J. W., Saganti, P., Hu, X., Kim, M. H. Y., Cleghorn, T., ... & Tripathi, R. K. (2006c). Isotopic dependence of GCR fluence behind shielding. *Radiation Measurements*, *41*(9-10), 1235-1249.

Cucinotta, F. A., Kim, M. H. Y., Willingham, V., & George, K. A. (2008). Physical and biological organ dosimetry analysis for international space station astronauts. *Radiation research*, *170*(1), 127-138.

Cucinotta, F. A., & Durante, M. (2009). Risk of radiation carcinogenesis. *Human health and performance risks of space exploration missions. NASA SP-2009-3405. Houston: National Aeronautics and Space Administration*, 119-170.

Cucinotta, F. A., Hu, S., Schwadron, N. A., Kozarev, K., Townsend, L. W., & Kim, M. H. Y. (2010). Space radiation risk limits and Earth-Moon-Mars environmental models. *Space Weather*, *8*(12).

Cucinotta, F. A., Plante, I., Ponomarev, A. L., & Kim, M. H. Y. (2011a). Nuclear interactions in heavy ion transport and event-based risk models. *Radiation protection dosimetry*, *143*(2-4), 384-390.

Cucinotta, F. A., Kim, M. H. Y., & Chappell, L. J. (2011b). *Space radiation cancer risk projections and uncertainties-2010* (No. S-1102).

Cucinotta, F. A., Kim, M. H. Y., & Chappell, L. J. (2012). Evaluating shielding approaches to reduce space radiation cancer risks. *NASA Technical Memorandum*, *217361*.

Cucinotta, F. A., Kim, M. H. Y., & Chappell, L. J. (2013a). Space radiation cancer risk projections and uncertainties-2012. NASA/TP-2013-217375.

Cucinotta, F. A., Kim, M. H. Y., Chappell, L. J., & Huff, J. L. (2013b). How safe is safe enough? Radiation risk for a human mission to Mars. *PloS one*, *8*(10), e74988.

Cucinotta, F. A., To, K., & Cacao, E. (2017). Predictions of space radiation fatality risk for exploration missions. *Life sciences in space research*, *13*, 1-11.

Cucinotta, F. A., Yan, C., & Saganti, P. B. (2018). 2nd-order optical model of the isotopic dependence of heavy ion absorption cross sections for radiation transport studies. *Nuclear Instruments and Methods in Physics Research Section B: Beam Interactions with Materials and Atoms*, *414*, 11-17.

Cucinotta, F. A., Cacao, E., Kim, M. H. Y., & Saganti, P. B. (2020a). Benchmarking risk predictions and uncertainties in the NSCR model of GCR cancer risks with revised low LET risk coefficients. *Life sciences in space research*, *27*, 64-73.

Cucinotta, F. A., & Cacao, E. (2020b). Predictions of cognitive detriments from galactic cosmic ray exposures to astronauts on exploration missions. *Life Sciences in Space Research*, *25*, 129-135.

Cucinotta, F. A., & Saganti, P. B. (2022a). Race and ethnic group dependent space radiation cancer risk predictions. *Scientific Reports*, *12*(1), 1-10.

Cucinotta, F. A. (2022b). Flying without a Net: Space Radiation Cancer Risk Predictions without a Gamma-ray Basis. *International Journal of Molecular Sciences*, *23*(8), 4324.

Cucinotta, F. A. (2024). Non-targeted effects and space radiation risks for astronauts on multiple International Space Station and lunar missions. *Life Sciences in Space Research*, *40*, 166-175.

Cullings, H. M., Pierce, D. A., & Kellerer, A. M. (2014). Accounting for neutron exposure in the Japanese atomic bomb survivors. *Radiation research*, *182*(6), 587-598.

de Laplace, P. S. (1820). *Théorie analytique des probabilités* (Vol. 7). Courcier.

De la Torre, G. G. (2014). Cognitive neuroscience in space. *Life*, *4*(3), 281-294.

Delp, M. D., Charvat, J. M., Limoli, C. L., Globus, R. K., & Ghosh, P. (2016). Apollo lunar astronauts show higher cardiovascular disease mortality: possible deep space radiation effects on the vascular endothelium. *Scientific reports*, *6*(1), 1-11.

Dertinger, H., & Jung, H. (1970). Direct and indirect action of radiation. In *Molecular Radiation Biology* (pp. 70-90). Springer, New York, NY.

Desouky, O., Ding, N., & Zhou, G. (2015). Targeted and non-targeted effects of ionizing radiation. *Journal of Radiation Research and Applied Sciences*, *8*(2), 247-254.

Desouky, O., & Zhou, G. (2016). Biophysical and radiobiological aspects of heavy charged particles. *Journal of Taibah University for Science*, *10*(2), 187-194.

Dingfelder, M., Jorjishvili, I. G., Gersh, J. A., & Toburen, L. H. (2006). Heavy ion track structure simulations in liquid water at relativistic energies. *Radiation protection dosimetry*, *122*(1-4), 26-27.

Durante, M., & Cucinotta, F. A. (2008). Heavy ion carcinogenesis and human space exploration. *Nature Reviews Cancer*, *8*(6), 465-472.

Durante, M., & Cucinotta, F. A. (2011). Physical basis of radiation protection in space travel. *Reviews of modern physics*, *83*(4), 1245.

Ehresmann, B., Hassler, D. M., Zeitlin, C., Guo, J., Köhler, J., Wimmer-Schweingruber, R. F., ... & Reitz, G. (2016). Charged particle spectra measured during the transit to Mars with the Mars Science Laboratory Radiation Assessment Detector (MSL/RAD). *Life sciences in space research*, *10*, 29-37.

Eichenauer, J., & Lehn, J. (1986). A non-linear congruential pseudo random number generator. *Statistische Hefte*, *27*(1), 315-326.

ESA (2020, March 30). *Types of orbits*. The European Space Agency. https://www.esa.int/Enabling_Support/Space_Transportation/Types_of_orbits#LEO

Ferrari, A., Sala, P. R., Fasso, A., Ranft, J., & Siegen, U. (2005). *FLUKA: a multi-particle transport code* (No. SLAC-R-773). Stanford Linear Accelerator Center (SLAC).

Fry, R. J. M., Powers-Risius, P., Alpen, E. L., & Ainsworth, E. J. (1985). High-LET radiation carcinogenesis. *Radiation Research*, *104*(2s), S188-S195.

Furihata, S., Niita, K., Meigo, S. I., Ikeda, Y., & Maekawa, F. (2001). *The GEM code. A simulation program for the evaporation and the fission process of an excited nucleus* (No. JAERI-DATA/CODE--2001-015). Japan Atomic Energy Research Inst..

Gasinska, A., Dubray, B., Hill, S. A., Denekamp, J., Thames, H. D., & Fowler, J. F. (1993). Early and late injuries in mouse rectum after fractionated X-ray and neutron irradiation. *Radiotherapy and Oncology*, *26*(3), 244-253.

Geant4 Collaboration (2021). *Physics Reference Manual Release 11.0* (Rev6.0).

Gentle, J. E. (2003). *Random number generation and Monte Carlo methods* (2nd ed.). New York: springer.

Goodhead, D. (1988). Spatial and temporal distribution of energy. *Health Physics*, *55*(2), 231-240.

Goodhead, D. T. (1994). Initial events in the cellular effects of ionizing radiations: clustered damage in DNA. *International journal of radiation biology*, *65*(1), 7-17.

Goodhead, D. T., & Nikjoo, H. (1997). Radiation track structure. *Radioprotection*, *32*, C1-3.

Goodhead, D. T. (1999). Mechanisms for the biological effectiveness of high-LET radiations. *Journal of radiation research, 40*(SUPPL), S1-S13.

Goorley, T., James, M., Booth, T., Brown, F., Bull, J., Cox, L. J., ... & Zukaitis, T. (2012). Initial MCNP6 release overview. *Nuclear technology*, *180*(3), 298-315.

Gubernatic, J. E., & Los Alamos National Laboratory (2003). *The Monte Carlo method in the physical sciences : celebrating the 50th anniversary of the Metropolis Algorithm : Los Alamos, New Mexico, 9-11 June 2003*. American Institute of Physics.

Guo, J., Zeitlin, C., Wimmer-Schweingruber, R. F., Hassler, D. M., Posner, A., Heber, B., ... & Reitz, G. (2015). Variations of dose rate observed by MSL/RAD in transit to Mars. *Astronomy & Astrophysics*, *577*, A58.

Haettner, E., Iwase, H., & Schardt, D. (2006). Experimental fragmentation studies with 12C therapy beams. *Radiation protection dosimetry*, *122*(1-4), 485-487.

Haigh, T., Priestley, M., & Rope, C. (2014). Los alamos bets on eniac: Nuclear monte carlo simulations, 1947-1948. *IEEE Annals of the History of Computing*, *36*(3), 42-63.

Hall, E. J., & Giaccia, A. J. (2018). *Radiobiology for the Radiologist* (8th ed.). Wolters Kluwer.

Hargens, A. R., & Vico, L. (2016). Long-duration bed rest as an analog to microgravity. *Journal of applied physiology*, *120*(8), 891-903.

Harrison, R. L. (2010, January). Introduction to monte carlo simulation. In *AIP conference proceedings* (Vol. 1204, No. 1, pp. 17-21). American Institute of Physics.

Hassler, D. M., Zeitlin, C., Wimmer-Schweingruber, R. F., Ehresmann, B., Rafkin, S., Eigenbrode, J. L., ... & Berger, G. (2014). Mars' surface radiation environment measured with the Mars Science Laboratory's Curiosity rover. *science*, *343*(6169), 1244797.

Heilbronn, L., Nakamura, T., Iwata, Y., Kurosawa, T., Iwase, H., & Townsend, L. W. (2005). Overview of secondary neutron production relevant to shielding in space. *Radiation protection dosimetry*, *116*(1-4), 140-143.

Heilbronn, L., Townsend, L., Burnham, C., Green, H., Tsai, P. E., Borak, T., & McBeth, R. (2014, March). Neutron fluences and doses behind shielded environments in space. In *2014 IEEE Aerospace Conference* (pp. 1-8). IEEE.

Heilbronn, L. H., Borak, T. B., Townsend, L. W., Tsai, P. E., Burnham, C. A., & McBeth, R. A. (2015). Neutron yields and effective doses produced by Galactic Cosmic Ray interactions in shielded environments in space. *Life Sciences in Space Research*, *7*, 90-99.

Hienz, R., Davis, C., Weed, M., Guida, P., Gooden, V., Brady, J., & Roma, P. (2010). Neurobehavioral Effects of Space Radiation on Psychomotor Vigilance Tests. *38th COSPAR Scientific Assembly*, *38*, 8.

Hintze, P., Meier, A., & Shah, M. (2018, July). Sabatier system design study for a mars isru propellant production plant. 48th International Conference on Environmental Systems.

Hirayama, H., Namito, Y., Nelson, W. R., Bielajew, A. F., Wilderman, S. J., & Michigan, U. (2005). *The EGS5 code system* (No. SLAC-R-730). United States. Department of Energy.

Hirayama, R., Ito, A., Tomita, M., Tsukada, T., Yatagai, F., Noguchi, M., ... & Furusawa, Y. (2009). Contributions of direct and indirect actions in cell killing by high-LET radiations. *Radiation research*, *171*(2), 212-218.

Hoffman, S. J. (1997). *Human exploration of Mars: the reference mission of the NASA Mars exploration study team* (Vol. 6107). National Aeronautics and Space Administration, Lyndon B. Johnson Space Center.

ICRP (1975). International Commission on Radiological Protection. *ICRP Publication 23, Report of the Task Group on Reference Man*. Pergamon Press, Oxford, UK.

ICRP (1977). International Commission on Radiological Protection. *ICRP Publication 26, Recommendations of the International Commission on Radiological Protection*. Ann. ICRP 1 (3).

ICRP (1991). International Commission on Radiological Protection. *ICRP Publication 60, 1990 Recommendations of the International Commission on Radiological Protection*. Ann. ICRP 21 (1-3).

ICRP (2002). International Commission on Radiological Protection. *ICRP Publication 89, Basic Anatomical and Physiological Data for Use in Radiological Protection Reference Values*. Ann. ICRP 32 (3-4).

ICRP (2007). International Commission on Radiological Protection. *ICRP Publication 103, The 2007 Recommendations of the International Commission on Radiological Protection*. Ann. ICRP 37 (2-4).

ICRP (2009). International Commission on Radiological Protection. *ICRP Publication 110, Adult Reference Computational Phantoms*. Ann. ICRP 39 (2).

ICRU (1989). International Commission on Radiation Units and Measurements. *ICRU Report 44, Tissue substitutes in radiation dosimetry and measurement*. Bethesda, MD, USA.

ISO (2004). International Organization for Standardization. *ISO 15390, Space environment (natural and artificial) – Galactic cosmic ray model*.

Iwamoto, O., Nakagawa, T., Chiba, S., & Otuka, N. (2011a). Covariance evaluation for actinide nuclear data in JENDL-4. *Journal of the Korean Physical Society*, *59*(2), 1224-1229.

Iwamoto, Y., Niita, K., Sato, T., Matsuda, N., Iwase, H., Nakashima, H., & Sakamoto, Y. (2011b). Application and validation of event generator in the PHITS code for the low-energy neutron-induced reactions. *Prog. Nucl. Sci. Technol*, *2*, 931-935.

Iwamoto, Y., Sato, T., Hashimoto, S., Ogawa, T., Furuta, T., Abe, S. I., ... & Niita, K. (2017). Benchmark study of the recent version of the PHITS code. *Journal of Nuclear Science and Technology*, *54*(5), 617-635.

Iwamoto, Y., Hashimoto, S., Sato, T., Matsuda, N., Kunieda, S., Çelik, Y., ... & Niita, K. (2022). Benchmark study of particle and heavy-ion transport code system using shielding integral

benchmark archive and database for accelerator-shielding experiments. *Journal of Nuclear Science and Technology*, *59*(5), 665-675.

Iwase, H., Niita, K., & Nakamura, T. (2002). Development of general-purpose particle and heavy ion transport Monte Carlo code. *Journal of Nuclear Science and Technology*, *39*(11), 1142-1151.

Jäckel, P. (2002). *Monte Carlo methods in finance* (Vol. 71). J. Wiley.

Jackson, J. D., & McCarthy, R. L. (1972). z 3 corrections to energy loss and range. *Physical Review B*, *6*(11), 4131.

Jiggens, P., Chavy-Macdonald, M. A., Santin, G., Menicucci, A., Evans, H., & Hilgers, A. (2014). The magnitude and effects of extreme solar particle events. *Journal of Space Weather and Space Climate*, *4*, A20.

Jun, I. (2001). Effects of secondary particles on the total dose and the displacement damage in space proton environments. *IEEE Transactions on Nuclear science*, *48*(1), 162-175.

Kalos, M. H., & Whitlock, P. A. (2009). *Monte carlo methods*. John Wiley & Sons.

Kase, P. G. (1970). Computerized anatomical model man. *Air Force Weapons Laboratory Technical Report No. AFWL-TR-69-161, Kirtland Air Force Base, NM*.

Kelvin, L. (1901). I. Nineteenth century clouds over the dynamical theory of heat and light. *The London, Edinburgh, and Dublin Philosophical Magazine and Journal of Science*, *2*(7), 1-40.

Kieffer, H. H. (1976). Soil and surface temperatures at the Viking landing sites. *Science*, *194*(4271), 1344-1346.

Kim, M. H. Y., George, K. A., & Cucinotta, F. A. (2006). Evaluation of skin cancer risk for lunar and Mars missions. *Advances in Space Research*, *37*(9), 1798-1803.

Kim, M. H. Y., Cucinotta, F. A., & Wilson, J. W. (2007). A temporal forecast of radiation environments for future space exploration missions. *Radiation and Environmental Biophysics*, *46*(2), 95-100.

Kim, M. H. Y., Hayat, M. J., Feiveson, A. H., & Cucinotta, F. A. (2009a). Prediction of frequency and exposure level of solar particle events. *Health physics*, *97*(1), 68-81.

Kim, M. H. Y., Hayat, M. J., Feiveson, A. H., & Cucinotta, F. A. (2009b). Using high-energy proton fluence to improve risk prediction for consequences of solar particle events. *Advances in Space Research*, *44*(12), 1428-1432.

Kim, M. Y., Rusek, A., & Cucinotta, F. A. (2015). Issues in ground-based GCR simulation for space radiobiology. *Front Radiat Onc*, *5*, 122.

Knoll, G. F. (2010). *Radiation detection and measurement*. John Wiley & Sons.

Korcyl, M. (2012). *Track structure modelling for ion radiotherapy.* [Doctoral dissertation, Jagiellonian University].

Kramer, R., Zankl, M., Williams, G., & Drexler, G. (1982). The calculation of dose from external photon exposures using reference human phantoms and Monte Carlo methods. *Part I: the male (ADAM) and female (EVA) adult mathematical phantoms*.

Krämer, M., & Scholz, M. (2000). Treatment planning for heavy-ion radiotherapy: calculation and optimization of biologically effective dose. *Physics in Medicine & Biology*, *45*(11), 3319.

Kramer, R., Vieira, J. W., Khoury, H. J., Lima, F. R. A., & Fuelle, D. (2003). All about MAX: a male adult voxel phantom for Monte Carlo calculations in radiation protection dosimetry. *Physics in Medicine & Biology*, *48*(10), 1239.

Kramer, R., Khoury, H. J., Vieira, J. W., Loureiro, E. C. M., Lima, V. J. M., Lima, F. R. A., & Hoff, G. (2004). All about FAX: a female adult voxel phantom for Monte Carlo calculation in radiation protection dosimetry. *Physics in Medicine & Biology*, *49*(23), 5203.

Krane, K. S. (1987). *Introductory nuclear physics*. John Wiley & Sons.

Kutcher, G. J., & Green, A. E. S. (1976). A model for energy deposition in liquid water. *Radiation Research*, *67*(3), 408-425.

Lambright, W. H. (2014). *Why Mars: NASA and the politics of space exploration*. JHU Press.

Landau, D. F., & Longuski, J. M. (2006). Trajectories for human missions to Mars, Part I: impulsive transfers. *Journal of Spacecraft and Rockets*, *43*(5), 1035-1042.

Leclerc, G. L., & de Buffon, C. (1777). Essai d'arithmétique morale. *Supplément à l'Histoire Naturelle*, *4*.

Lee, S. J., Lehar, A., Meir, J. U., Koch, C., Morgan, A., Warren, L. E., ... & Germain-Lee, E. L. (2020). Targeting myostatin/activin A protects against skeletal muscle and bone loss during spaceflight. *Proceedings of the National Academy of Sciences*, *117*(38), 23942-23951.

Lehmer, D. H. (1951). Mathematical methods in large-scale computing units. *Annu. Comput. Lab. Harvard Univ.*, *26*, 141-146.

Letaw, J. R., Silberberg, R., & Tsao, C. (1983). Proton-nucleus total inelastic cross-sections-an empirical formula for E greater than 10 MeV. *The Astrophysical Journal Supplement Series*, *51*, 271-275.

Lewis, S. R., Collins, M., Read, P. L., Forget, F., Hourdin, F., Fournier, R., ... & Huot, J. P. (1999). A climate database for Mars. *Journal of Geophysical Research: Planets*, *104*(E10), 24177-24194.

Lindhard, J., & So, A. H. (1996). Relativistic theory of stopping for heavy ions. *Physical Review A*, *53*(4), 2443.

Manno, I. (1999). *Introduction to the Monte-Carlo method*. Akademiai Kiado.

Martin, A., Harbison, S., Beach, K., & Cole, P. (2018). *An introduction to radiation protection*. CRC Press.

Mattfeld, B., Stromgren, C., Shyface, H., Komar, D. R., Cirillo, W., & Goodliff, K. (2014). *Trades between opposition and conjunction class trajectories for early human missions to Mars* (No. NF1676L-18141).

Matthiä, D., Berger, T., Mrigakshi, A. I., & Reitz, G. (2013). A ready-to-use galactic cosmic ray model. *Advances in Space Research*, *51*(3), 329-338.

Matthiä, D., Ehresmann, B., Lohf, H., Köhler, J., Zeitlin, C., Appel, J., ... & Wimmer-Schweingruber, R. F. (2016). The Martian surface radiation environment–a comparison of models and MSL/RAD measurements. *Journal of Space Weather and Space Climate*, *6*, A13.

Maupin, K. A., Childress, P., Brinker, A., Khan, F., Abeysekera, I., Aguilar, I. N., ... & Kacena, M. A. (2019). Skeletal adaptations in young male mice after 4 weeks aboard the International Space Station. *npj Microgravity*, *5*(1), 21.

Mazhdrakov, M., Benov, D., & Valkanov, N. (2018). *The Monte Carlo method: engineering applications*. ACMO Academic Press.

Metropolis, N., & Ulam, S. (1949). The monte carlo method. *Journal of the American statistical association*, *44*(247), 335-341.

Metropolis, N. (1987). The beginning of the Monte Carlo method. *Los Alamos Science*, *15*(584), 125-130.

Mode, C. J. (2011). *Applications of Monte Carlo methods in biology, medicine and other fields of science*. IntechOpen.

Mokhov, N. V., & Van Ginneken, A. (1999, March). Muons versus hadrons for radiotherapy. In *Proceedings of the 1999 Particle Accelerator Conference (Cat. No. 99CH36366)* (Vol. 4, pp. 2525-2527). IEEE.

Morgan, R. L. (1972, July). Fast neutron therapy. In *AIP Conference Proceedings* (Vol. 9, No. 1, pp. 562-577). American Institute of Physics.

Mortezaee, K., Najafi, M., Farhood, B., Ahmadi, A., Shabeeb, D., & Eleojo Musa, A. (2019). Genomic instability and carcinogenesis of heavy charged particles radiation: clinical and environmental implications. *Medicina*, *55*(9), 591.

Musk, E. (2017). Making humans a multi-planetary species. *New Space*, *5*(2), 46-61.

Musk, E. (2018). Making life multi-planetary. *New Space*, *6*(1), 2-11.

Naito, M., & Kodaira, S. (2022). Considerations for practical dose equivalent assessment of space radiation and exposure risk reduction in deep space. *Scientific Reports*, *12*(1), 13617.

Nakahara, Y., & Tsutsui, T. (1982). *NMTC/JAERI: a simulation code system for high energy nuclear reactions and nucleon-meson transport processes* (No. JAERI-M--82-198). Japan Atomic Energy Research Inst..

Nara, Y., Otuka, N., Ohnishi, A., Niita, K., & Chiba, S. (1999). Relativistic nuclear collisions at 1 0 A GeV energies from p+ Be to Au+ Au with the hadronic cascade model. *Physical Review C*, *61*(2), 024901.

NASA (2020, September). The National Aeronautics and Space Administration. *NASA's Lunar Exploration Program Overview*.

NASA (2023, Dec 10). The National Aeronautics and Space Administration. *Mars Fact Sheet*. https://nssdc.gsfc.nasa.gov/planetary/factsheet/marsfact.html

NCRP (2000). National Council on Radiation Protection and Measurements. *NCRP Report 132, Recommendations of dose limits for low Earth orbit*.

NCRP (2006). National Council on Radiation Protection and Measurements. *NCRP Report 153, Information Needed to Make Radiation Protection Recommendations for Space Missions Beyond Low-Earth Orbit*.

NCRP (2014). National Council on Radiation Protection and Measurements. *NSCR Commentary 23, Radiation protection for space activities: Supplement to previous recommendations.*

NICT (2024, Feb 17). National Institute of Information and Communications Technology. *WArning System for AVIation Exposure to Solar energetic particle (WASAVIES)*. https://wasavies.nict.go.jp/FFPday.txt

Niita, K., Chiba, S., Maruyama, T., Maruyama, T., Takada, H., Fukahori, T., ... & Iwamoto, A. (1995). Analysis of the (N, xN′) reactions by quantum molecular dynamics plus statistical decay model. *Physical Review C*, *52*(5), 2620.

Niita, K., Takada, H., Meigo, S. I., & Ikeda, Y. (2001). High-energy particle transport code NMTC/JAM. *Nuclear Instruments and Methods in Physics Research Section B: Beam Interactions with Materials and Atoms*, *184*(3), 406-420.

Niita, K., Sato, T., Iwase, H., Nose, H., Nakashima, H., & Sihver, L. (2006). PHITS—a particle and heavy ion transport code system. *Radiation measurements*, *41*(9-10), 1080-1090.

NIST (2023, Oct 31). The National Institute of Standards and Technology. *Stopping-Power And Range Tables for Proton*. https://physics.nist.gov/PhysRefData/Star/Text/PSTAR.html

Noguchi, K., Ikeda, S., Kuroda, T., Tellmann, S., & Pätzold, M. (2014). Estimation of changes in the composition of the Martian atmosphere caused by CO_2 condensation from GRS Ar

measurements and its application to the rederivation of MGS radio occultation measurements. *Journal of Geophysical Research: Planets*, *119*(12), 2510-2521.

NRC (1997). National Research Council. *Radiation hazards to crews of interplanetary missions: biological issues and research strategies*. National Academies Press.

NRC (2006). National Research Council. *Health risks from exposure to low levels of ionizing radiation: BEIR VII phase 2*.

NRC (2012). National Research Council. *Technical evaluation of the NASA model for cancer risk to astronauts due to space radiation.*

Nymmik, R. A., Panasyuk, M. I., Pervaja, T. I., & Suslov, A. A. (1992). A model of galactic cosmic ray fluxes. *International Journal of Radiation Applications and Instrumentation. Part D. Nuclear Tracks and Radiation Measurements*, *20*(3), 427-429.

Nymmik, R. A., Panasyuk, M. I., & Suslov, A. A. (1996). Galactic cosmic ray flux simulation and prediction. *Advances in Space Research*, *17*(2), 19-30.

Ogawa, T., Sato, T., Hashimoto, S., & Niita, K. (2015a). Revision of JAERI-QMD for analysis of peripheral nucleus-nucleus collisions.

Ogawa, T., Sato, T., Hashimoto, S., Satoh, D., Tsuda, S., & Niita, K. (2015b). Energy-dependent fragmentation cross-sections of relativistic C 12. *Physical Review C*, *92*(2), 024614.

Ogawa, T., Hashimoto, S., Sato, T., & Niita, K. (2016). Application of JAERI quantum molecular dynamics model for collisions of heavy nuclei. In *EPJ Web of Conferences* (Vol. 122, p. 04005). EDP Sciences.

Ornitz, R. D., Bradley, E. W., Mossman, K. L., Fender, F. M., Schell, M. C., & Rogers, C. C. (1980). Clinical observations of early and late normal tissue injury inpatients receiving fast neutron irradiation. *International Journal of Radiation Oncology* Biology* Physics*, *6*(3), 273-279.

O'Shea, C. (2023, May 19*). NASA selects Blue Origin as second Artemis Lunar Lander Provider*. NASA. https://www.nasa.gov/press-release/nasa-selects-blue-origin-as-second-artemis-lunar-lander-provider

Papadimitroulas, P., Loudos, G., Nikiforidis, G. C., & Kagadis, G. C. (2012). A dose point kernel database using GATE Monte Carlo simulation toolkit for nuclear medicine applications: comparison with other Monte Carlo codes. *Medical physics*, *39*(8), 5238-5247.

Patrignani, C., Agashe, K., Aielli, G., Amsler, C., Antonelli, M., Asner, D. M., ... & Ringwald, A. (2016). Review of particle physics.

Pak, S., & Cucinotta, F. A. (2021). Comparison between PHITS and GEANT4 Simulations of the Heavy Ion Beams at the BEVALAC at LBNL and the Booster Accelerator at BNL. *Life Sciences in Space Research*, *29*, 38-45.

Pak, S., & Cucinotta, F. A. (2024). Tissue-Specific Dose Equivalents of Secondary Mesons and Leptons during Galactic Cosmic Ray Exposures for Mars Exploration. *Life Sciences in Space Research*, *41*, 29-42.

Phillips, K. J. (1995). *Guide to the Sun*. Cambridge University Press.

PHITS development team (2022, March). Features of PHITS3.27.

Pierce, T. E., & Blann, M. (1968). Stopping Powers and Ranges of 5-90-MeV S 32, Cl 35, Br 79, and I 127 Ions in H 2, He, N 2, Ar, and Kr: A Semiempirical Stopping Power Theory for Heavy Ions in Gases and Solids. *Physical Review*, *173*(2), 390.

Plante, I., & Cucinotta, F. A. (2011). Monte-Carlo simulation of ionizing radiation tracks. *Application of Monte Carlo methods in biology, medicine and other fields of science. InTech, Rijeka, Croatia*, 315-356.

Rauch, B. F., & CALET Collaboration. (2014). Predicted CALET measurements of ultra-heavy cosmic ray relative abundances. *Advances in Space Research*, *53*(10), 1444-1450.

Roberts, D. R., Zhu, X., Tabesh, A., Duffy, E. W., Ramsey, D. A., & Brown, T. R. (2015). Structural brain changes following long-term 6 head-down tilt bed rest as an analog for spaceflight. *American Journal of Neuroradiology*, *36*(11), 2048-2054.

Roberts, D. R., Albrecht, M. H., Collins, H. R., Asemani, D., Chatterjee, A. R., Spampinato, M. V., Zhu, X., Chimowitz, M. I., & Antonucci, M. U. (2017). Effects of spaceflight on astronaut brain structure as indicated on MRI. *New England Journal of Medicine*, *377*(18), 1746-1753.

Rojdev, K., Koontz, S., Reddell, B., Atwell, W., & Boeder, P. (2015). Comparison and Validation of FLUKA and HZETRN as Tools for Investigating the Secondary Neutron Production in Large Space Vehicles. In *AIAA SPACE 2015 Conference and Exposition* (p. 4601).

Rosenfeld, A. H. (1975). The particle data group: Growth and operations-eighteen years of particle physics. *Annual Review of Nuclear Science*, *25*(1), 555-598.

Rubinstein, R. Y., & Kroese, D. P. (2016). *Simulation and the Monte Carlo method* (Vol. 10). John Wiley & Sons.

Rudd, M. E. (1990). Cross-sections for production of secondary electrons by charged particles. *Radiation Protection Dosimetry*, *31*(1-4), 17-22.

Sato, T., Tsuda, S., Sakamoto, Y., Yamaguchi, Y., & Niita, K. (2003). Analysis of dose-LET distribution in the human body irradiated by high energy hadrons. *Radiation protection dosimetry*, *106*(2), 145-153.

Sato, T., Iwamoto, Y., Hashimoto, S., Ogawa, T., Furuta, T., Abe, S. I., ... & Niita, K. (2018). Features of particle and heavy ion transport code system (PHITS) version 3.02. *Journal of Nuclear Science and Technology*, *55*(6), 684-690.

Sato, T., Endo, A., Sihver, L., & Niita, K. (2011). Dose estimation for astronauts using dose conversion coefficients calculated with the PHITS code and the ICRP/ICRU adult reference computational phantoms. *Radiation and environmental biophysics*, *50*, 115-123.

Sato, T., Iwamoto, Y., Hashimoto, S., Ogawa, T., Furuta, T., Abe, S. I., ... & Niita, K. (2024). Recent improvements of the particle and heavy ion transport code system–PHITS version 3.33. *Journal of Nuclear Science and Technology*, *61*(1), 127-135.

Sawilowsky, S. S. (2003). You think you've got trivials?. *Journal of Modern Applied Statistical Methods*, *2*(1), 21.

Shea, M. A., & Smart, D. F. (1990). A summary of major solar proton events. *Solar Physics*, *127*(2), 297-320.

Shibata, K., Iwamoto, O., Nakagawa, T., Iwamoto, N., Ichihara, A., Kunieda, S., ... & Katakura, J. I. (2011). JENDL-4.0: a new library for nuclear science and engineering. *Journal of Nuclear Science and Technology*, *48*(1), 1-30.

Simpson, J. A. (1983). Elemental and isotopic composition of the galactic cosmic rays. *Annual Review of Nuclear and Particle Science*, *33*(1), 323-382.

Slaba, T. C., Qualls, G. D., Clowdsley, M. S., Blattnig, S. R., Walker, S. A., & Simonsen, L. C. (2010). Utilization of CAM, CAF, MAX, and FAX for space radiation analyses using HZETRN. *Advances in Space Research*, *45*(7), 866-883.

Slaba, T. C., McMullen, A. M., Thibeault, S. A., Sandridge, C. A., Clowdsley, M. S., & Blattnig, S. R. (2011, August). Oltaris: An efficient web-based tool for analyzing materials exposed to space radiation. In *Nanophotonics and Macrophotonics for Space Environments V* (Vol. 8164, pp. 138-145). SPIE.

Slaba, T. C., Blattnig, S. R., Reddell, B., Bahadori, A., Norman, R. B., & Badavi, F. F. (2013). Pion and electromagnetic contribution to dose: Comparisons of HZETRN to Monte Carlo results and ISS data. *Advances in Space Research*, *52*(1), 62-78.

Smith, A. R. (2006). Proton therapy. *Physics in Medicine & Biology*, *51*(13), R491.

Snyder, W. S., et al. (1969). Estimates of absorbed fractions for monoenergetic photon sources uniformly distributed in various argans of a heterogeneous phantom. *MIRD pamphlet No. 5*.

Snyder, W. S., et al. (1978). Estimates of specific absorbed fractions for monoenergetic photon sources uniformly distributed in various organs of a heterogeneous phantom. *MIRD pamphlet*, *5*.

Stavnichuk, M., Mikolajewicz, N., Corlett, T., Morris, M., & Komarova, S. V. (2020). A systematic review and meta-analysis of bone loss in space travelers. *npj Microgravity*, *6*(1), 13.

Sternheimer, R. M., & Peierls, R. F. (1971). General expression for the density effect for the ionization loss of charged particles. *Physical Review B*, *3*(11), 3681.

Stone, E. C., Frandsen, A. M., Mewaldt, R. A., Christian, E. R., Margolies, D., Ormes, J. F., & Snow, F. (1998). The advanced composition explorer. *Space Science Reviews*, *86*, 1-22.

Stricklin, D. L., VanHorne-Sealy, J., Rios, C. I., Scott Carnell, L. A., & Taliaferro, L. P. (2021). Neutron radiobiology and dosimetry.

Takada, H., Yoshizawa, N., Kosako, K., & Ishibashi, K. (1998). An upgraded version of the nucleon meson transport code: NMTC/JAERI97.

Todd, P. (1992). Multiple cell hits by particle tracks in solid tissues. *Advances in Space Research*, *12*(2-3), 393-401.

Townsend, L. W. (1983). Abrasion cross-sections for 20Ne projectiles at 2.1 GeV/nucleon. *Canadian Journal of Physics*, *61*(1), 93-98.

Townsend, L. W., & Wilson, J. W. (1986). Energy-dependent parameterization of heavy-ion absorption cross-sections. *Radiation research*, 283-287.

Townsend, L. W., Wilson, J. W., Tripathi, R. K., Norbury, J. W., Badavi, F. F., & Khan, F. (1993). *HZEFRG1: An energy-dependent semiempirical nuclear fragmentation model* (No. L-17161).

Townsend, L. W., Cucinotta, F. A., Wilson, J. W., & Bagga, R. (1994). Estimates of HZE particle contributions to SPE radiation exposures on interplanetary missions. *Advances in Space Research*, *14*(10), 671-674.

Tylka, A. J., & Dietrich, W. F. (2009, July). A new and comprehensive analysis of proton spectra in ground-level enhanced (GLE) solar particle events. In *31th International Cosmic Ray Conference*. Lodź: Universal Academy Press.

Tylka, A. J., Dietrich, W., & Atwell, W. (2010). Band function representations of solar proton spectra in ground-level events. *38th COSPAR Scientific Assembly*, *38*, 4.

Ulam, S., Richtmyer, R. D., & von Neumann, J. (1947). Statistical methods in neutron diffusion. *LAMS-551, Los Alamos National Laboratory*, 1-22.

Usoskin, I. G., Kovaltsov, G. A., Mironova, I. A., Tylka, A. J., & Dietrich, W. F. (2011). Ionization effect of solar particle GLE events in low and middle atmosphere. *Atmospheric Chemistry and Physics*, *11*(5), 1979-1988.

VerWest, B. J., & Arndt, R. A. (1982). NN single pion production cross-sections below 1500 MeV. *Physical Review C*, *25*(4), 1979.

Von Braun, W. (1953). *The Mars Project*. University of Illinois Press.

Werner, C. J. (2017). MCNP Users Manual-Code Version 6.2. *Los Alamos National Laboratory*.

Werner, C. J., Bull, J. S., Solomon, C. J., Brown, F. B., McKinney, G. W., Rising, M. E., ... & Casswell, L. (2018). *MCNP version 6.2 release notes* (No. LA-UR-18-20808). Los Alamos National Lab.(LANL), Los Alamos, NM (United States).

Wilson, J. W. (1974). Multiple scattering of heavy ions, Glauber theory, and optical model. *Physics Letters B*, *52*(2), 149-152.

Wilson, J. W., & Townsend, L. W. (1981). An optical model for composite nuclear scattering. *Canadian Journal of Physics*, *59*(11), 1569-1576.

Wilson, J. W., Townsend, L. W., Chun, S. Y., Buck, W. W., Khan, F., & Cucinotta, F. (1988). *BRYNTRN: A baryon transport computer code, computation procedures and data base* (No. L-16432).

Wilson, J. W., Chun, S. Y., Badavi, F. F., Townsend, L. W., Lamkin, & S. L. (1991). *HZETRN: A heavy ion/nucleon transport code for space radiations* (No. NASA-TP-3146).

Wilson, J. W., Thibeault, S. A., Cucinotta, F. A., Shinn, J. L., Kim, M., Kiefer, R., & Badavi, F. F. (1995a). Issues in protection from galactic cosmic rays. *Radiation and environmental biophysics*, *34*(4), 217-222.

Wilson, J. W., Tripathi, R. K., Cucinotta, F. A., Shinn, J. L., Badavi, F. F., Chun, S. Y., ... & Miller, J. (1995b). *NUCFRG2: An evaluation of the semiempirical nuclear fragmentation database* (No. NASA-TP-3533).

Wilson, J. W., Badavi, F. F., Cucinotta, F. A., Shinn, J. L., Badhwar, G. D., Silberberg, R., ... & Tripathi, R. K. (1995c). *HZETRN: Description of a free-space ion and nucleon transport and shielding computer program* (No. NASA-TP-3495).

Wilson, J. W. (1997). *Shielding Strategies for Human Space Exploration: Proceedings of a Workshop Sponsored by the National Aeronautics and Space Administration and Held at Lyndon*

B. Johnson Space Center, Houston, Texas, December 6-8, 1995 (Vol. 3360). National Aeronautics and Space Administration, Langley Research Center.

Withers, H. R., Thames Jr, H. D., & Peters, L. J. (1982). Biological bases for high RBE values for late effects of neutron irradiation. *International Journal of Radiation Oncology* Biology* Physics*, *8*(12), 2071-2076.

Wu, H., Huff, J. L., Casey, R., Kim, M. H., & Cucinotta, F. A. (2009). Risk of acute radiation syndromes due to solar particle events. *The Human Health and Performance Risks for Space Explorations. Houston, Texas: NASA Human Research Program*, 171-90.

Yucker, W. R., & Huston, S. L. (1990). The computerized anatomical female. Final Report, MDC-6107. McDonnell Douglas Company, Huntington Beach, CA (United States).

Yucker, W. R., & Reck, R. J. (1992). Computerized anatomical female body self-shielding distributions. Report, MDC 92H0749, McDonnell Douglas Company, Huntington Beach, CA (United States).

Zeitlin, C., Miller, J., Heilbronn, L., Frankel, K., Gong, W., & Schimmerling, W. (1996). The fragmentation of 510 MeV/nucleon iron-56 in polyethylene. I. Fragment fluence spectra. *Radiation research*, *145*(6), 655-665.

Zeitlin, C., Hassler, D. M., Cucinotta, F. A., Ehresmann, B., Wimmer-Schweingruber, R. F., Brinza, D. E., ... & Reitz, G. (2013). Measurements of energetic particle radiation in transit to Mars on the Mars Science Laboratory. *science*, *340*(6136), 1080-1084.

<div align="center">**Curriculum Vitae**

Sungmin Pak
(sungminpak4@gmail.com)</div>

Education

Doctor of Philosophy – Interdisciplinary Health Sciences
University of Nevada, Las Vegas
May 2024

Master of Science – Space Research
Kyung Hee University
February 2018

Bachelor of Science – Astronomy and Space Science
Kyung Hee University
August 2016

Research

Space Radiation

Radiation Transport

Radiation Shielding

Monte Carlo Simulation

Space Instrument

Health Physics

Radiation Biology

Professional Membership

American Geophysical Union, Student Member, 2022 – Present

Radiation Research Society, Scholar-in-Training Member, 2021 – Present

Korean Space Science Society, Member, 2017 – Present

Teaching

Radiation Biology, Graduate Teaching Assistant, Department of Health Physics and Diagnostic Sciences, University of Nevada, Las Vegas, 2020, 2021, 2023, 2024.

Sectional Anatomy in Medical Imaging, Graduate Teaching Assistant, Department of Health Physics and Diagnostic Sciences, University of Nevada, Las Vegas, 2021 – 2023.

Selected Honors and Awards

Presidential Scholarship, Kyung Hee University, 2016, 2017.

Graduated with High Honors, Kyung Hee University, 2016.

Excellence Award, Kyung Hee University, 2015, 2016.

Publications

Pak S, Cucinotta FA. Tissue-Specific Dose Equivalents of Secondary Mesons and Leptons during Galactic Cosmic Ray Exposures for Mars Exploration. Life Sciences in Space Research. 2024; 41:29-42. https://doi.org/10.1016/j.lssr.2024.01.003

Cucinotta FA, **Pak S**. Cancer and Circulatory Disease Risks for the Largest Solar Particle Events in the Space Age. Life Sciences in Space Research. 2024; 40:1-7. https://doi.org/10.1016/j.lssr.2023.10.003

Cucinotta FA, **Pak S**. Isotopic production cross sections in proton-^{16}O and proton-^{12}C interactions for energies from 10 MeV/u to 100 GeV/u. Nuclear Instruments and Methods in Physics Research Section B: Beam Interactions with Materials and Atoms. 2023; 534:26-34. https://doi.org/10.1016/j.nimb.2022.11.005

Pak S, Cucinotta FA. Comparison between PHITS and GEANT4 Simulations of the Heavy Ion Beams at the BEVALAC at LBNL and the Booster Accelerator at BNL. Life Sciences in Space Research. 2021; 29:38-45. https://doi.org/10.1016/j.lssr.2021.03.002

Seon J, Chae KS, Na GW, Seo HK, Shin YC, Woo J, Lee CH, Seol WH, Lee CA, **Pak S**, Lee H, Shin SH, Larson DE, Hatch K, Parks GK, Sample J, McCarthy M, Tindall C, Jeon YJ, Choi JK, Park JY. Particle detector (PD) experiment of the Korea Space Environment Monitor (KSEM) aboard geostationary satellite GK2A. Space Science Reviews. 2020; 216(1):1-26. https://doi.org/10.1007/s11214-020-0636-4

Pak S, Shin Y, Woo J, Seon J. A numerical method to analyze geometric factors of a space particle detector relative to omnidirectional proton and electron fluxes. Journal of the Korean Astronomical Society. 2018; 51(4):111-7. https://doi.org/10.5303/JKAS.2018.51.4.111

Conference Presentations

Pak S, Cucinotta FA. Secondary Neutron Generation during Galactic Cosmic Ray and Solar Particle Event Exposures for Mars Exploration. American Geophysical Union Fall Meeting; 2022 December; Chicago, IL.

Lee C, **Pak S**, Seol W, Seon J. Energy Calibration of Charged Particle Detector Using Radioactive Isotope Sources. Asia Oceania Geosciences Society Annual Meeting; 2019 July-August; Singapore.

Na GW, Seon J, Chae KS, Shin Y, Woo J, Seol W, Lee C, **Pak S**, Shin S, Auster HU, Strauch C, Magnes W, Fischer D. In-Orbit Test Result for Korean Space Environment Monitor (KSEM) on GEO-KOMPSAT-2A. Asia Oceania Geosciences Society Annual Meeting; 2019 July-August; Singapore.

Shin SH, Seon J, **Pak S**, Shin Y. Analysis of Radiation Penetration and Shielding of Charged Particle Detector. Asia Oceania Geosciences Society Annual Meeting; 2019 July-August; Singapore.

Na GW, Seon J, Chae KS, Shin Y, Woo J, Seol W, Lee C, **Pak S**, Shin S. Early operation of Korean Space Environment Monitor (KSEM) onboard GEO-KOMPSAT-2A and the preliminary result of KSEM Particle Detector (PD). The Korean Space Science Society Spring Conference; 2019 April; Gangneung, South Korea.

Shin S, **Pak S**, Shin Y, Seon J. Understanding of the radiation shielding using Geant4-based simulation. The Korean Space Science Society Spring Conference; 2019 April; Gangneung, South Korea.

Pak S, Shin Y, Woo J, Yun J, Chae KS, Seon J, Lee K, Koo B. Deduction of Response of KSEM PD Using GEANT4 Particle Simulation. The Korean Space Science Society Spring Conference; 2017 April; Buan, South Korea.

Park JP, Jung I, **Pak S**, Lee S. Design and Analysis for CubeSat Sun Sensor. The Korean Society for Aeronautical and Space Sciences Spring Conference; 2017 April; Samcheok, South Korea.